May 2014

Determining Limitations of Kinetic Models for Pyrolysis Simulation of Fiber Reinforced Polymer Composites

Brianna Helen Gillespie
Worcester Polytechnic Institute

Caitlin Elizabeth Walde
Worcester Polytechnic Institute

Mary Alexis Long
Worcester Polytechnic Institute

Natalie Elizabeth McMillan
Worcester Polytechnic Institute

Determining Limitations of Kinetic Models for Pyrolysis Simulation of Fiber Reinforced Polymer Composites

A Major Qualifying Project Report submitted to the Faculty of
Worcester Polytechnic Institute
in partial fulfillment of the requirements for the
Degree of Bachelor of Science
By:

_____

Brianna Gillespie

_____

Mary Long

_____

Natalie McMillan

_____

Caitlin Walde

May 2014

Project Number: FM13

_____

Professor Nicholas A. Dembsey, Advisor

_____

Professor David DiBiasio, Advisor

Abstract

Recently the fire protection engineering community has started to use comprehensive pyrolysis models, to analyze the thermal performance of fire resistant polymers. In order to use these pyrolysis models material kinetics must be understood. This study evaluated recently proposed simplified kinetic modeling and analysis techniques. The material system considered was representative of fiber reinforced polymers, where ratios of resin to additive mixtures were varied to design for required fire performance. Samples of differing resin to additive ratios were evaluated by Thermogravimetric Analysis (TGA) and Differential Scanning Calorimetry (DSC). The approach was to examine the contributions of the resins and additives separately in order to evaluate if the thermal properties of the respective mixtures could be predicted. The TGA data was used to determine the activation energies through the application of an isoconversional method; these energies were then used to characterize the reactions taking place during decomposition. The various analyses suggest that transport effects take place as a result of the different sample morphologies. The DSC data was used to determine the heat of decomposition of each of the mixtures. The analysis determined that the heat of decompositions could be combined to calculate the corresponding heat of decomposition for each mixture. Through the examination of different resins and additives, it was determined that the models can be applied, however there are limitations based on the type of material as well as the different sample morphologies that affect the accuracy of the model.

Acknowledgements

We would like to thank Kresysler and Associates for providing the resins, additives, and mixture samples. We would also like to thank our advisors, Professor Nicholas Dembsey and Professor David Dibiasio, as well as Esther Kim and Randall Harris, for their assistance.

Table of Contents

Table of Figures

Table of Tables

Chapter 1: Introduction and Background

In the engineering world today, mechanical deformation of structures can be simulated by applying a Finite Element Analysis (FEA) to a Computer Aided Design (CAD) model. This computerized analysis is able to simulate the actual behavior of a structure by using input values for basic material mechanical properties. By simulating a test, companies are then able to make adjustments to the structure at a very low cost compared to the cost of having to repeat full-scale tests after each alteration.

In Fire Protection Engineering, these computer simulated tests exist in programs such as GPYRO and Fire Dynamics Simulator (FDS), but there are limitations, especially relative to input material properties (Appendix A: Computational Programs). A great amount of interest lies in new materials such as Fiber Reinforced Polymers (FRPs), as they are becoming more common in buildings for aesthetic applications; these FRPs add a new dimension of complexity to computer simulations (Appendix B: Fiber Reinforced Polymers). FRP composites are comprised of a polymer matrix, which consists of a resin and additives; and fiber filler, which are often glass or carbon fiber. While there are many different resins and additives available with innumerable combinations, there is little data and research in the literature on the basic kinetic and thermal properties of individual resins and additives as well as their mixtures. Without these properties, the thermal degradation of the materials cannot be accurately simulated in pyrolysis models.[1] Some work has been done in this area, but limited results are currently available.

Building codes such as the International Building Code (IBC) require National Fire Protection Association (NFPA) and American Society for Testing and Materials (ASTM) testing to ensure products demonstrate a certain level of performance. These tests evaluate either a material or an assembly, and can only be run once (Appendix C: NFPA and ASTM Standards). So, it is in the company's best interest to pass the test on the first attempt in order to save money. This can often lead to over-engineering of products; resources can further be saved if the company can design their products to specifically meet standards, rather than exceed them. If a company is able to accurately predict the behavior of a mixture based on the properties of the resin and additive individually, they may be able to optimize the ratio of the two to best meet the test standards.

Objectives

Three main objectives were distilled from understanding the background of this study. The objectives stated below were selected in an attempt to learn about this topic and to obtain an understanding of the samples. This research aimed to:

1. Determine if kinetic properties of individual components can be used to predict those of mixtures. Specific attention was paid to activation energy (E_a) and heat of decomposition (H_x);
2. Follow a proposed modeling method[2] to investigate and validate the notion of using a simplified reaction mechanism scheme;
3. Examine the presence of transport effects and how they affect testing, data, and modeling.

Chapter 2: Methods

Testing

The use of the following apparatuses assumes zero-dimensional analysis.

Thermogravimetric Analysis

Thermogravimetric Analysis (TGA) measures weight changes in a material as a function of temperature in a controlled atmosphere.[3] TGA was used with an inert purge gas flow of nitrogen and tested samples between 1 – 10 milligrams. Small sample size and constant purge gas flow rate were used in order to reduce or eliminate the effect of heat transfer effects and to remain consistent between runs.[4] Calibrations were completed at set intervals and a standard, well-known sample was tested as a case study to confirm the validity of results. ASTM D3850-12 was consulted and a uniform testing procedure was conducted throughout research. For a complete testing procedure, see Appendix D: Thermogravimetric Analysis.

Differential Scanning Calorimetry

Differential Scanning Calorimetry (DSC) measures and records the heat flow required to increase the temperature of a sample as a function of time.[5] DSC was used with an inert purge gas flow of nitrogen and tested samples between 1 – 5 milligrams. Small sample size and constant purge gas flow rate were used in order to reduce or eliminate the effect of heat transfer effects and to remain consistent between runs. Calibrations involving baseline and cell constant tests were run and recorded at the beginning of each day of testing. Standard, well-known samples were tested as references and as a case study to confirm the validity of results. ASTM D7426-08 and ASTM D3418-12e1 were consulted and a uniform testing procedure was observed throughout research. For a complete testing procedure, see Appendix E: Differential Scanning Calorimetry.

Samples

Kreysler provided samples that came in two main forms, solidified drops that were approximately 10mg each and placards of the material about 4 inches by 4 inches in size. During manufacturing, a liquid resin is mixed with powder additives; after it catalyzes, it solidifies into selected sample shape. Varying the surface area of a sample is known to cause variations in the results from a TGA and DSC; for this reason, three different sample morphologies were analyzed.[6] Specifically, powder filed from the placards, chunks chipped from the placards, and the solid drops were tested relative to each other. Drop and chunk morphologies most accurately simulate material that would be used in building applications. The drop samples were chosen over the chunk samples for the majority of analysis because the chunk morphology was highly variable in surface area and mass, whereas the drop samples were more consistent.

Each of the samples provided were made with varying resins and additives. Three different types of resins were examined; Hetron 650 T20, Ashland Fireblock Gelcoat FRP, and Gurit Ampreg 21 Fr. Additionally, two different additives were studied: Alumina trihydrate (ATH) and Sand. Table 1 shows pure samples and mixtures initially considered for testing. The numbers in the table correspond to a ratio between the two materials listed.

Table 1: Resin and Additive Mixtures

Hetron	Fireblock	Ampreg
Hetron & ATH (100:33)	Fireblock & Sand (70:30)	Ampreg & ATH (100:10)
Hetron & ATH (100:66)	Fireblock & Sand (60:40)	Ampreg & ATH (100:20)
Hetron & ATH (100:100)	Fireblock & Sand (50:50)	Ampreg & ATH (100:30)
Hetron & ATH (100:130)	Fireblock & Sand (40:60)	ATH
ATH	Sand	

All pure samples, including ATH and sand, were tested. Due to commercial availability, ATH was only able to be studied in the powder form.

Chapter 3: Analysis

Isoconversional Method

The use of an isoconversional method allowed for data from multiple heating rates to be accounted for in parameter estimation of activation energy. By including multiple heating rates, a more accurate result was obtained. The method of Ozawa, Flynn, and Wall (OFW)[7] was used for analysis of multiple heating rate tests of the resin and additive samples. Referencing the approach taken by Esther Kim[2] and retaining the notion of simplicity, the OFW method was selected because while it proves to be mathematically and conceptually simple, it is a validated approach in the literature.[8,9] In a study comparing five different types of isoconversional methods including the OFW method, it was concluded that for any isoconversional study, the biggest source of error lies in the approximation of a constant activation energy, but that all isoconversional methods gave accurate activation energy (E_a) values.[10] After data is put through a series of numerical operations, an activation energy trend can be observed. For a pure sample, a straight trend is seen and an average activation energy can be determined and then used as a value to begin model parameter optimization. Mixture activation energy trends help to elucidate the presence of multiple reactions, seen by the shifting and curving values of activation energies with declining mass fraction.[2] For the complete isoconversional method, see Appendix F.1: Isoconversional.

Modeling

In order to model the mass loss histories for the samples, a Runge Kutta Fourth Order (RK4) Method was applied to two ordinary differential equations for each reaction (Appendix F.2: Runge Kutta Modeling). The first equation represented the mass loss rate of a sample over time (Equation 1), the second equation represented the heating rate applied to the sample in the TGA (Equation 2). Since heating rate (β) is constant during testing, a change in temperature corresponds to a change in time. Subsequently, equations 1 and 2 were able to be combined into one ordinary differential equation.

$$\frac{d(1-\propto)(t)}{dt} = \left[Aexp\left(-\frac{E_a}{RT(t)}\right)\right](1-\propto(t))^n \qquad \text{(Eq. 1)}$$

$$\frac{dT(t)}{dt} = \beta \qquad \text{(Eq. 2)}$$

where: $\alpha = 1 - (m/m_o)$

$t\ is\ time\ (minutes)$

$m\ is\ mass\ of\ sample\ (kg)$

$m_o\ is\ initial\ mass\ of\ sample\ (kg)$

$A\ is\ pre-exponential\ constant$

$E_a\ is\ activation\ energy\ (kJ/mol)$

$R\ is\ the\ ideal\ gass\ constant\ (8.314\ J/molK)$

$T\ is\ temperature\ (K)$

$n\ is\ the\ exponent$

$\beta\ is\ heating\ rate\ (K/min)$

When modeling the decomposition of a sample, the activation energy, pre-exponential constant (A), and exponent (n) were optimized. As stated previously, the OFW isoconversional method determined activation energies for a range of mass fractions. For pure Hetron and pure ATH, the average value of their respective activation energies was used in the decomposition ordinary differential equation. This single value was then treated as a constant in the decomposition equation in order to prevent a compensation effect that is noted in the literature to be seen with activation energy and pre-exponential constant values.[6] Based on proposed kinetic modeling methods, it is reasonable to use an average value since Hetron and ATH activation energies followed a linear behavior for their respective mass fraction ranges. This suggests that the sample can be modeled as a single reaction.

The mass loss rate of the experimental data and the mathematical model were graphed with respect to temperature (Figure 1).

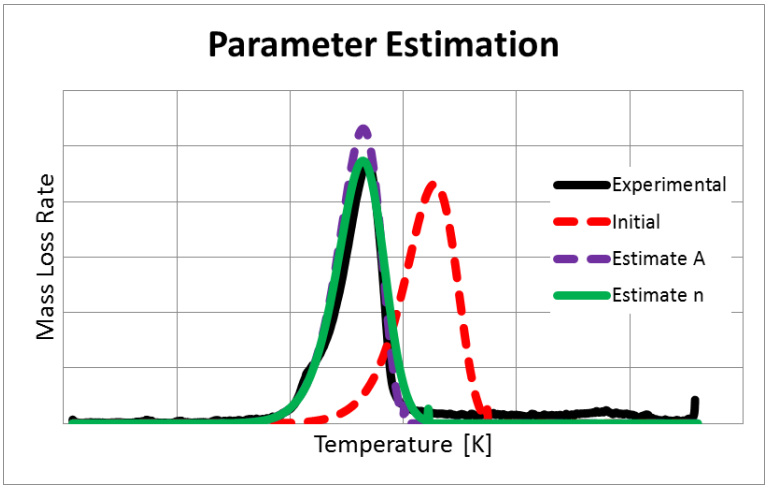

Figure 1: Optimizing Parameters

For the model, initial A and n values are 10^{10} and 1 respectively as is suggested in the proposed method. In order to fit the model, A was first adjusted to match the temperature range to that of the experimental data, and n was then adjusted to match the peak height.

Heat of Decomposition

Peaks in the heat flow curve generated by the DSC show the energy associated with transformations in a material; these can be melting, crystallization, decomposition, etc. In order to determine the heat of decomposition, the heat flow curve was plotted against the mass loss rate from the TGA. The temperature range of decomposition was selected by identifying the peak observed on the mass loss rate curve. The red dots seen on the curve in Figure 2 correspond to the temperature range of decomposition.

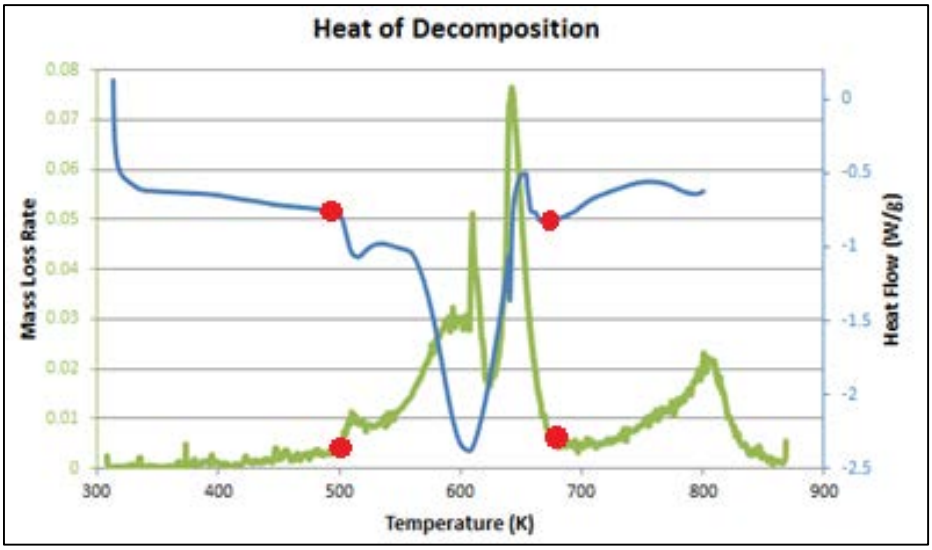

Figure 2: Correlate Decomposition Temperature Range from Mass Loss Rate the Heat Flow

As can be seen in Figure 2, the temperature range bounds are then translated to the heat flow curve to mark the boundaries of integration.

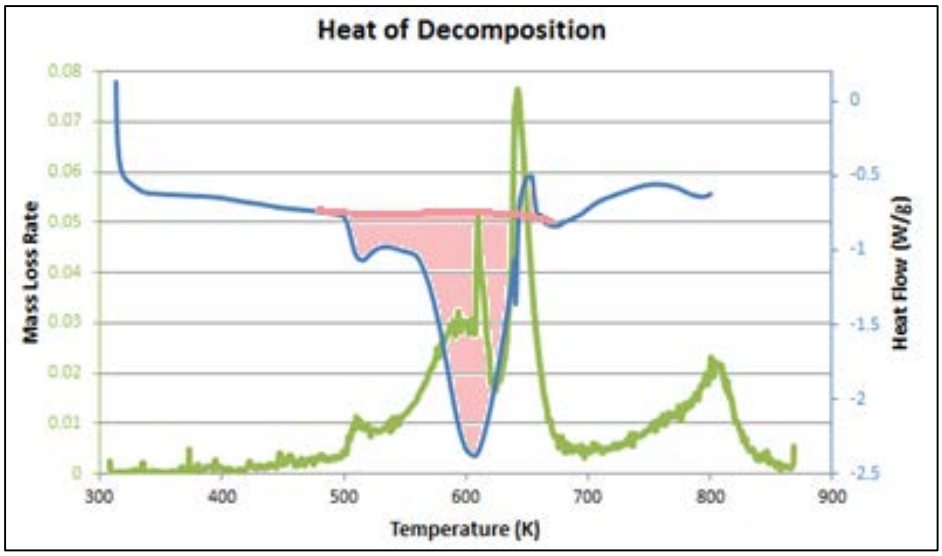

Figure 3: Integrate Heat Flow between Decomposition Temperature Range

The shaded area seen in Figure 3 represents the integration performed to yield the experimental heat of decomposition value.[11] The heat of decomposition is a valuable material property that enhances the understanding of a material.

Chapter 4: Results and Discussion

Observations

Several observations were made about trends seen in the experimental FRP data. Throughout testing, it became evident that a sample's morphology can greatly affect the decomposition behavior of a material. The comparison of mass fraction and mass loss rate curves for powder, chunk, and drop samples illustrated that a transport effect takes place. A material transport effect occurs when it takes longer for heat to permeate through different types of samples. For example, powders are finer and have more surface area; therefore heat is able to pass through them at a faster rate than that of a drop or a chunk. This negates the assumption that the appartuses are opperating under zero-demensional anaylsis.

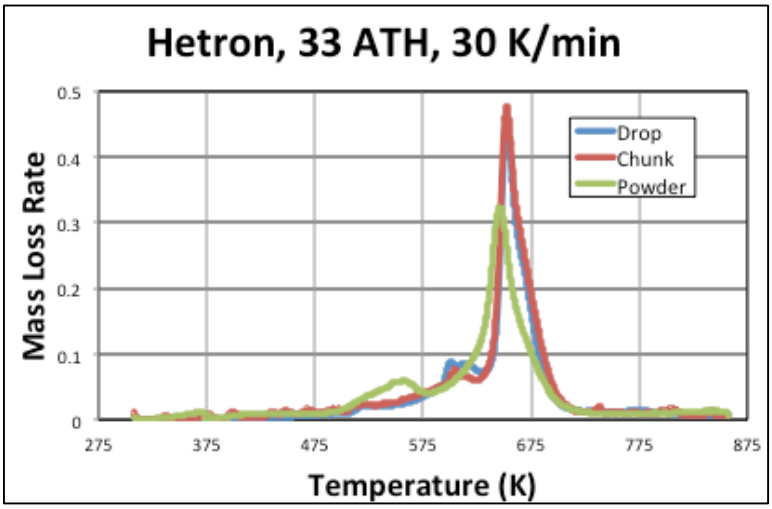

Figure 4: Observing Transport Effects with a Variety of Morphologies of Hetron, 33 ATH, 30 K/min

Figure 4 shows the comparision of the mass loss rate curve for various sample morphologies. It can be seen that the chunk and the drop follow a similar trend in mass loss rate as the temperature is increased. A transport effect can be most prominently seen in the powder where the first peak is shifted about 75 Kelvin, and the second peak is significantly lower than the other morphologies. While this comparison shows a transport effect in the Hetron-ATH mixture (100:33), this effect can be seen to some extent in all of the resin and additive mixtures.

Testing the Fireblock-Sand mixture elucidated some potential uncertainties with the small scale nature of the TGA and DSC. Due to the finer particles of ATH, a more homogenous mixture is produced when mixed with the liquid resins. The Fireblock-Sand mixture presents a different case due to the potential variance in the sand. An average sand particle can range in size from 0.01 mm to 0.60 mm.[12] Considering the average sample drop diameter of 3 mm, a sand particle has the potential to occupy anywhere between

approximately 0.0033 – 20% of the diameter. With TGA and DSC requiring small scale, this potential variance significantly increases the probability that a drop may not actually contain its intended composition. It is possible that to acquire valuable data for this kind of mixture, scale up to testing on the cone calorimeter may needed. Examples of varying composition can be seen in Figure 5.

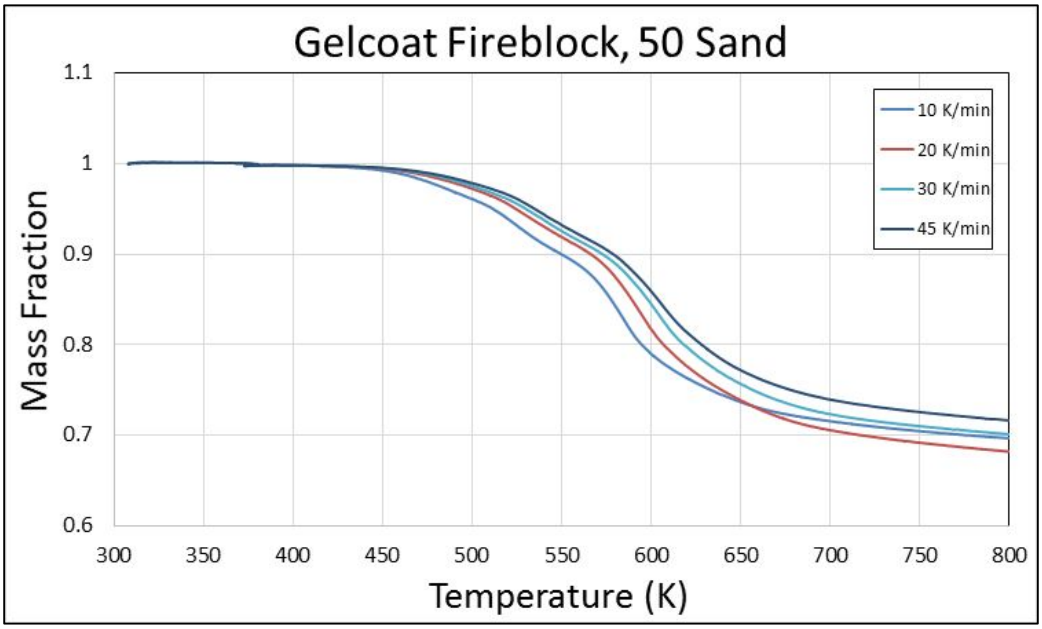

Figure 5: Fireblock-Sand (50:50) multiple heating rates

In Figure 5, an example of the irregularities can be seen in the sample heated at a rate of 10 K/min since it does not follow the same trend as the other three heating rates. The 10 K/min irregularities may potentially be an effect of the lower heating rate allowing for more time for gases to expand and pyrolyze; however the difference in final mass fractions supports the theory that the sample compositions may not be overtly accurate. Mass fraction differences are expected to be seen in various ratios of Fireblock to sand because of the inert property of sand. Differences in the final mass fraction of the same ratio translate to the inaccuracy of the composition of the sample. These abnormalities seem to become amplified with increasing sand composition. No further testing and analysis was completed with the Fireblock because of these abnormalities. The complete Fireblock data set can be viewed in Appendix J: Ashland Fireblock Gelcoat.

Fireblock, as well as Ampreg, both contain an intumescent, which means as they are heated they swell in size. The sample swelling produced an error with the machine and therefore increased the abnormalities seen in these samples (Appendix K: Gurit Ampreg 21FR Data). Again no further testing and analysis was completed with the Ampreg because of these irregularities.

Looking more closely at the Hetron composites, the OFW isoconversional method was used to determine the activation energy of the mixtures. Key trends could be observed through the various steps in the analysis process. In Figure 6, it can be seen that as the heating rate is increased the time and the temperature at which the decomposition begins shifts.

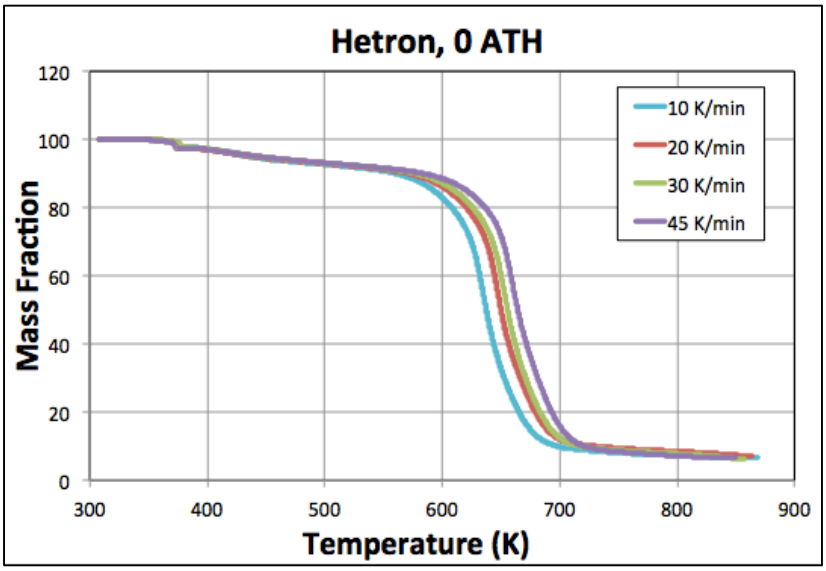

Figure 6: Observing the shifts due to varying heating rates in the decomposition

Examining specific mass fractions for the various heating rates, Figure 7 was generated by plotting the natural log of the heating rate (β) versus the inverse of the temperature.

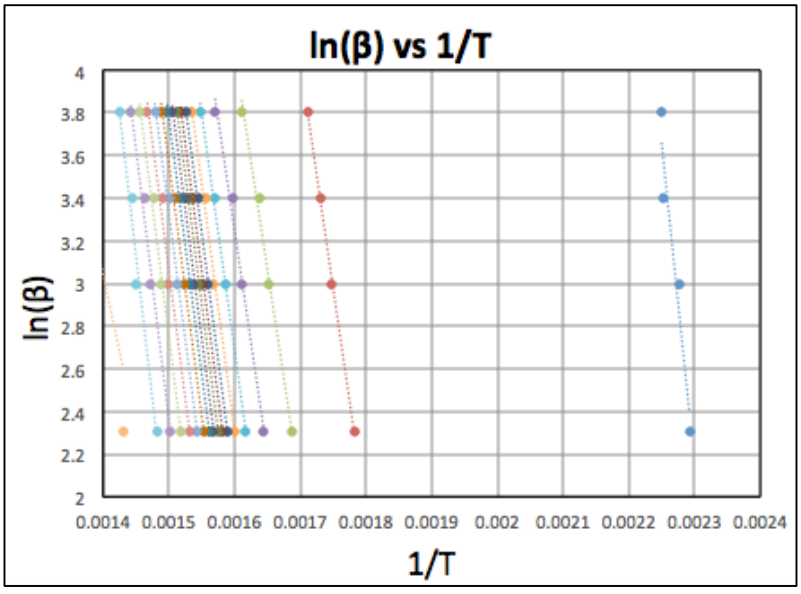

Figure 7: Intermediate step in the isoconversional method for Hetron-ATH (100:0)

The slope of the line in Figure 7 represents the activation energy of the decomposition reactions at a specific mass fraction. From these activation energies, Figure 8 can be developed.

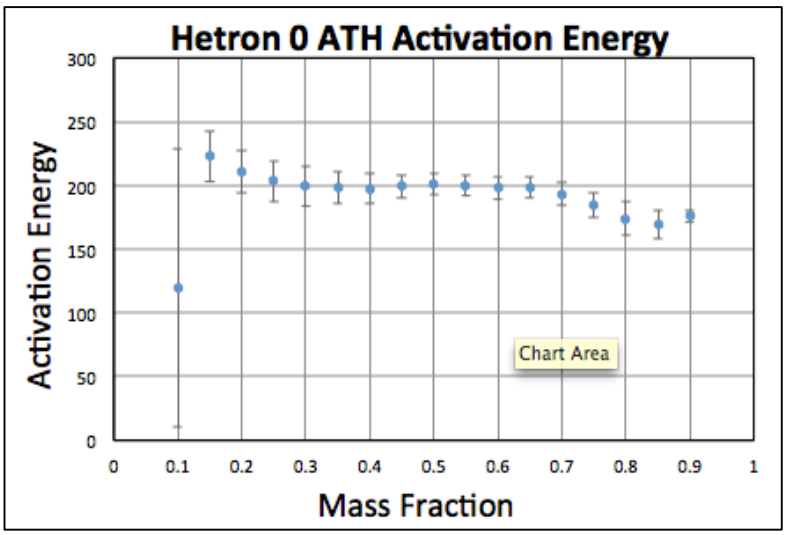

Figure 8: Observing activation energies during the course of the decomposition

Figure 8 illustrates that the trend in activation energy for Hetron is somewhat linear indicating a minimum of one reaction is taking place. More details on the process to developing Figures 7 and 8 can be found in Appendix F.1: Isoconversional.

Looking at the Hetron-ATH mixture data compared to the pure Hetron and ATH data, it was also observed that each peak in the mass loss rate represents various reactions taking place. Figure 9 is a graph of all Hetron-ATH mixtures and shows the mass loss rate of each at 30 K/min. The results for this heating rate are typical for all heating rates.

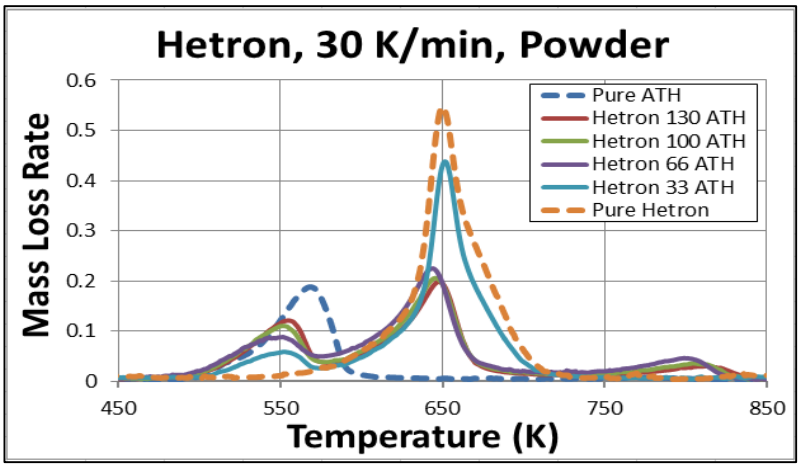

Figure 9: Observing Multiple Reactions with Hetron and ATH Mixtures, 30 K/min, Powder

The dotted blue and orange lines in Figure 9 show the pure Hetron and ATH and illustrate a minimum of one reaction is taking place. However, when the two components are combined, there are two distinct peaks therefore at least two decomposition reaction are occuring.

Results

Mass Loss Rate Model

In order to model mixtures, an ideal mixing model was implemented. From the isoconversional method, the pure Hetron and pure ATH samples were modeled under the assumption that their respective mass loss rate peaks were single reactions. An additive approach was used to model the multiple peak mixtures that treated each peak as an independent reaction in which the optimized characteristics of each component were proportioned relative to their percentage in the mixture, r. For a two component mixture the following equation was used to calculate alpha at each time step:

$$\propto_{total}(t) = f_1 r_1 \propto_1 + f_2 r_2 \propto_2 \qquad \text{(Eq. 3)}$$

$$f_n r_n = Z_n \qquad \text{(Eq. 4)}$$

Table 2 below shows the optimized parameters used for each Hetron-ATH mixture, and Table 3 shows the scaling constants used to proportion the parameters in the ideal modeling mixture. Following the tables are the modeled mass fraction and mass loss curves for powder and drop mixtures at 30K/min.

Table 2: Optimized Parameters for pure Hetron and ATH

Optimized Parameters	Pure Hetron	Pure ATH
Activation Energy, Ea	195.37	140.1
Pre-exponential Constant, log A	13.7	11.4
Exponent, n	1.125	1.25
Weight-loss fraction, f	0.94	0.34

Table 3: Scaling Constants of Hetron and ATH

Mixture Ratio Hetron : ATH	Scaling Constant, Z_{Hetron}	Scaling Constant, Z_{ATH}
100 : 33	0.707	0.084
100 : 66	0.566	0.135
100 : 100	0.47	0.17
100 : 130	0.409	0.192

Limitations for this simplified, ideal approach were apparent in modeling Hetron and ATH mixtures. Variations due to transport effects and morphology were seen between the experimental and modeled mass fraction and mass loss rate histories. Drop and powder mixtures of Hetron-ATH (100:66) heated at 30 K/min are shown below to represent the modeling limitations observed among all mixture ratios and heating rates.

In Figure 10, the experimental and modeled mass loss rates and mass fractions of a drop sample were graphed against temperature. In the mass loss rate curve, transport effects are seen in that the modeled ATH mass fraction peak is shifted to a lower temperature in comparison to the experimental data. This shift, apparent in all drop mixtures, was believed to be the result of the ATH parameters being optimized for a powder sample.

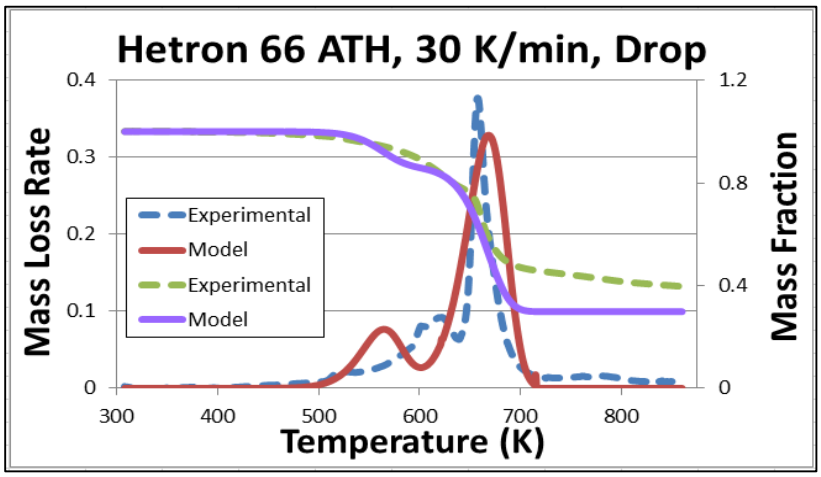

Figure 10: Model Fit of Hetron 66 ATH Drop

It was also observed that the model underestimates the peak of the Hetron mass loss rate peak, while overestimating the temperature range in which the Hetron was decomposing. This discrepancy was further supported by the mass fraction graph where the experimental and modeled final mass fractions are not equal. Since an additive approach was taken to model the two "independent" reactions, the heightened experimental peak is a result of the ATH and Hetron peaks joining around 650 K. While matching the temperature range of the experimental data, the modeled mass loss rate peak of pure Hetron covered more area than the experimental peak due to the symmetrical nature of the model. This overestimation was then carried over into the modeling of mixtures.

In Figure 11, the experimental and modeled mass loss rates and mass fractions of a powder sample were graphed against temperature. This graph shows that the overall behavior of the model was more similar to the experimental powder sample than the drop sample, but with its own set of limitations.

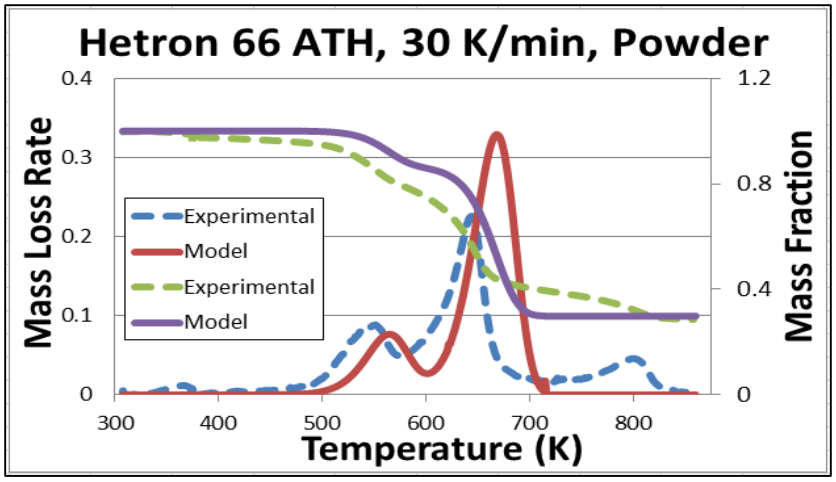

Figure 11: Model Fit of Hetron 66ATH Powder

In this case, the model overestimates the Hetron mass loss rate peak of the powder. Since the final mass fractions of the model closely match that of the experimental, it shows that the integrals of the model and experimental data are equal. However, additional peaks are seen in the experimental powder data that are not accounted for in the ideal mixing model. Throughout testing, powder had proven to be more variable in its decomposition; most likely the result of variable surface areas during experimentation. The complete set of Hetron and ATH decomposition models can be seen in Appendix I: Hetron Mixtures: Ideal Mixing Model.

Heat of Decomposition Model

The effect of morphology on sample behavior can also be seen when studying heat flow. Figure 12 shows data for Hetron 0 ATH sample drops run at both 5 K/min and 10 K/min. Here, it can be seen that the drops produce repeatable results, with key peaks occurring at similar temperatures and being of similar size.

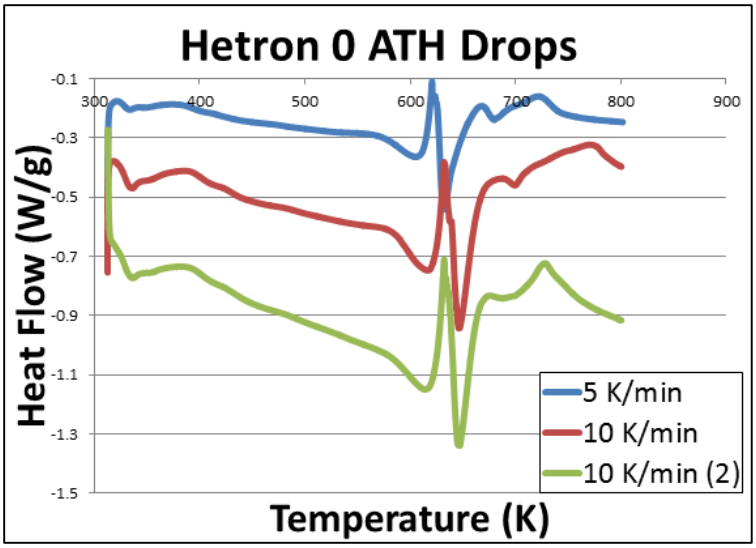

Figure 12: Hetron 0 ATH Drop Samples Heat Flow

Figure 13 shows data for Hetron 0 ATH sample powder run at both 5 K/min and 10 K/min. Here, it can be seen that the powders do not produce repeatable results.

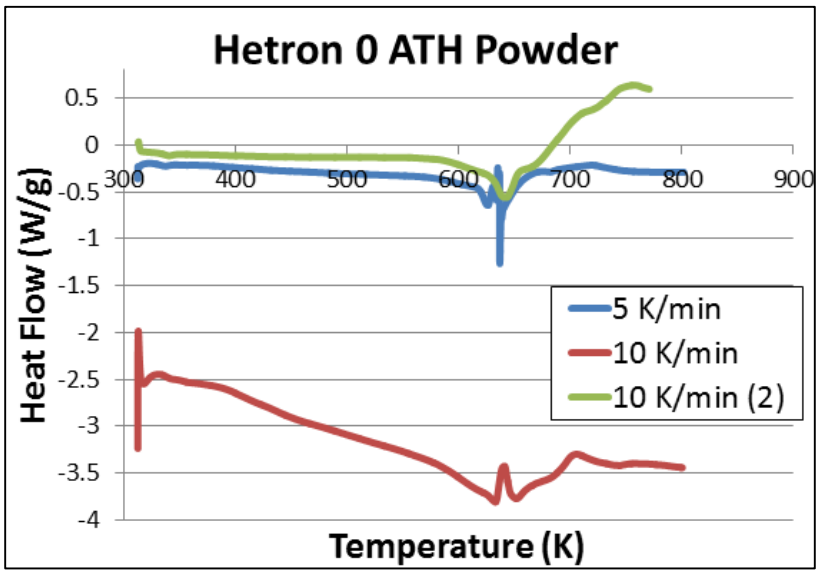

Figure 13: Hetron 0 ATH Powder Samples Heat Flow

Differences between the drop and the powder are expected, however the powder is inconsistent with itself. The peaks do not occur at the same temperature, sometimes do not occur at all, and the overall shape varies greatly between each sample.

The Hetron and ATH were first studied individually; it was determined that the heat of decomposition for ATH powder was 1000 J/g, and the heat of decomposition for Hetron drops was 62 J/g and 172 J/g for

powder. This significant difference between the morphologies of Hetron further highlights transport effects.

By plotting the heat of decompositions of pure Hetron and ATH with those of the mixtures, it was determined that the heat of decomposition can be predicted using an ideal mixing approach, as in Equation 5.

$$H_M = H_H + (H_{ATH} - H_H)x \qquad \text{(Eq. 5)}$$

$where: H_H\ is\ heat\ of\ decomposition\ of\ pure\ Hetron$

$H_{ATH}\ is\ heat\ of\ decomposition\ of\ pure\ ATH$

$H_M\ is\ heat\ of\ decomposition\ of\ mixture$

$x\ is\ the\ percent\ ATH\ present\ in\ the\ mixture$

Figure 14 shows the heats of decomposition determined experimentally for the Hetron and ATH mixtures for drops and powders plotted against ideal mixing models.

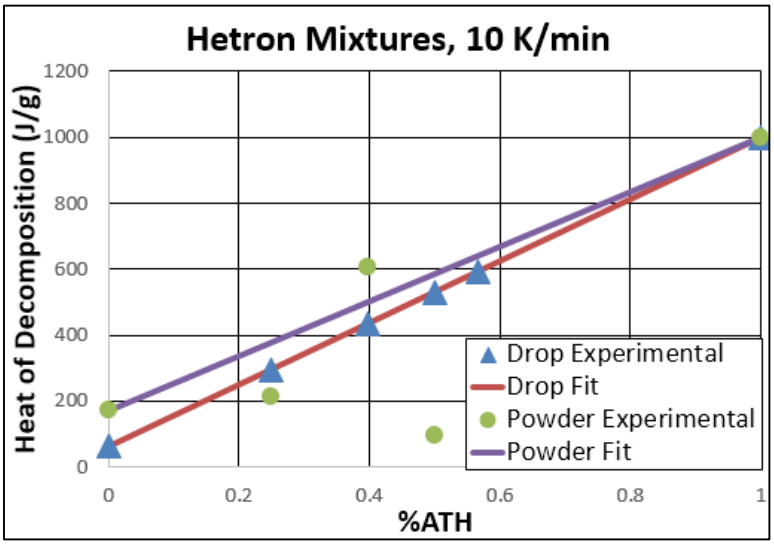

Figure 14: Ideal Mixing Model versus Data for Hetron and ATH Mixtures with Powder and Drop

It can be seen that the drops follow their mixing model very closely, yielding uncertainties less than 1%. However, it can be seen that the powder varies significantly, producing uncertainties on the order of 10-20%. This is due to the transport effects present in the powder that have been noted in other instances as well. It is especially important to note that the drops are more consistent because they are a solid, uniform mass, whereas the powder can shift on the pan. This leads to highly repeatable results with the drops, and more variation with the powder. The powder should follow the ideal mixing model as well, but more data would be needed to show this.

Chapter 5: Conclusion

From the observations and results, conclusions were drawn regarding sample decomposition and the application of kinetic models. First, transport effects were observed in the mass fractions and mass loss rates of samples. Apparatus transport was to be expected as the TGA and DSC measure thermocouple temperature, not the exact specimen temperature; however these effects were also apparent as a result of differing sample morphologies. It would be the recommendation of this study that morphologies similar to drops be used for similar research due to the observation that powder samples had proven to be more variable in their behavior, as well as the notion that drops would be more comparable to the applied material.

Second, simplified kinetic models similar to the one followed in this study can be applied, but there are limitations that should be noted. While this model provided insight to the decomposition behavior of Hetron and ATH mixtures, morphology and reaction complexity affected the accuracy of the model. When using a simplified, idealistic model, these variables were not taken into account. The development of a more complex model that could handle transport effects and more complex reactions would provide more realistic results, and would perhaps allow for mixtures like Fireblock and sand to be modeled.

Third, heats of decomposition can be predicted for mixtures based on their individual components. Morphology again needs to be considered in this ideal mixture model.

This research has potential for further exploration. The observations seen in this study, specifically regarding transport effects, are not directly discussed in the literature. The apparent role that these effects have on the analysis and modeling of materials therefore opens new avenues for investigation. Further testing on different FRP materials and various ratios of components would help to develop more accurate complex models. Developing a model that could mathematically account for transport effects could also help eliminate discrepancies in the data.

Appendix A: Computational Programs

Fire Dynamics Simulator (FDS) is a computational modeling program developed by the National Institute of Standards and Technology (NIST) which emphasizes smoke and heat transport from fires. FDS is most often accompanied by Smokeview, a visualization program that allows users to display the programs outputs. The program also has the capacity to connect with third party programs which allows other programs to provide input parameters. A paper published by NIST outlines the prediction of the mass loss rate of polymer materials evaluating FDS versus Thermakin. Both FDS and Thermakin use similar energy, mass and species balances but differ in the way input parameters are entered numerically. The paper concludes that if care is taken with the temperature dependence of input parameters, that FDS and Thermakin reproduce tests closely, most often within 4%. Additionally, FDS models decompositions kinetics using an Arrhenius type expression which allows for decompositions of solid phase components to be modeled.

The Generalized Pyrolysis Model for Combustible Solids (GPYRO) is a modeling program which simulates thermo-chemical processes occurring in simulated solids. GPYRO can be used in 0D, 1D or 2D simulations and conveniently couples to V 5.2.3 of FDS. It can also be used to estimate material properties from lab tests like TGA and DSC. With TGA, it is primarily used to estimate reaction kinetics, and with DSC it is most often used to estimate heats of reaction. Additionally, GPYRO allows the user to input as much or as little complexity as desired.

At its highest level of complexity, GPYRO has the ability to solve multi-dimensional conjugate heat transfer, fluid flow evolution, temperature dependent thermo physical properties, multi-step heterogeneous decomposition kinetics, and more. In regards to the kinetic aspect of GPYRO, it can be used to analyze data. GPYRO contains a material property estimation program which has the capacity to estimate material properties from tests including TGA and DSC. Overall, the heat transfer aspect of the program is more defined and definite, as opposed to the kinetic aspect, which is more estimated and has more room for error and variation. GPYRO models, while able to handle a full range of complexities, still make estimates in many cases as to the material properties. Like its full range of ability, GPYRO is used for a range of problems - including thermal pyrolysis studies, TGA & DSC experiments, heating and swelling of intumescent coatings, and thermal resistances.

Thermakin models gas-phase mass transfer within a solid phase material. Thermakin model is a flexible two-dimensional model of burning for pyrolyzable solids. It takes into consideration convective and radiative heat transfer, mass transport, and multiple chemical reactions taking place in the condensed

phase. The model solves for the transient mass and energy conservation equations and calculates the rate of gaseous fuel production from the physical and chemical properties of the solid. Thermakin is good for gas-solid interactions that enable the gas driven sample and expansion simulations; additionally the model can handle multiple components with multiple reactions. Stanislav Stoliarov is a professor in the fire protection department at the University of Maryland. He has numerous publications and is most well-known for his work developing Thermakin modeling and his work on the kinetics and thermodynamics of pyrolysis of combustible solids. Some of Stanislav's work moves towards a goal similar to ours - determining the often unknown or estimated physical and chemical properties of material components. With DSC he conducted tests measuring mass loss kinetics and reaction heat flow measurements. Thermakin was used as a numerical pyrolysis model to analyze mass loss kinetics. Thermakin is utilized in the study of burning of pyrolyzable solids, where it was used to calculate the rate of gaseous fuel production. Thermakin enables the modeling of pyrolysis and combustion with complex thermal degradation chemistry. From Stanislav Stoliarov's many uses of Thermakin, it is clear that it is a flexible software. Many uses of the modeling framework, include its uses in kinetic studies to larger studies on flame spread and growth. It is also being used for development of pyrolysis models for layered and non-homogeneous composites.

Appendix B: Fiber Reinforced Polymers

Fiber reinforced polymers (FRP) are composites that have been used to reinforce surfaces and structures.[13] They provide many benefits in the construction industry in surface aesthetics, corrosion prevention, high strength and stiffness, are low cost, and lightweight. This technology has improved the safety, economy, and functionality of structures being built. The main problem with them is making sure that the composites meet fire safety standards. One company on the cutting edge of FRP composites is Kreysler & Associates based out of Canyon, California.[14] The company specializes in the design, engineering, and manufacturing of composites for architecture, sculpture, and industrial application. FRP are made with a combination of fiber reinforcements, resins, fillers, and additives.

Fiber Reinforcement

There are three main fiber reinforcement categories: glass, aramid, and carbon.[13] Glass is the least expensive and carbon is the most. There are three different types of glass fibers used, e-glass, s-glass, and c-glass; which are used for electrical purposes, high strength, and high corrosion resistance respectively. Aramid fibers are made out of organic materials and provide excellent creep and fatigue resistance to the composites. An example of aramid fibers is Kevlar. Carbon fibers, the most expensive, have very high fatigue and creep resistance as well as have low strain at the point of rupture.

Resin

The resins in FRP allow for high compressibility strength and hold the fibers together.[13] There are two classes of resins, thermoplastics and thermosets. Thermoplastics remain solid at room temperature, melt when heated, and solidify when cooled. However they do not cure permanently and therefore are not good for structural applications. Thermosetting resins cure permanently and therefore are the most commonly used resins for structural applications. Both types of resins are highly expensive so in order to control material cost fillers are added to fill in the voids in the composite mixture. There are three main kinds of resins:

Acrylic

Acrylic resin is a thermoplastic that can be heated and manipulated repeatedly. It is mixed from a polymer, dry powder, a methyl methacrylate monomer, a thin liquid, and organic peroxide.

Polyester

Clear liquid that is mixed with a strong catalyst which causes the mass to cure during heating. It is a thermosetting plastic which means that it cannot be repeatedly manipulated. It is versatile and is not a hard as Acrylic.

Epoxy

Epoxy resins are very similar to polyester resins however they do not have as strong a smell. When epoxy resins harden that often have stronger mechanical properties as well as high temperature and chemical resistance.

Additives

One of the main issues with FRPs is their lack of fire retardancy, therefore many manufactures often use additives to produce that physical property. Additives typically improve the material properties, aesthetics, manufacturing process, and the performance of the composite.[13] Additives can be separated into three main categories: catalysts, promoters, and inhibitors; coloring dyes; and releasing agents. Two of the main additives used as a flame retardant are Aluminum Trihydrate (ATH) and Halogenated Compounds.

ATH acts as a flame retardant because it does not evaporate under the influence of heat therefore decomposing and producing non-flammable gases and water in an endothermic reaction.[15] In the gas phase, this mixes with the flammable gas, shielding the surface of the polymer against oxygen attack. ATH is effective through multiple routes:

1. It dilutes the amount of fuel available to sustain combustion during a fire by replacing part of the resin
2. Contain 34.6 % water that is released at high temperatures which provides a blanket effect and limits the oxygen available
3. It absorbs heat from combustion which reduces continued burning
4. Produces a char during burning that results in further flame retardancy and less smoke

However, ATH resins often negatively affect the properties of composites. Other downsides are that high loadings are required to meet ASTM standards and it often does not settle to reinforcements and therefore causes them to be more brittle. ATH reaction breaks down into aluminum and water which helps it act as a flame retardant. Overall there are many benefits to using ATH as a FRP resin. Halogenated compounds are very common as a fire retardant. However, there are downsides to working with halogenated compounds as well. For example, brominated compounds often times produce excessive toxic products and give off smoke when exposed to a flame.

Appendix C: NFPA and ASTM Standards

Due to the energy crisis in the 1970s, insulation was starting to be used more frequently as an energy savings measure.[16] The plastics industry encouraged the use of foam plastic insulation on exterior wall assemblies, but due to four of the five construction types requiring non-combustible components, the proposal was rejected. Later, the Society of the Plastics Industry consulted code and fire officials, and were challenged to design a testing method that would prove flame spread increase was not significant when foam plastics were involved. Finally in 1988, the Uniform Building Code (UBC) adopted a two-story full assembly test and allowed the use of foam plastics as insulation in exterior wall constructions. The National Fire Protection Association (NFPA) Committee on Fire Tests adopted the tests in 1998, and published it as NFPA 285, Standard Fire Test Method for Evaluation of Fire Propagation Characteristics of Exterior Non-Load-Bearing Wall Assemblies Containing Combustible Components.[17] It is important to note that the testing was done on the full wall assemblies not just the individual components. Even though individual components may be deemed usable, materials act differently in fires when tested alone compared to with other materials.

More recently, foam plastic insulation is not the only reason exterior walls are required to pass NFPA 285 tests. Water-resistive barriers, metal composite materials, fiber-reinforced plastics, and high pressure laminates, have all been added to the IBC requiring NFPA 285 testing. In previous years, the actual requirements for this testing have seemed to confuse architects, and many designers and code officials believed most structures were exempt from testing. However, NFPA 285-compliant wall assembly design and specifications are becoming more critical. In 2010, high rise building fires in the United States and China have shown that the entire exterior of a building can be engulfed in flames, even from a small ignition source.[18]

The main measurement evaluated for fire performance to follow NFPA 285 standards is the Flame Spread Test. During this test, a two-story structure with one room on each floor is constructed. Fires are set in the first floor room and in a window opening on the first floor. Externally, flames shall not reach ten feet above the window top, nor five feet laterally from the window's centerline to pass the NFPA test. Due to the high rise building fires, in 2012 IBC now requires wall assemblies to also meet additional requirements as laid out by ASTM E84 and the tunnel test.

The tunnel test was developed at the Underwriter's Laboratories by A. J. Steiner. The purpose of the test was to determine the fire hazard classification of building materials. The American Society for Testing and Materials (ASTM) adopted the test formally in 1961 as ASTM E 84. The NFPA adopted the tunnel

test as a standard in 1963. Since then, the test has been adopted by all four model building codes as well as regional and local code authorities.

For the test, the walls and floor in the tunnel are lined with firebrick, and the ceiling surface is constructed by the 24ft (7.3m) test specimen. The ceiling is exposed to a 4.5ft (1.4m) igniting flame with a heat release rate of 88 kJ/s based on the heat of combustion for methane. The flame covers a similar area than that of which would be exposed to flame if a large trash basket or small chair were ignited. During the test, air is drawn through the tunnel at a set velocity.

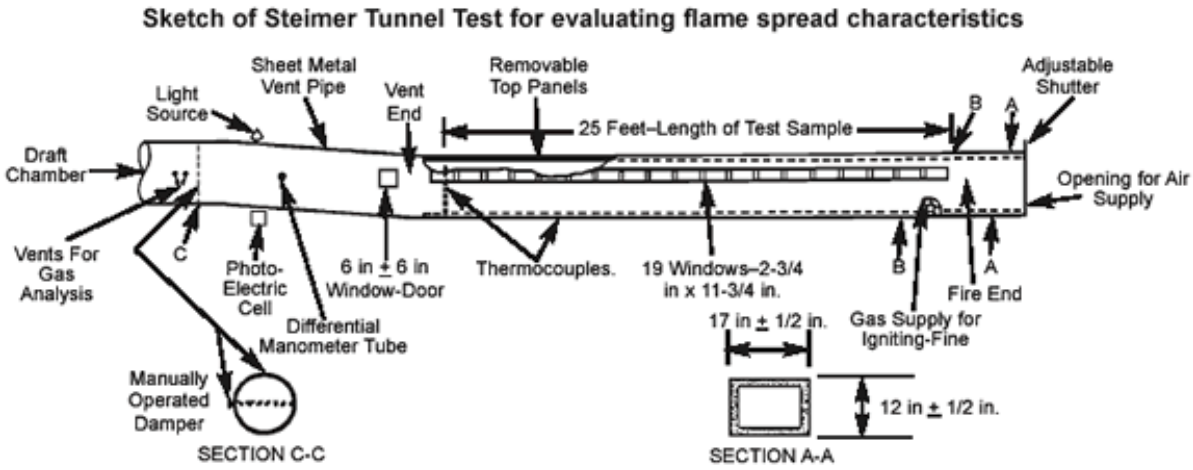

Figure 15: Steiner Tunnel Test Setup[16]

The determination of fire hazard classification is based on flame spread, fuel contribution, and smoke production. The flame spread classification (FSC) is based on the time required for the flame to travel beyond the end of the tunnel, or the maximum distance travelled at the end of the 10 minute exposure period. The fuel contribution (FC) is based on the area under the temperature versus time curve of a thermocouple placed "upstream" from the vent end over the 10 minute period. The smoke development classification (SDC) is based on the area under the light absorption versus time curve measured by the smoke meter outside of the tunnel over the 10 minute period.

Statistical evaluations were performed to determine the reproducibility of the tunnel test. William Parker took the lead in the investigation.[19] The FSC in the test was found to be highly dependent on the moisture content, brick temperature, preheat time, and specimen thickness, but was not dependent on draft velocity. Smoke development classification, however, was highly dependent on draft velocity. In

terms of the application of the test results to the development of fires in full scale rooms was also evaluated. In general, FSC below 25 have been classified as providing a high level of fire safety, however there is not necessarily a correlation between measured flame spread index and material behavior in actual fires. A series of tests was developed to better understand these scenarios. Open corner tests concluded that although the FSCs correlated with the tunnel tests, the speed in which the fire grew depended more on the density of the material than its FSC. Differing tests indicate the need for analytical models to explain how to use both tunnel test data and open room data to design parameters for a full scale application.

The burning characteristics of a material as defined by its heat release rate, ignitability, and flame spread rate depends on its incident heat flux. The incident heat flux is due to both radiation and convection. There are large differences found in open room tests and the tunnel test. Some of these differences arise when the flame comes in contact with a joist or corner in the room. Parker recommends that the ceiling-wall mounting could work with the tunnel test to indicate flame spread potential of materials near intersection of walls or wall and ceiling. The cohesion of these tests could indicate greater hazards in materials in terms of flame spread, than the tunnel would conclude alone. Room-corner tests in comparison to tunnel tests reveal some problems in the reproducibility of data. For one example, materials tested and classified with the with Steiner's test deemed the material acceptable in terms of flame spread index, where the room-corner test revealed the materials led to flash over and are not acceptable. Full-room and full scale test procedures like the room-corner test and the tests required by NFPA 285, allow products to be more efficiently evaluated because they are set up and tested in the same formation that they would be when encountering an actual fire. Therefore, these tests are more suitable for inputs of fire models for performance based design.

Appendix D: Thermogravimetric Analysis

Appendix D.1: Standard Operating Procedures

Fire Science Laboratory

TGA Checklist

Pre-Test

Ensure proper PPE is in use	_____
Turn on computer*	_____
Turn on TGA*	_____
Open "Compressed Air" valve at manifold	_____
Open "Nitrogen" valve at manifold	_____
Leak check purge gas hoses and connections	_____
Open TGA program through TA Instruments Software program	_____

Note any maintenance. * These items are normally left on.

_____

_____

Specimen Preparation

Select proper sample pan	_____
Place pan on control arm - pan must be flat on control arm	_____
Press "Tare" in program or on TGA to tare pan	_____

Use tweezers when loading pan. Also, use caution as the wire hanger will bend easily causing a problem during sample loading.

Test

Edit "Procedure" tab in software program	_____
Place specimen in pan[1]	_____
Place pan on control arm - pan must be flat on control arm	_____
Press "Play" or "Start run" in software program	_____

Post-Test

Ensure data has saved to specified location; if not "Transfer Data"[2]	_____
Ensure cooling air has stopped	_____
Remove sample pan, place in appropriate area to cool	_____
If running another test cool cell as needed and return to **Specimen Preparation,** if testing is complete, proceed[3]	_____
Close furnace by putting into the up position	_____
Close both valves at manifold	_____
Close TA Instruments software	_____

[1] Sample should be approximately less than 10mg
[2] See "Guidelines" for directions to use this function
[3] Be sure to clean the sample pan between runs; see "Guidelines" for recommendations

Filename: tgasopcheck.doc Last Revised: 17 April 2014

Appendix D.2: Calibration Methods

In order to be confident the TGA is producing sound data, it is important to calibrate it. This was done in accordance with the TA standard "TGA Temperature Calibration Using Curie Temperature Standards" using TGA 358 and TGA 153. This method utilizes the transition of a ferromagnetic material from magnetic to unmagnetized at its Curie temperature. By placing the sample in a tarred TGA pan, placing a magnet at the bottom of the furnace, and heating the sample above its Curie temperature, the accuracy of the TGA temperature readings was assessed. At the Curie temperature, a distinct change in weight can be observed; if the TGA shows this change at the correct temperature, it is said to be calibrated.

We used two different samples to assess the calibration of our TGA. Figure 16 shows the test with TGA 358. This material has a Curie temperature of 358C. At approximately 570K, the magnet was moved near the furnace, causing an increase in mass. At 615K (342C) a decrease in mass occurs; this corresponds to the Curie temperature of the material. Our machine is within 4.5% of the accepted value, so we determined it was calibrated. Figure 17 shows the test with TGA 153. This material has a Curie temperature of 153C. With this sample, the magnet was in close proximity from the start of the test. At 420K (147C) a decrease in mass occurs; this corresponds to the Curie temperature of the material. Our machine is within 3.9% of the accepted value, so we furthered verified that it's calibration.

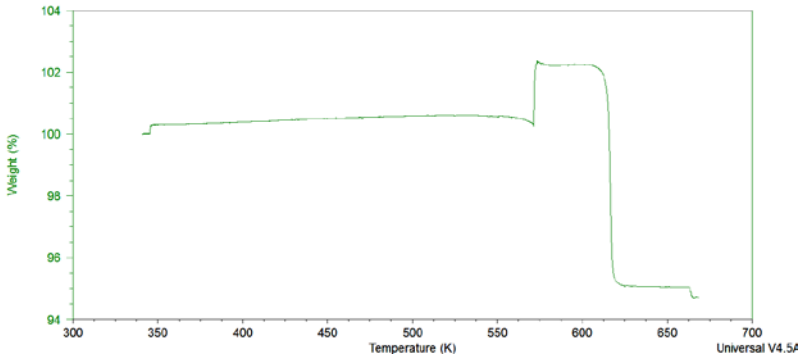

Figure 16: TGA 358

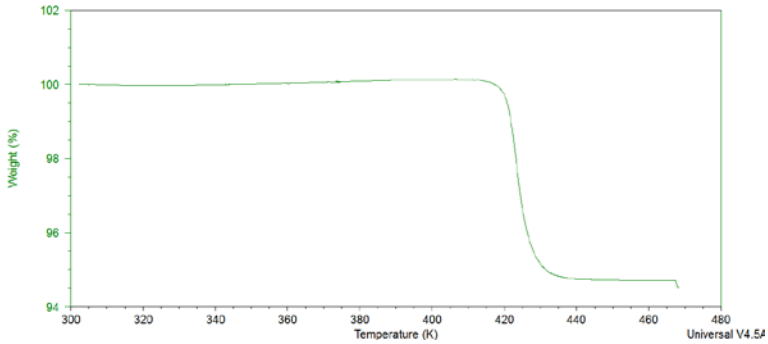

Figure 17: TGA 153

Appendix D.3: Testing Procedure

The following procedure was used to complete all testing with the TGA; ASTM D3850-12 was used.

1. Prepare sample (1-10 mg)
2. Equilibrate at 35 ^{o}C
3. Heat at selected rate to 100 ^{o}C
4. Hold isothermal
5. Continue heating to 600 ^{o}C

Appendix E: Differential Scanning Calorimetry

Appendix E.1: Standard Operating Procedures

Fire Science Laboratory

DSC Checklist

Pre-Test

Ensure proper PPE is in use	_____
Turn on computer*	_____
Turn on DSC*	_____
Open "Compressed Air" valve at manifold	_____
Open "Nitrogen" valve at manifold	_____
Leak check purge gas hoses and connections	_____
On computer desktop open TA Instruments Explorer	_____
Open DSC icon	_____

Note any maintenance. * These items are normally left on.

_____

_____

Specimen Preparation

Select proper sample pan and lid	_____
Weigh sample pan and lid, empty; tare	_____
Place sample in pan	_____
Weigh sample in pan and lid; record weight in program	_____
Crimp pan and lid together in press	_____

Use tweezers to handle sample pans and to remove cell covers. Use caution when crimping pans to ensure no obstructions are present in jig.

Test

Set test parameters in TA Instruments	_____
Remove chamber lid, using tweezers	_____
Remove both cell lids, using tweezers	_____
Reference pan should be in furnace, if not place on rear left sensor	_____
Place sample pan in furnace on front right sensor	_____
Replace cell and chamber lids	_____
Begin test	_____

Post-Test

Ensure data has saved to specified location; if not "Transfer Data"	_____
Remove chamber lid, using tweezers	_____
Remove both cell lids, using tweezers	_____
Remove sample pan, place in appropriate area to cool	_____
Dispose of sample pan in proper waste receptacle	_____
If running another test cool cell as needed and return to **Specimen Preparation,** if testing is complete, proceed	_____
Close both valves at manifold	_____
Close TA Instruments software	_____

Filename: dscsopcheck.doc Last Revised: 17 April 2014

Appendix E.2: Calibration Methods

Due to large uncertainty in DSC measurements, it is important to calibrate the DSC often.[20] We performed Baseline and Cell Constant calibrations daily to ensure the highest accuracy. Our calibration results can be seen Table 4.

Baseline Calibration

The Baseline Calibration was performed using an empty cell and should be run whenever testing parameters – such as heating rate, temperature range, and pan type – change significantly. The TA DSC20 has a Calibration Wizard that was used. This calibration was run by selecting "Calibrate" from the main toolbar, then "Calibration Wizard". In the Wizard, "Baseline" was selected, and the parameters for this calibration should match the parameters for the tests being run later. Once the run was completed, the data was transferred by selecting "Tools" from the main toolbar, then "Data Transfer". Once the data was successfully saved, the calibration must be saved to the machine. This was done by selecting "Calibrate" from the main toolbar, then "Analysis"; Figure 18 shows the analysis view. The Baseline file was opened and "Accept" was selected to accept this calibration. When selecting a table to save the calibration to, keep in mind the new file will overwrite the existing one. The tables can be viewed by selecting "Calibration" from the main toolbar, then "Cell Constant/Table".

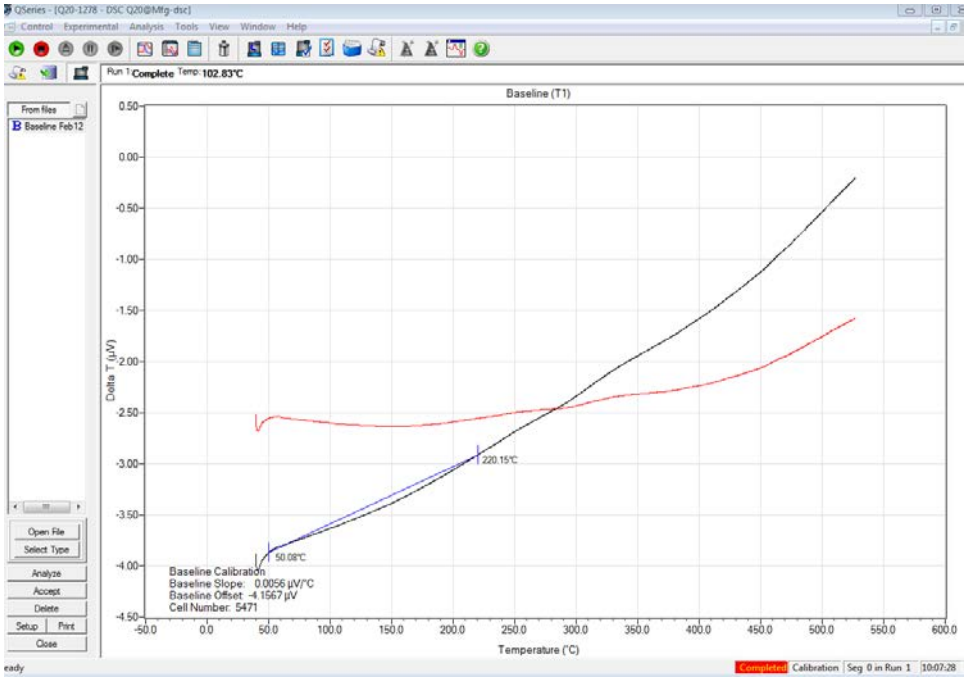

Figure 18: Baseline Analysis View

Cell Constant Calibration

The Cell Constant Calibration was performed using a standard sample, typically a metal. We used indium for all of our calibrations. Again, the Calibration Wizard was used, selecting "Cell Constant/Temperature" from the first screen of the Wizard. The parameters for the run should automatically adjust based on which material is being used. The only parameter that needed to be adjusted was the heating rate; this matched the heating rate being used in subsequent runs. Once the run was complete, the data was transferred by selecting "Tools" from the main toolbar, then "Data Transfer". Once the data was successfully saved, the calibration was saved to the machine. This was done by selecting "Calibrate" from the main toolbar, then "Analysis"; Figure 19 shows the analysis view. The Cell Constant file was opened and "Accept" was selected to accept this calibration. When selecting a table to save the calibration to, keep in mind the new file will overwrite the existing one. The tables can be viewed by selecting "Calibration" from the main toolbar, then "Cell Constant/Table".

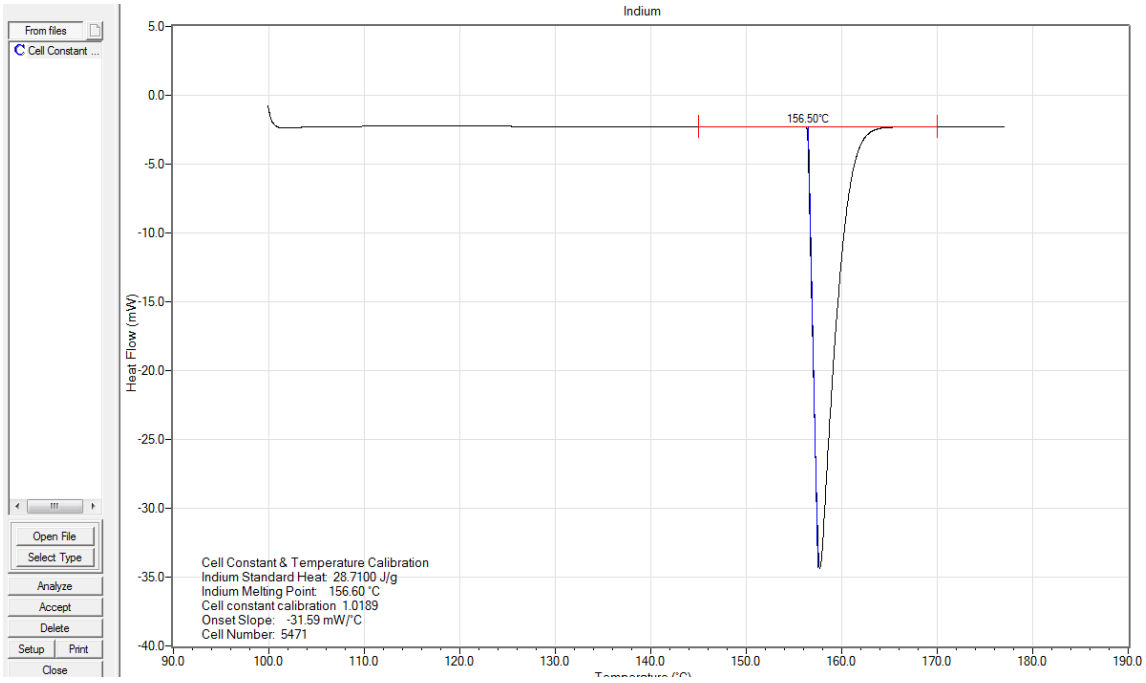

Figure 19: Cell Constant Analysis View

After all calibrations were complete, the calibrations were selected for use during testing; this was done using the Experimental Wizard.

Table 4: Calibration Values

Date	Baseline		Cell Constant
	Offset (microV)	Slope (microV/C)	
12-Feb	-4.1567	0.0056	1.0189
14-Feb	-3.6261	0.0047	1.0052
17-Feb	-3.6905	0.003	0.9643
19-Feb	-3.7888	0.0037	0.9992
21-Feb	-3.4865	0.0061	1.0588
24-Feb	-3.8271	0.0011	1.0467
26-Feb	-4.2604	0.0061	1.0793
28-Feb	-4.123	-0.0005	1.05
3-Mar	-5.0739	-0.0001	1.0636
5-Mar	-4.6009	0.0027	1.056

Appendix E.3: Testing Procedure

The following procedure was used to complete all testing with the DSC; ASTM D7426-08 & ASTM D3418-12e1 was used.

1. Calibration
   a. Baseline
   b. Cell Constant
2. Prepare sample (1-10 mg)
3. Heat at selected rate to 530 ^{o}C

Appendix F: Analysis Process

Appendix F.1: Isoconversional

To verify and calibrate the OFW isoconversional method before use on Kreysler samples, a well know material PMMA, was tested. Poly (methyl methacrylate) or PMMA is an important commercial polymer, used widely in a variety of industries. Valued for its rigidity and weathering ability. On the molecular level, PMMA begins to degrade at high temperatures. The long chain polymer backbone begins to separate and react, thus changing properties. Thermal degradation of PMMA occurs at 300 – 400 C (573 – 673 K). Physically, PMMA yields char and experiences a change in the molecular weight. PMMA was used in our process of verification and calibration of experimental testing and data analysis because of its common uses and the considerable availability of literature information on the polymer. TGA tests were run with PMMA samples at four different heating rates, 10, 20, 30, and 45 K/min. The resulting data was compared with the literature data of M. Ferriola, et al.[21] in which PMMA samples were tested at 2, 5, 8, and 10 K/min. The following steps illustrate step by step the OFW isoconversional method results and comparison to this literature for verification.

Following an Arrhenius approach, the temperature is recorded at each of the four heating rates at alpha values ranging from 0.1 to 0.9. With this data 1/T (K) versus the natural log of the heating rate ln(β), was graphed. The slope of the line for each alpha data set E_a/R, was recorded, seen in Figure 21.

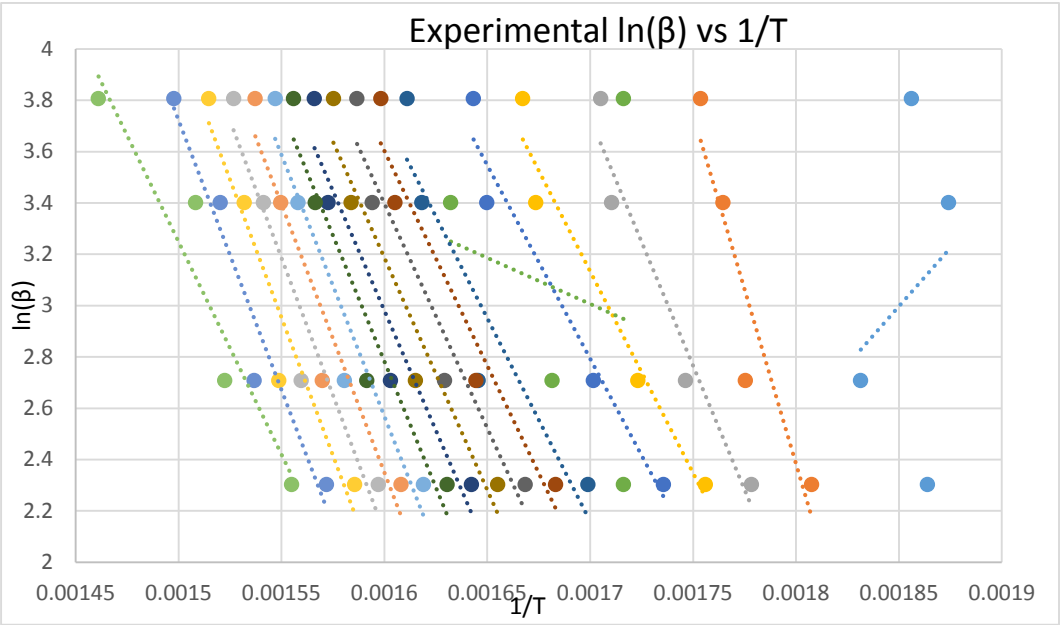

Figure 20: Experimental Results for ln(B) vs 1/T

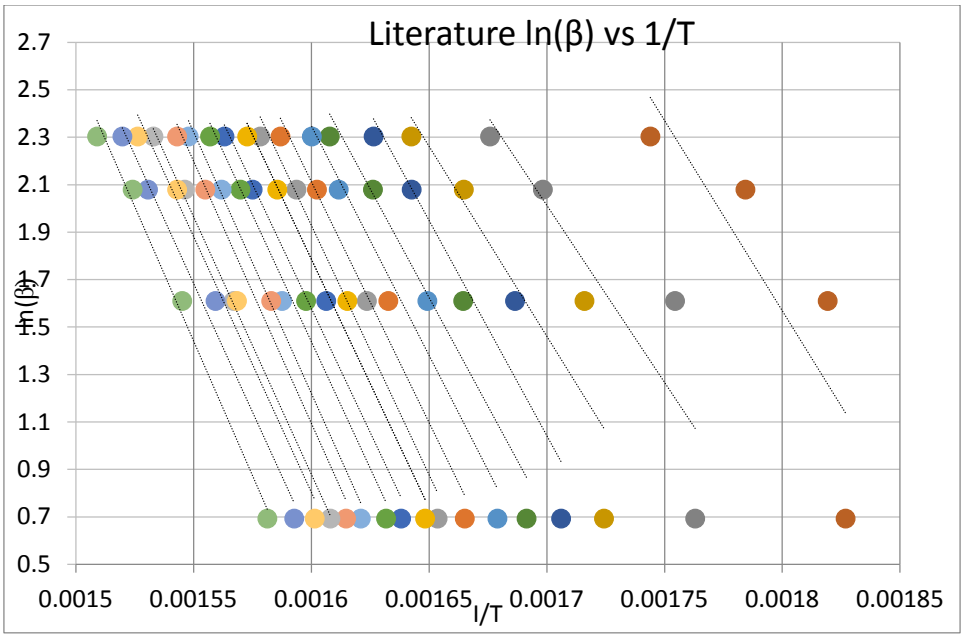

Figure 21: Literature Results for ln(B) vs 1/T

The slope at each alpha value is recorded and multiplied by 0.008314 kJ/mol K, the universal gas constant, in order to obtain the activation energy value. The error of the linear regression was determined by finding the error on each slope from Figure 22. The excel statistics function 'LINEST' was used to obtain slope error values.

Table 5: Experimental and Literature Activation Energy Determination

	Experimental		Literature	
α	Ea (kJ/mol)	Error (±)	Ea (kJ/mol)	Error (±)
0.95	-75.56	212.17	40.61	88.38
0.9	226.34	59.154	133.56	57.62
0.85	160.14	26.354	124.11	45.03
0.8	130.62	18.546	133.18	48.32
0.75	125.48	17.785	150.74	37.15
0.7	29.95	97.768	152.41	28.80
0.65	131.70	35.505	161.04	24.10
0.6	139.05	23.591	169.00	19.87
0.55	145.47	26.194	174.90	22.67
0.5	150.37	28.240	174.52	17.57
0.45	155.07	31.44	174.12	19.31
0.4	163.32	32.314	177.587	15.58
0.35	169.55	34.737	183.31	15.648
0.3	173.65	36.393	183.82	17.83
0.25	177.84	36.200	180.68	5.086
0.2	178.65	35.456	179.25	18.59
0.15	174.80	30.538	180.37	15.54
0.1	137.75	30.412	188.60	11.82
AVE	**158.74**	**±31.43**	**165.96**	**±24.74**

Activation energy versus alpha was graphed to determine the trend in E_a values and compared to the literature. Figure 23 can be seen below:

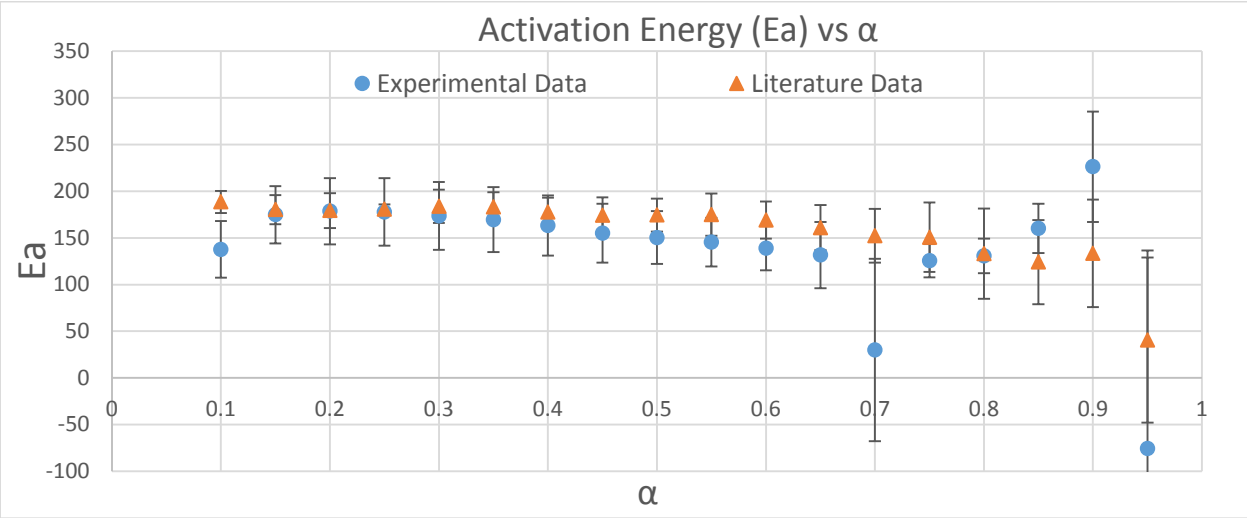

Figure 22: Activation Energy versus Mass Fraction

Examining the activation energy trends and error bars generated, the data shows a linear trend of the activation energy value. The average experimental activation energy value was 158.74 kJ/mol while the literature data yielded a comparable value of 165.96 kJ/mol. Both of these values found from using our data analysis process are similar to other literature information for PMMA including 247.27 kJ/mol (Flynn & Wall), 188 kJ/mol (Stas), and 153 kJ/mol (Ozawa). These values and trends are conclusive that our process yields data and calculations analogous to that of the literature values.

Single Heating Rate Method

In additional to the isoconversional method which considers multiple heating rate, the single heating rate method was also utilized in order to back up results. Data was reproduced from a TGA run testing a PMMA sample in a small 10 mg chunk shape. Utilizing a 45 C/min heating rate, the test was run with nitrogen as a purge gas. It was assumed that there is a single reaction occurring and that it is first order.

The constant heating rate is defined as $\beta = \frac{dT}{dt}$ and assuming a first order reaction rate of $f(\alpha) = (1-\alpha)^1$, the Arrhenius equation is considered:

$$\frac{d\alpha}{dT} = \frac{A}{\beta}\exp\left(\frac{-E_a}{RT}\right)(1-\alpha) \qquad \text{(Eq. 6)}$$

The data was graphed with temperature on the x-axis versus the rate of mass loss on the y-axis,

$$r_p = \frac{\Delta m/m_o}{\Delta t} \qquad \text{(Eq. 7)}$$

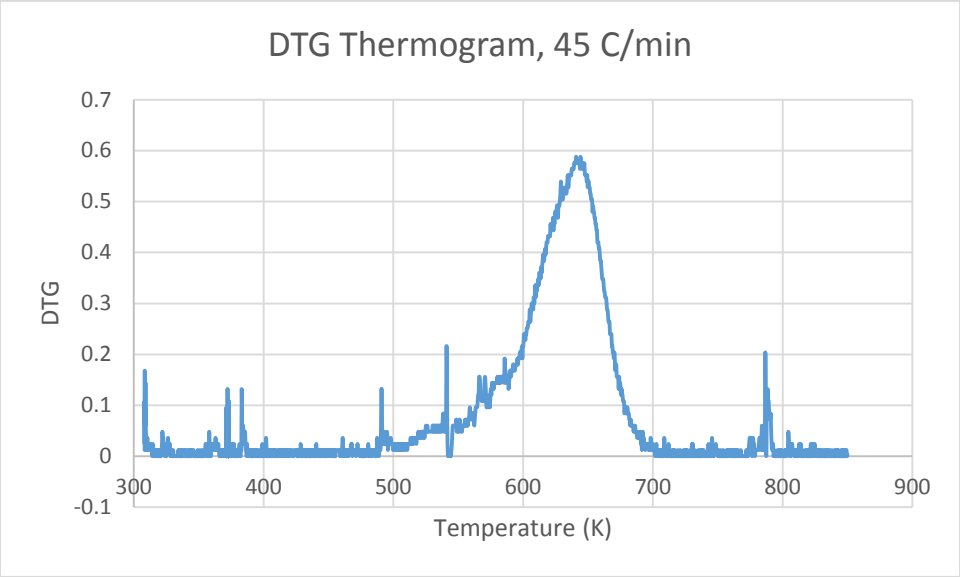

The peak point occurs at 644.2 K, and a DTG value of 0.5882. The gas constant of 0.00831446 kJ/mol*K was used. Ester's equations for activation energy and the pre-exponential factor were used:

$$E_a = \frac{RT_p^2}{\beta} * \frac{er_p}{1-\alpha_o} \qquad \text{(Eq. 8)}$$

$$A = \frac{er_p}{1-\alpha_o} * \exp\left(\frac{E_a}{RT}\right) \qquad \text{(Eq. 9)}$$

Equations 7 and 8 resulted in an activation energy value of 193.52 kJ/mol and a pre-exponential factor of 1.242 E 16 min^{-1}. The activation energy fits closely with various literature data of 188 kJ/mol (Stas) and 247.24 kJ/mol (Flynn & Wall). The pre-exponential factor A is later optimized via the Runge Kutta method.

Appendix F.2: Runge Kutta Modeling

This method is taken directly from Chapter 5 of Esther Kim's dissertation paper in an exercise to apply and validate her proposed kinetic modeling method.

After conducting the isoconversional Method, an nth order reaction model is utilized to estimate other kinetic parameters. The weight-loss fraction (f), pre-exponential constant (A), and the exponent of the model (n) are estimated in order to develop a complete mathematical description of decomposition. The flexibility of the nth order model allows it to provide a good fit between the experimental data and the theoretical model.

Equation Set Up

The Runge Kutta 4th order method (RK4) is applied to both the decomposition and constant heating rate ordinary differential equations for each reaction of a test specimen. The two ODE equations are:

$$\frac{d(1-\propto)(t)}{dt} = \left[Aexp\left(-\frac{E_a}{RT(t)}\right)\right](1-\propto(t))^n \quad \text{(Eq. 10)}$$

$$\frac{dT(t)}{dt} = \beta \quad \text{(Eq. 11)}$$

Since the heating rate (β) is constant we can solve the Runge Kutta using only the decomposition equation where α is the dependent variable, and time (t) is the independent variable. Per RK4, the following equations are used to develop the relationship between α and t.

$$k1d(1-\propto) = \left[Aexp\left(-\frac{E_a}{RT}\right)\right](1-\propto)^n \quad \text{(Eq. 12)}$$

$$k2d(1-\propto) = \left[Aexp\left(-\frac{E_a}{RT}\right)\right](1-(\propto + .5 * k1d \propto))^n \quad \text{(Eq. 13)}$$

$$k3d(1-\propto) = \left[Aexp\left(-\frac{E_a}{RT}\right)\right](1-(\propto + .5 * k2d \propto))^n \quad \text{(Eq. 14)}$$

$$k4d(1-\propto) = \left[Aexp\left(-\frac{E_a}{RT}\right)\right](1-(\propto + k3d \propto))^n \quad \text{(Eq. 15)}$$

$$\propto_n = \propto_{n-1} + (k1d \propto + 2(k2d \propto + k3d \propto) + k4d \propto)\frac{dt}{6} \quad \text{(Eq. 16)}$$

$$\propto(t) = \frac{m_o - m(t)}{m_o} \quad ; \quad \propto(0) = 0 \quad \text{(Eq. 17)}$$

By this definition of alpha at any given time, $\propto(t)$ represents the amount of mass that has been consumed up to that time. As noted previously, RK4 is applied for **each reaction of a test specimen.** So, for every reaction, an independent $\propto(t)$ value will be produced. The total decomposition of a sample in the kinetic model is then a sum of each reaction that has been scaled with its respective weight-loss fraction, f; where f represents the amount of weight (mass) that is consumed by each reaction.

$$\propto_{total} = f_1 \propto_1 + f_2 \propto_2 \ldots f_n \propto_n + f_{residue} \quad \text{(Eq. 18)}$$

If scaling is not applied, every reaction would result in 100% conversion meaning all of the mass would be consumed.

For the kinetic model, treat the activation energy (Ea) calculated from the isoconversional method as a set parameter. In multiple heating rate analysis, the isoconversional method calculates a series of Ea values over a range of mass fractions. This provides insight on the minimum number of elementary reactions that take place during decomposition. If the Ea values over the total decomposition are linear,

it is reasonable to use an average of this range as the set parameter. For more complex degradation, more than one Ea value will need to be applied to different reactions.

Adjusting Parameters

The DTG curve of the experimental data is graphed with the DTG curve of the RK4 calculated values in order to estimate parameters A and n. Initial guesses for the pre-exponential constant (A) and the exponent (n) are generally 10 and 1 respectively. When doing single heating rate analysis, use the calculated pre-exponential constant (A) as the initial value.

Adjustments to A effect the shape and size of the graph corresponding with the x-axis. The goal in adjusting the pre-exponential constant is to match the temperature ranges of the RK4 and experimental mass-loss peaks. An increase in A results in a wider and taller curve. Changes in n values range from 0-3 and result in changes in the shape of the DTG curve, where increasing n lowers the peak and widens the temperature range.

Appendix F.3: Heat of Decomposition

Data produced by tests run in the DSC can be used to calculate the heat of decomposition of materials. This is important in understanding the thermal properties and decomposition behavior of the Kreysler products.

In order to determine the heats of decomposition, the DSC data was plotted with the TGA data for Weight% and Derivative Weight% to see when the change in mass was occurring. For the samples heated at 10 K/min, the decomposition region was determined by the region of the peak of the Derivative Weight% curve; this coincided with visible peaks and changes in slopes on the DSC curve. For the DSC samples heated at 5 K/min, the decomposition region was determined by the peaks and changes in slope matching the ones in the samples heated at 10 K/min. Figure 23 , Figure 25, and Figure 25 show the determination of the heats of decomposition for two different samples heated at 10 K/min and 5 K/min using the “Integrate Peak Sig Horizontal” function in TA Universal Analysis.

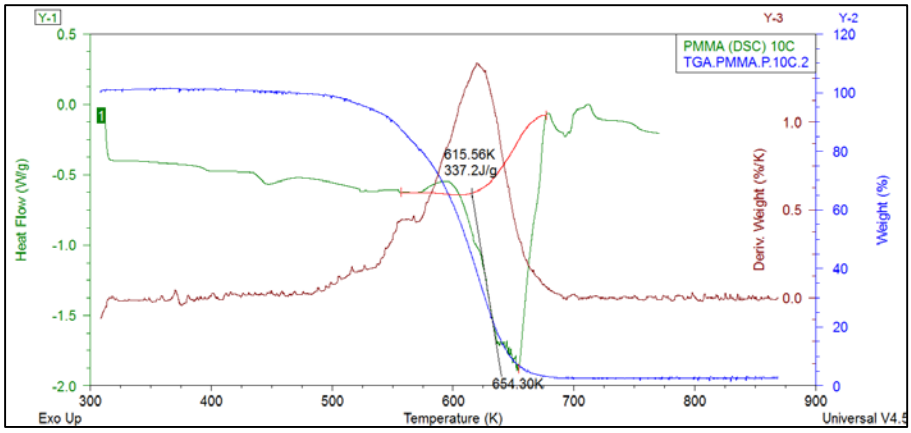

Figure 23: PMMA (Powder 10 K/min) Heat of Decomposition

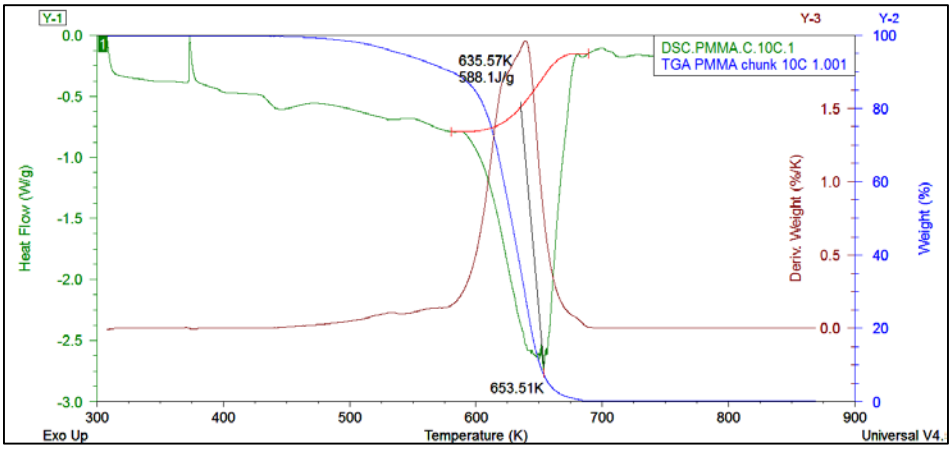

Figure 24: PMMA (Chunk 10 K/min) Heat of Decomposition

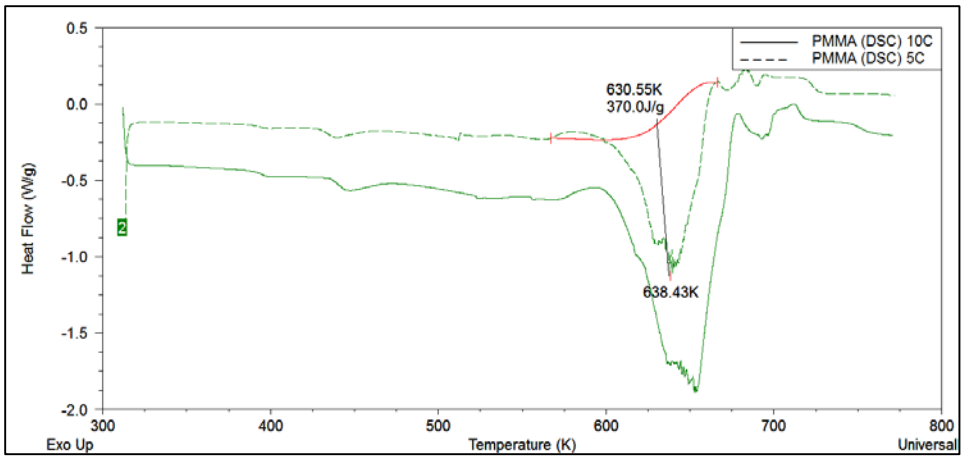

Figure 25: PMMA (Powder 5 K/min) Heat of Decomposition

It is interesting to note the large difference between the powder and the chunk samples, however this difference is consistent with other reported findings. Hung reports a value of 355 J/g for the heat of decomposition for PMMA; our values for the powder samples are within 5% of that, which is acceptable. On the other hand, Stoliarov reports a heat of decomposition of 870 $\pm$ 200 J/g; our values for the chunk samples are with 12% of this range. This is not ideal, but we must consider the differences in test methods. Stoliarov performed tests with squares of PMMA at a heating rate of 5 K/min while we tested non-uniform chunks, though of similar mass. For the intents of this case study, we can assume that our methodology and data are sound and that we can confidently proceed to analyze the Kreysler materials. When moving forward with testing, it is important to consider the differences in sample form observed here.

Appendix G: ATH Data

TGA tests were run with pure ATH samples at four different heating rates, 10 K/min, 20 K/min, 30 K/min, and 45 K/min.

Single Heating Rate Method

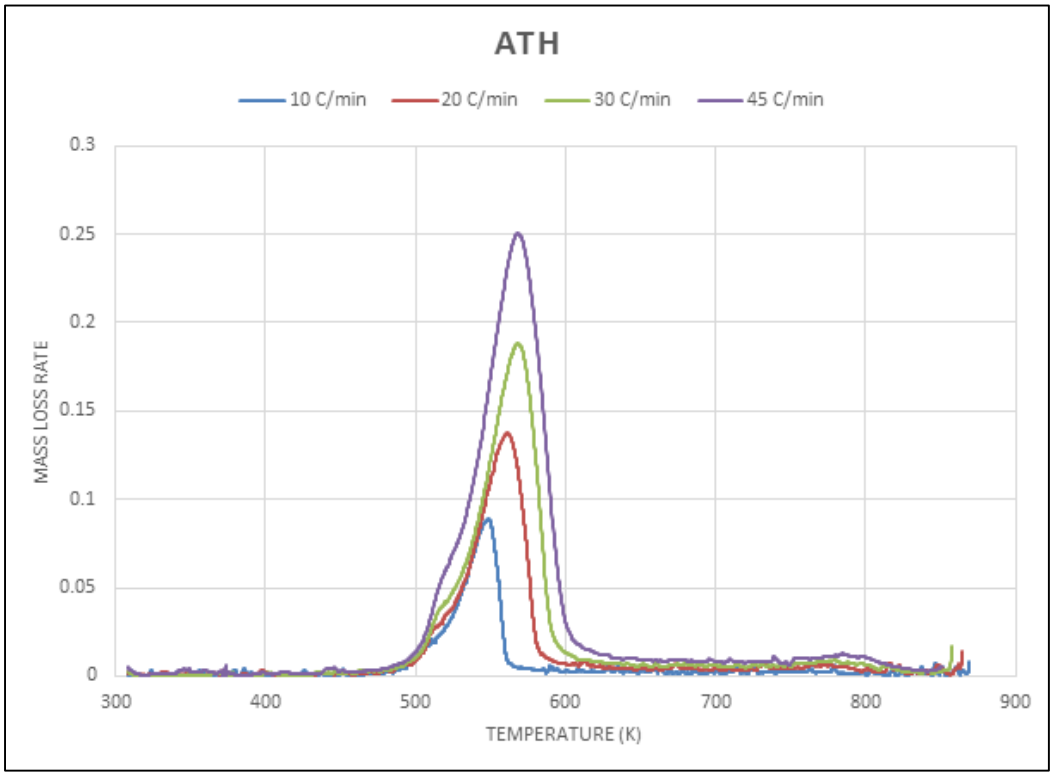

Figure 26: Single Heating Rate Method of ATH at Various Heating Rates

Single Heating Rate Method – Peak Temperature and Activation Energy

Table 6: Peak Temperatures and Activation Energies

Heating Rate (K/min)	Peak Temperature (K)	Activation Energy (E_a – J/mol)	Pre-Exponential Factor (A)
10	548.52	76426.975	5792960.55
20	561.1446	59856.7509	170557.539
30	568.115	55457.1962	77842.8702
45	566.6462	47680.7792	19967.7004

OFW Isoconversional Method

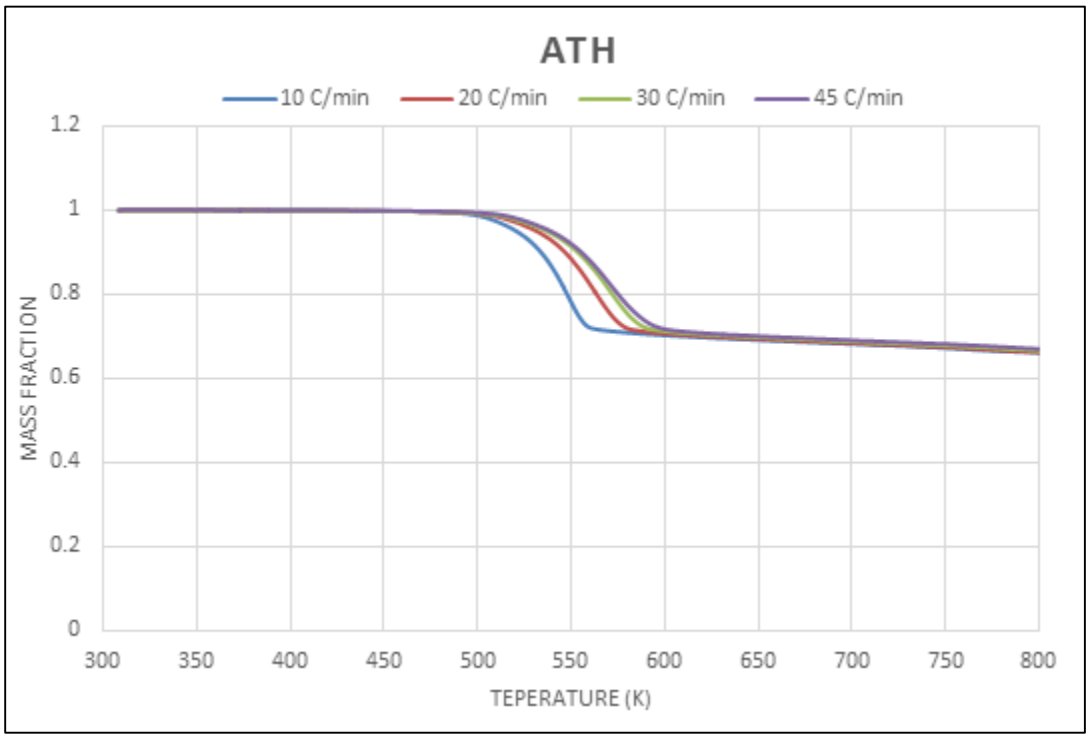

Figure 27: Multiple Heating Rate for ATH TGA Data

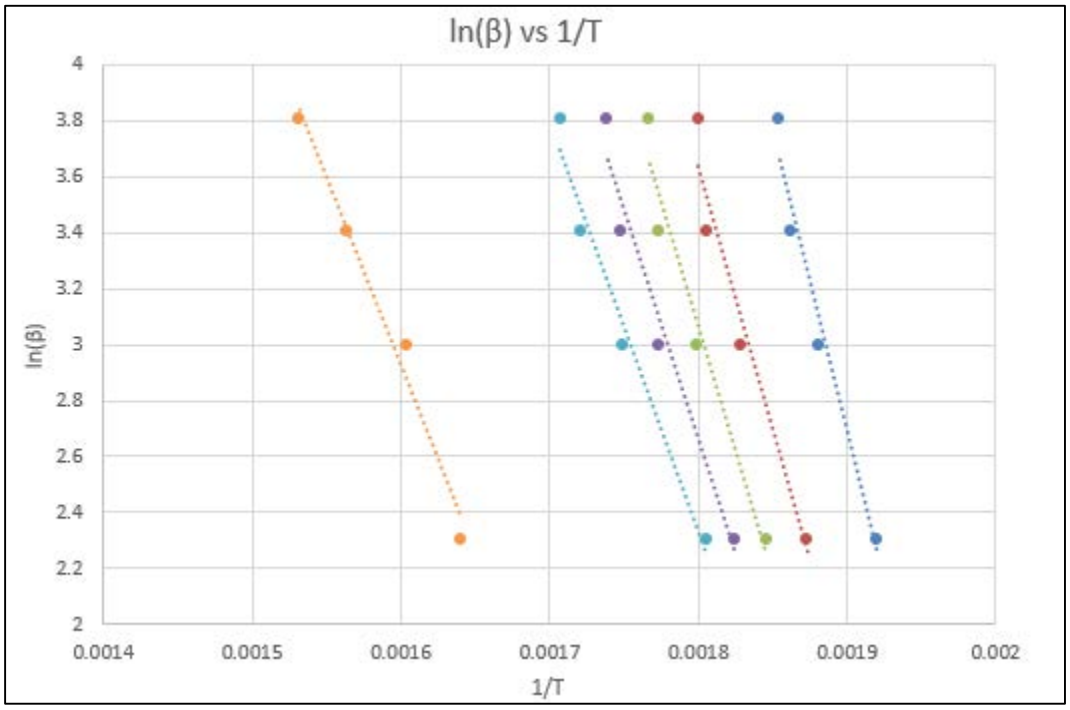

Figure 28: Intermediate Step in Isoconversional Method

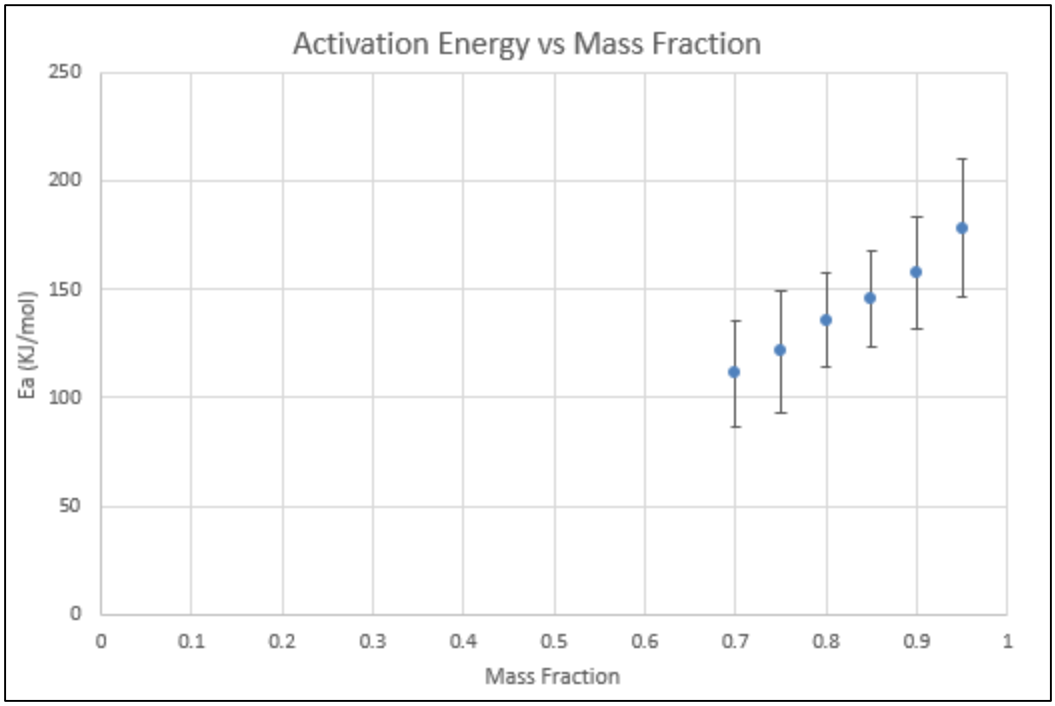

Figure 29: Activation Energy Trend Observed from Various Alpha Values

Multiple Heating Rate – Activation Energy

Table 7: ATH Error and Activation Energy Determination

α	Slope	LINEST	Ea (kJ/mol)	Error
0.95	-21446	3870.10	178.30	32.18
0.9	-18971	3135.07	157.72	26.06
0.85	-17551	2673.68	145.92	22.23
0.8	-16312	2593.48	135.62	21.56
0.75	-14572	3432.48	121.15	28.54
0.7	-13350	2896.88	110.99	24.08

Appendix H: Sand Data

TGA tests were run with Sand samples at four different heating rates, 10 K/min, 20 K/min, 30 K/min, and 45 K/min.

Single Heating Rate Method

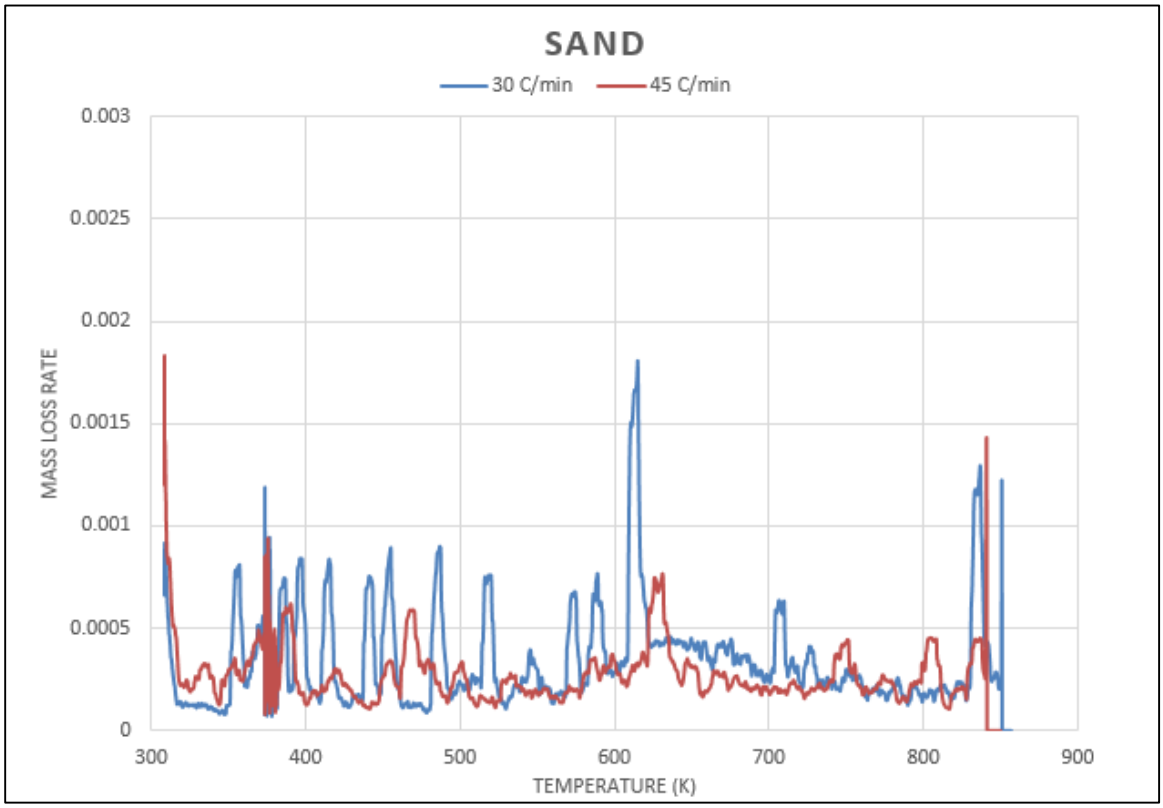

Figure 30: Single Heating Rate Method of ATH at Various Heating Rates

Figure 31 illustrates that sand doesn't have a significant temperature where a large portion of the compound can be seen decomposing. This was what was expected because sand doesn't burn. Only two heating rates were looked at because it was proven that sand wouldn't decompose from them.

Appendix I: Hetron 650 T20 Data

Hetron-ATH (100:0)

TGA tests were run with Hetron-ATH (100:0) samples at four different heating rates, 10 K/min, 20 K/min, 30 K/min, and 45 K/min.

Single Heating Rate Method

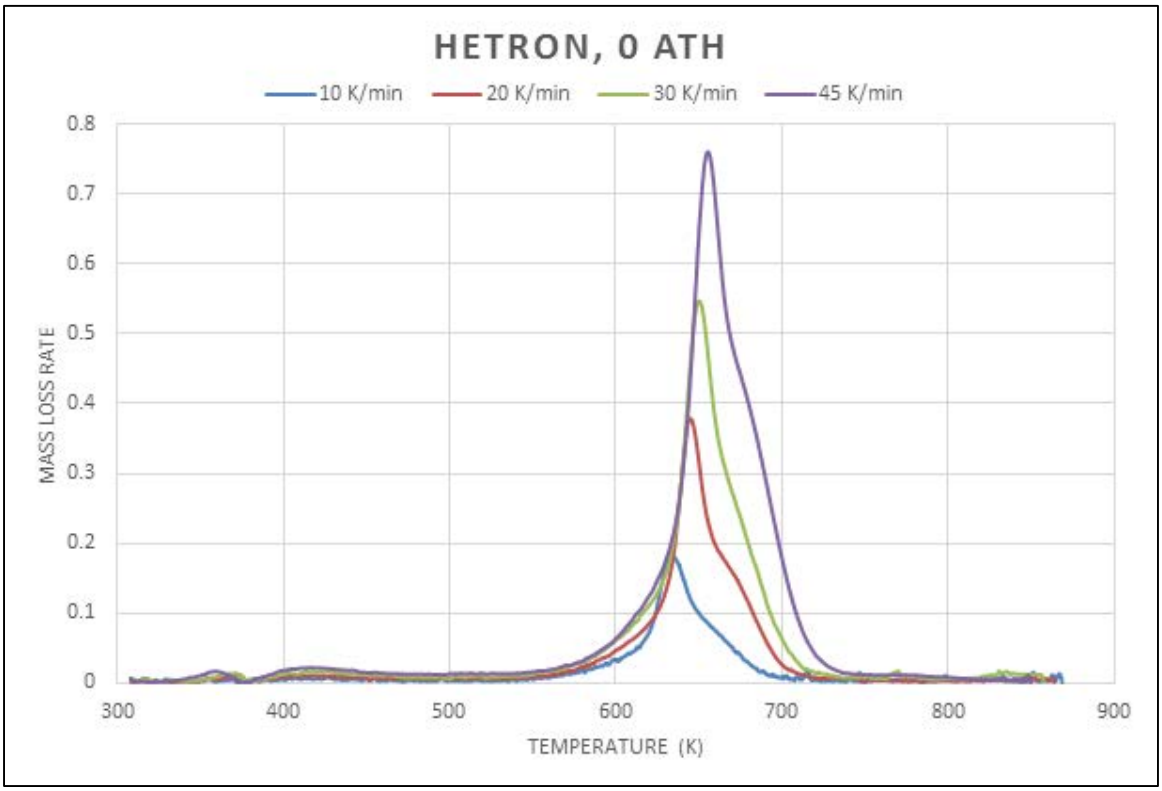

Figure 31: Single Heating Rate Method of Hetron 0 ATH at Various Heating Rates

Single Heating Rate Method – Peak Temperature and Activation Energy

Table 8: Peak Temperature and Activation Energies

Heating Rate (K/min)	Peak Temperature (K)	Activation Energy (E_a – J/mol)	Pre-Exponential Factor (A)
10	633.1718	286236.6	3.52E+23
20	644.7258	296158.7	1.69E+24
30	650.7298	293984.5	9.92E+23
45	655.3896	251246.7	3.35E+20

OFW Isoconversional Method

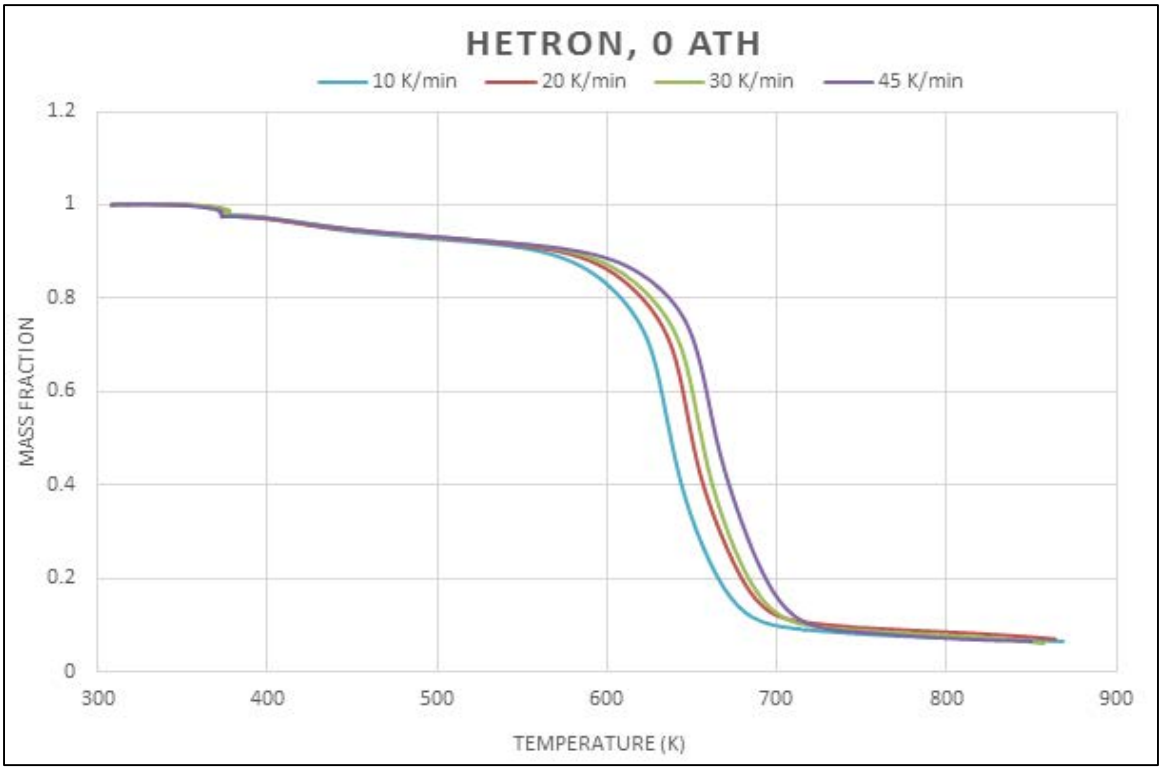

Figure 32: Multiple Heating Rate for Hetron TGA Data

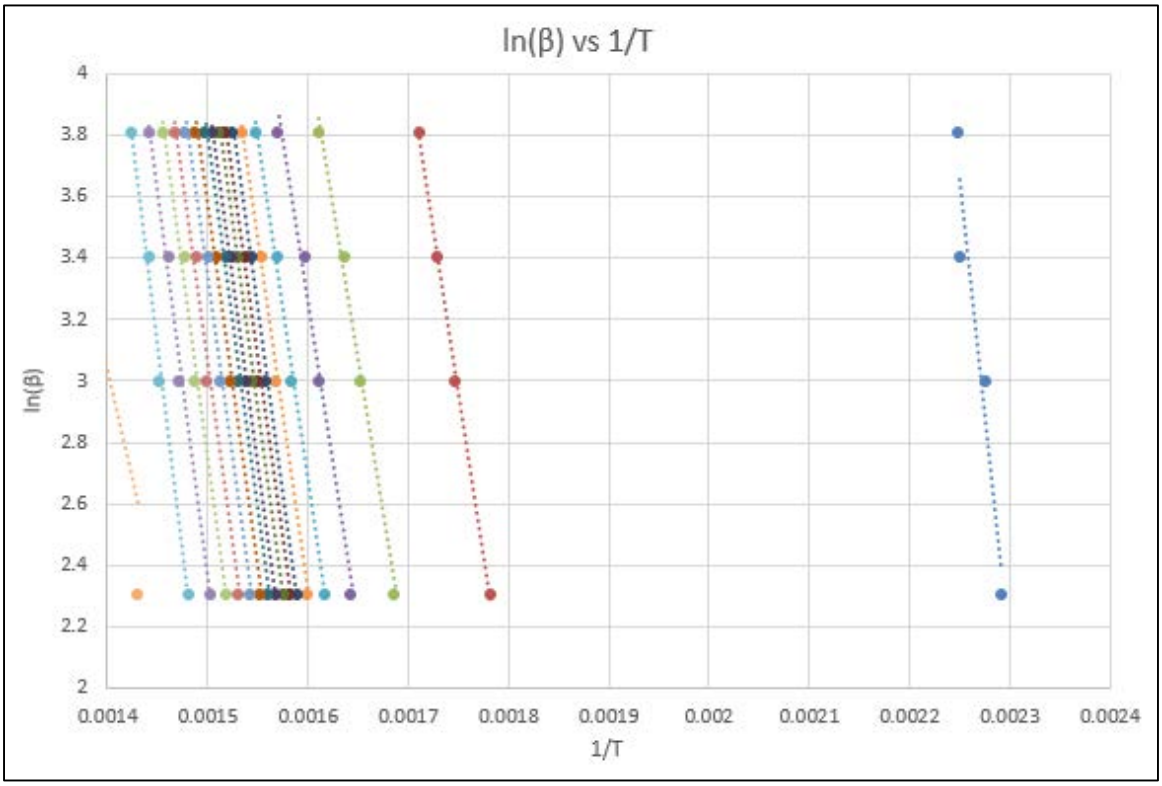

Figure 33: Intermediate Step in Isoconversional Method

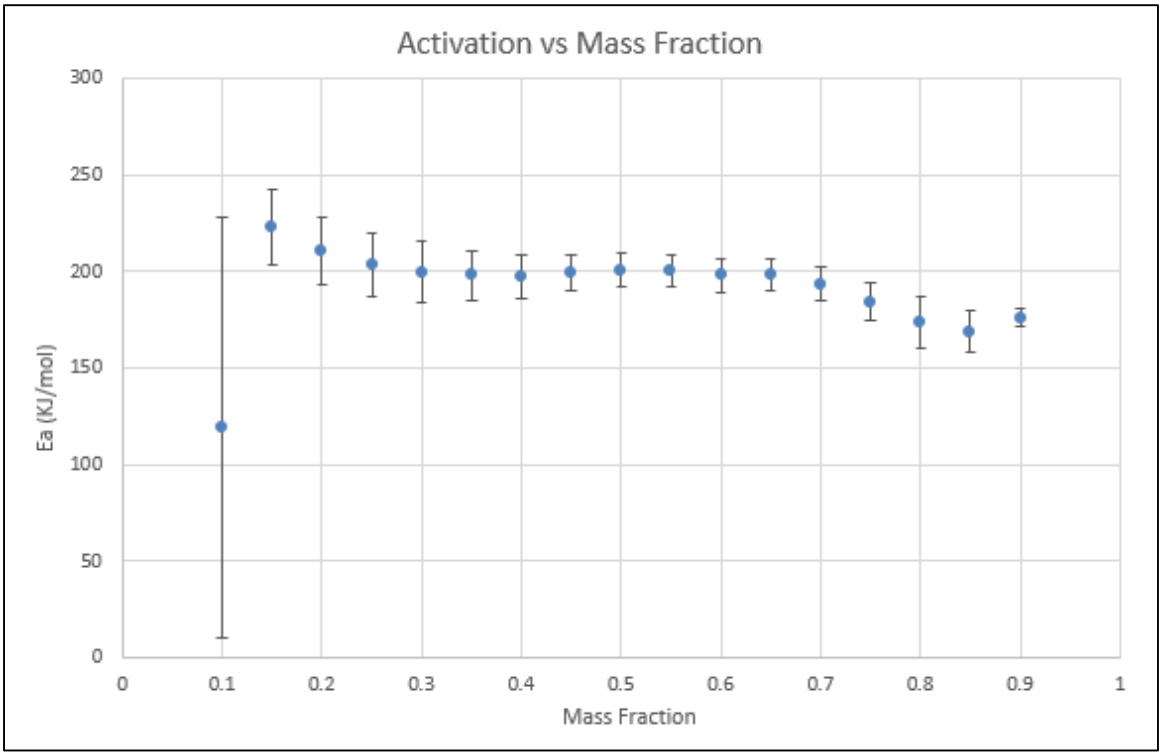

Figure 34: Activation Energy Trend Observed from Various Alpha Values

Multiple Heating Rate – Activation Energy

Table 9: Hetron Error and Activation Energy Determination

α	Slope	LINEST	Ea (kJ/mol)	Error
0.95	21192	6234.723	-176.19028	51.83548
0.9	-21192	591.6598	176.190288	4.91906
0.85	-20324	1338.826	168.973736	11.131
0.8	-20949	1605.727	174.169986	13.35001
0.75	-22160	1171.161	184.23824	9.737031
0.7	-23243	1053.936	193.242302	8.762425
0.65	-23867	968.3769	198.430238	8.051086
0.6	-23801	1037.546	197.881514	8.62616
0.55	-24082	987.0986	200.217748	8.206738
0.5	-24150	1009.424	200.7831	8.392354
0.45	-23999	1106.804	199.527686	9.201971
0.4	-23739	1375.541	197.366046	11.43625
0.35	-23826	1524.398	198.089364	12.67385
0.3	-24007	1896.067	199.594198	15.7639
0.25	-24477	1935.932	203.501778	16.09534
0.2	-25360	2073.306	210.84304	17.23747
0.15	-26809	2378.543	222.890026	19.77521
0.1	-14349	13093.61	119.297586	108.8603

Powder, Chunk, and Drop Analysis

TGA tests were run with Hetron 0 ATH samples at the same heating rate, 30 K/min, for three different morphologies chunk, powder, and drops.

Single Heating Rate Method

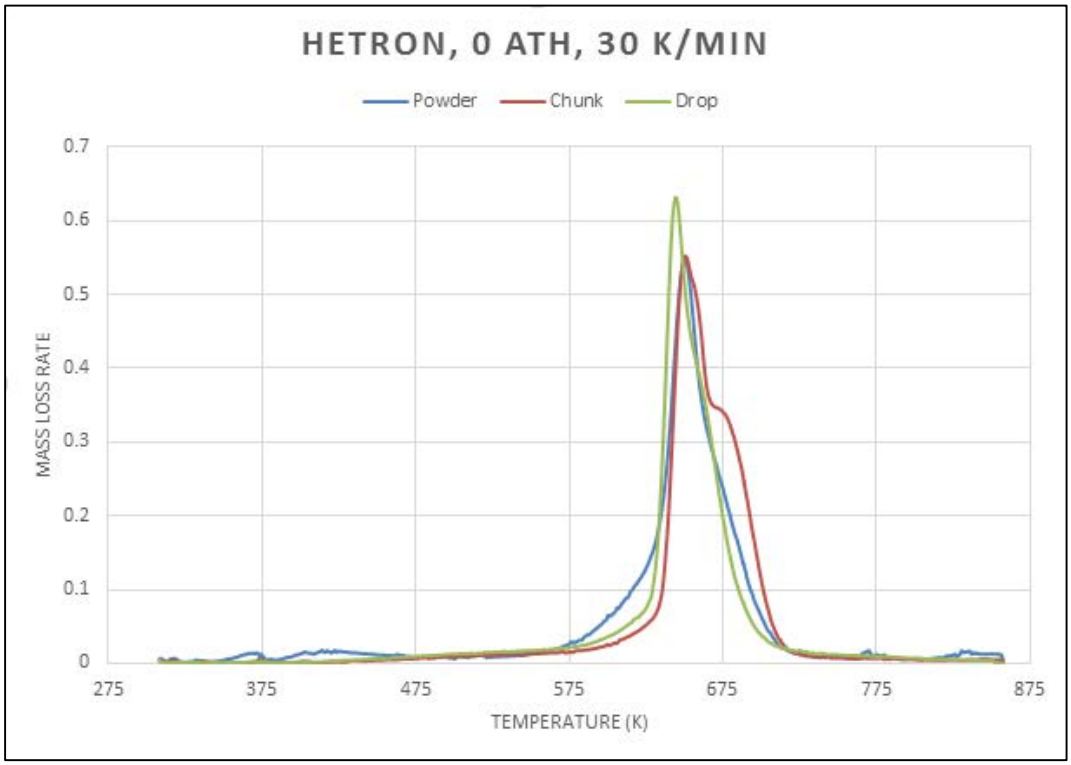

Figure 35: Powder, Chunk, and Drop Samples at Single Heating Rate, 30 K/min

Mass Loss History

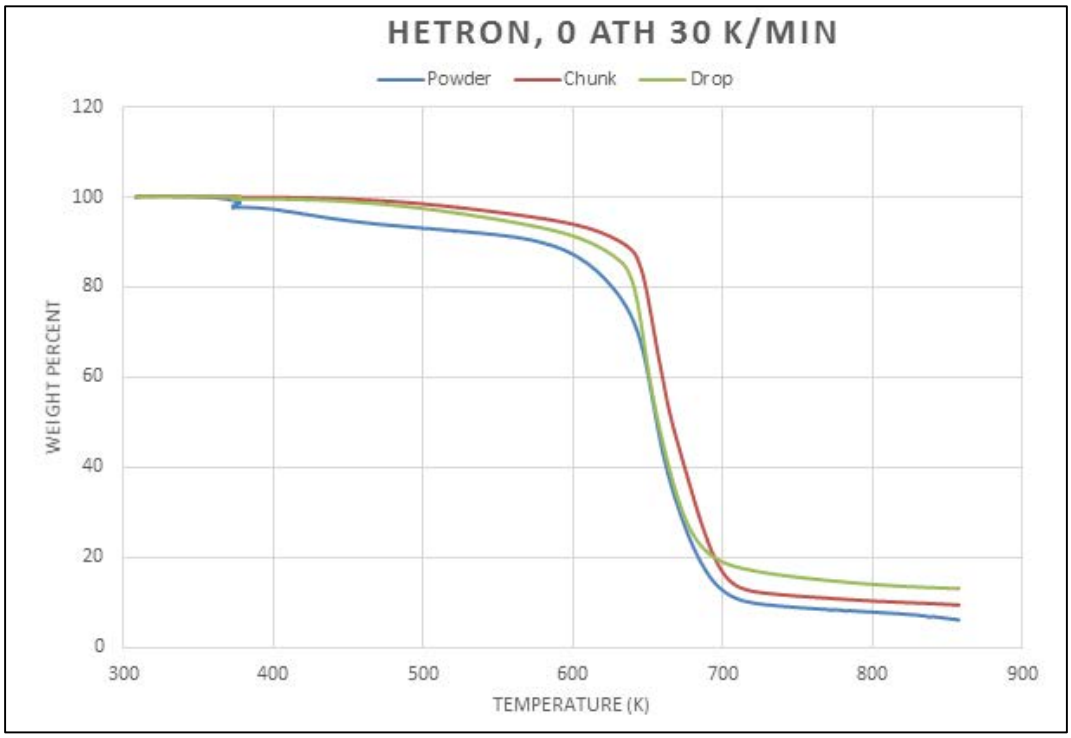

Figure 36: Change in Alpha Value compared to the temperature for various Sample Preps

Hetron-ATH (100:33)

TGA tests were run with Hetron-ATH (100:33)samples at four different heating rates, 10 K/min, 20 K/min, 30 K/min, and 45 K/min.

Single Heating Rate Method

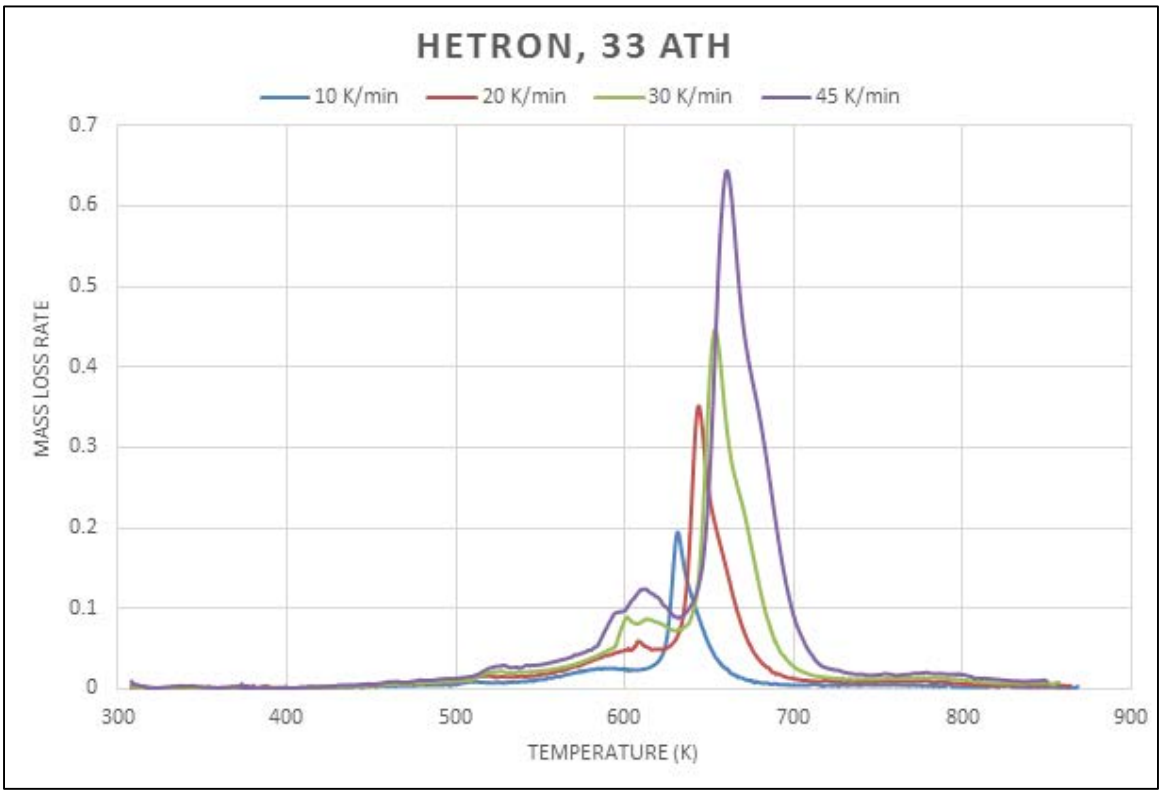

Figure 37: Single Heating Rate Method of Hetron 33 ATH at Various Heating Rates

Single Heating Rate Method – Peak Temperature and Activation Energy

Table 10: Peak Temperature and Activation Energies

Heating Rate (K/min)	Peak Temperature (K)	Activation Energy (E_a – J/mol)	Pre-Exponential Factor (A)
10	631.1395	258374.486	1.89E+21
20	643.2533	235300.178	1.75E+19
30	652.6638	320912.272	1.31E+26
45	659.1853	218238.337	5.34E+17

OFW Isoconversional Method

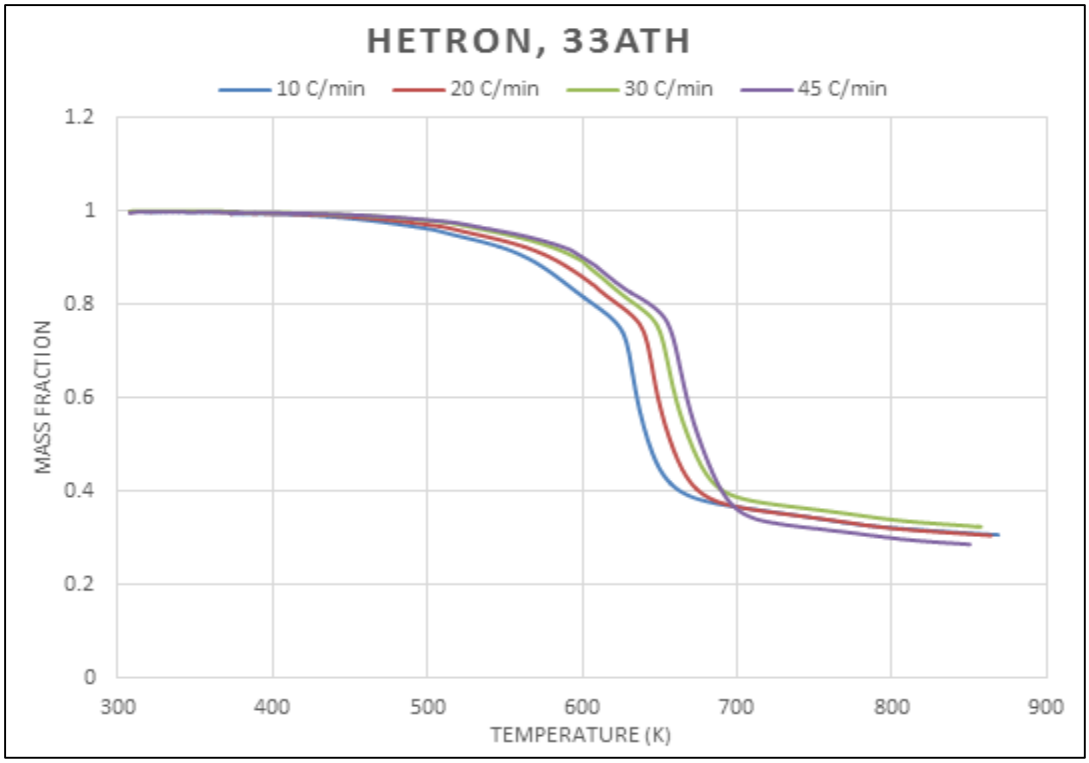

Figure 38: Multiple Heating Rate for Hetron TGA Data

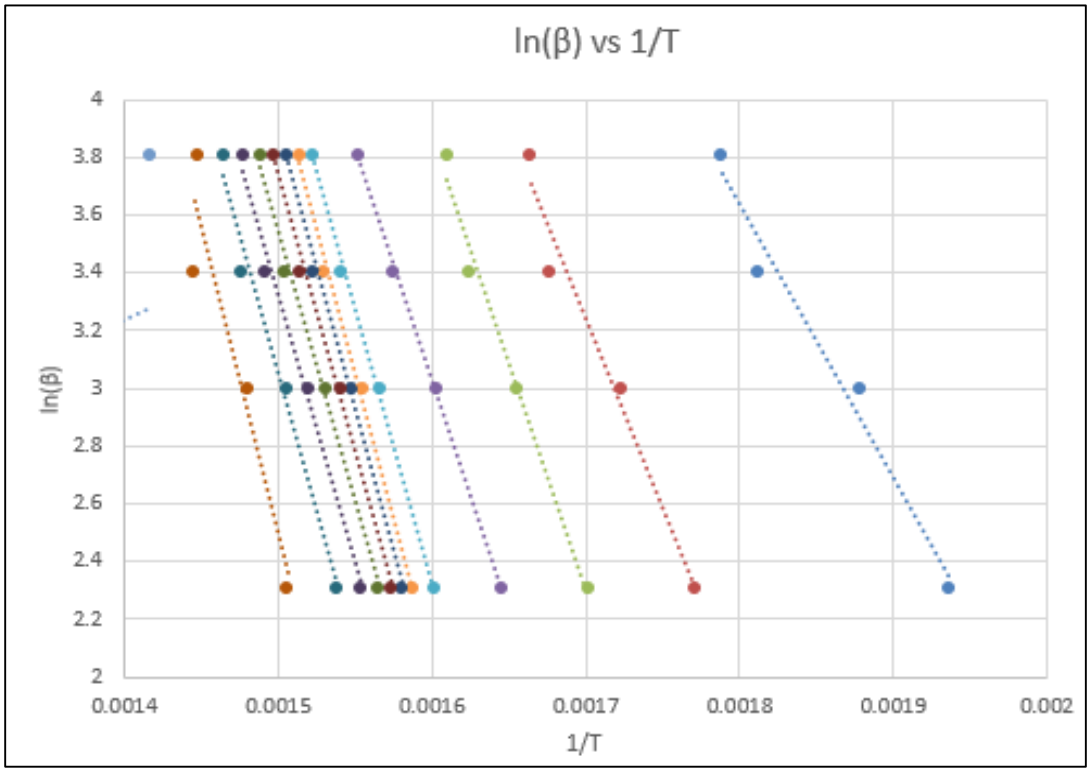

Figure 39: Intermediate Step in Isoconversional Method

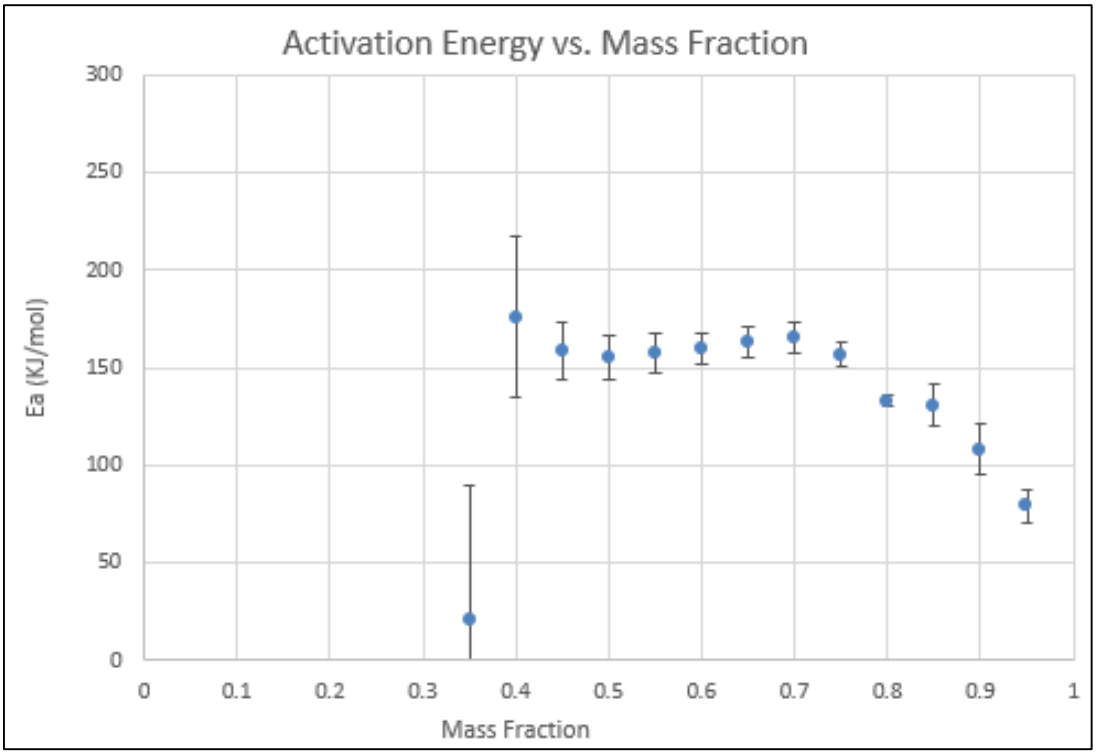

Figure 40: Activation Energy Trend Observed from Various Alpha Values

Multiple Heating Rate – Activation Energy

Table 11: Hetron Error and Activation Energy Determination

α	Slope	LINEST	Ea (kJ/mol)	Error
0.95	-9506.6	1036.53	79.04	8.62
0.9	-13002.0	1562.36	108.10	12.99
0.85	-15718.0	1262.22	130.68	10.49
0.8	-15996.0	345.82	132.99	2.88
0.75	-18851.0	759.36	156.73	6.31
0.7	-19886.0	934.60	165.33	7.77
0.65	-19597.0	975.27	162.93	8.11
0.6	-19182.0	945.19	159.48	7.86
0.55	-18932.0	1168.90	157.40	9.72
0.5	-18642.0	1404.10	154.99	11.67
0.45	-19009.0	1756.80	158.04	14.61
0.4	-21148.0	4913.06	175.82	40.85
0.35	-2465.2	8312.34	20.50	69.11

Powder, Chunk, and Drop Analysis

TGA tests were run with Hetron 33 ATH samples at the same heating rates, 30 K/min, for three different morphologies chunk, powder, and drops.

Single Heating Rate Method

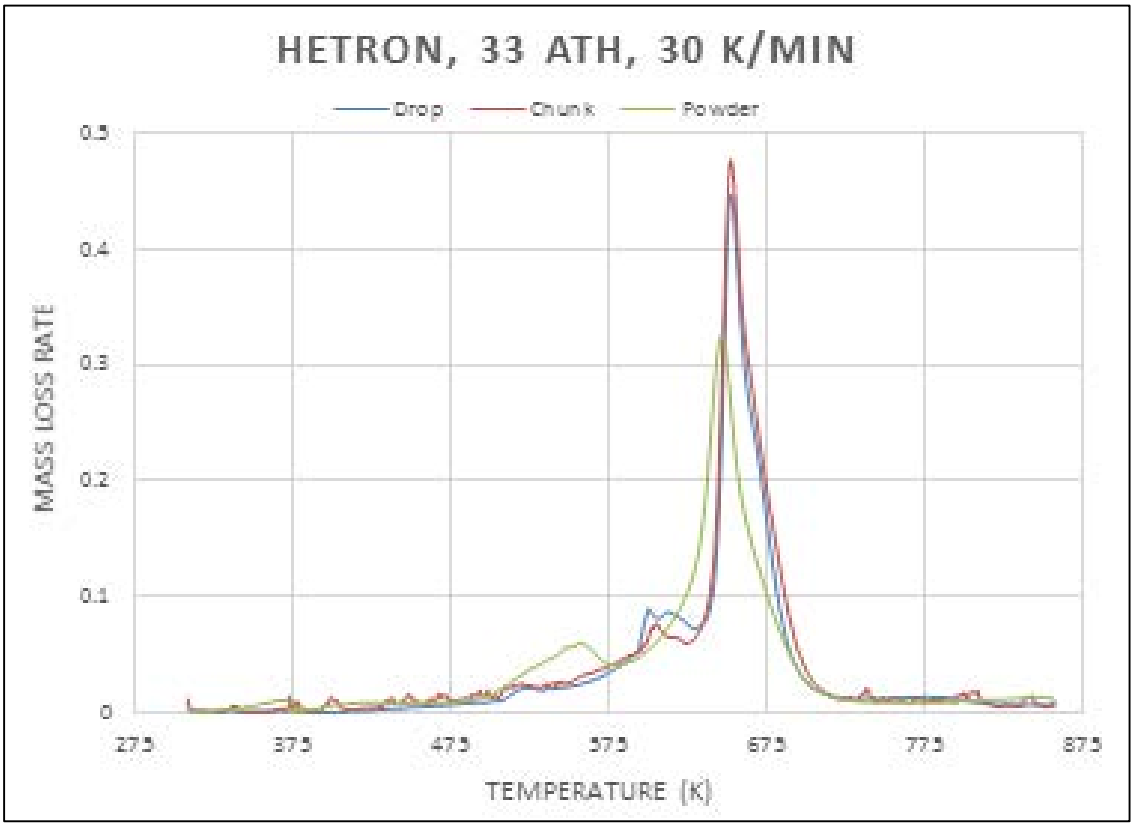

Figure 41: Powder, Chunk, Drop Samples at Single Heating Rate, 30 K/min

Mass Loss History

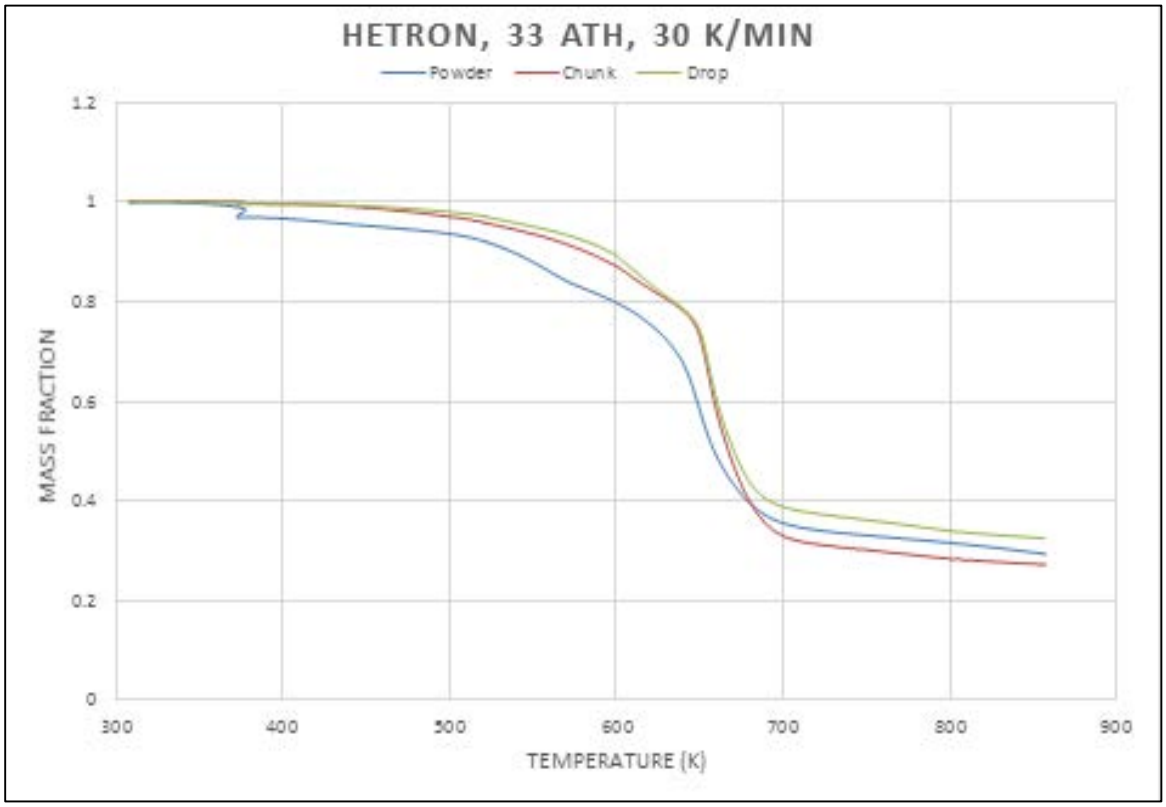

Figure 42: Change in Alpha Value compared to the temperature for various Sample Preps

Hetron-ATH (100:66)

TGA tests were run with Hetron (66 ATH) samples at four different heating rates, 10 K/min, 20 K/min, 30 K/min, and 45 K/min.

Single Heating Rate Method

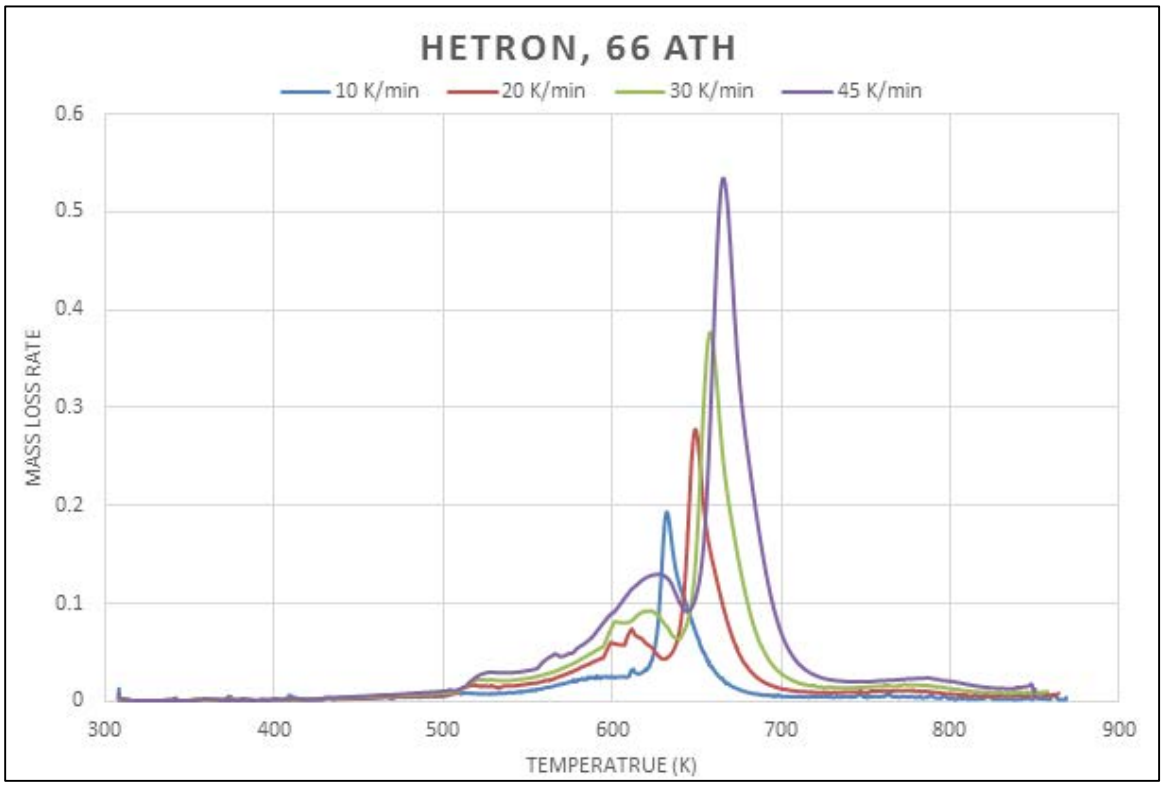

Figure 43: Single Heating Rate Method of Hetron 66 ATH at Various Heating Rates

Single Heating Rate Method – Peak Temperature and Activation Energy

Table 12: Peak Temperature and Activation Energies

Heating Rate (K/min)	Peak Temperature (K)	Activation Energy (E_a – J/mol)	Pre-Exponential Factor (A)
10	632.3076	252356.953	5.33E+20
20	649.2413	188344.022	1.53E+15
30	657.9582	173026.589	7.86E+13
45	665.8345	163618.888	1.37E+13

OFW Isoconversional Method

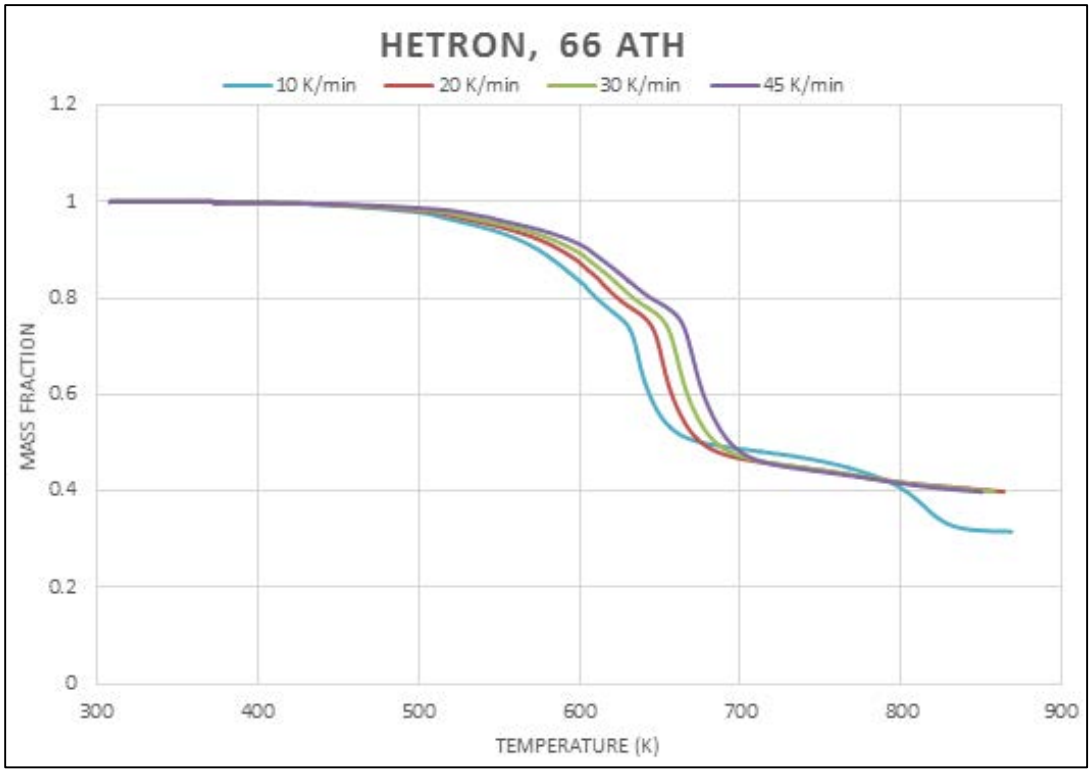

Figure 44: Multiple Heating Rate for Hetron TGA Data

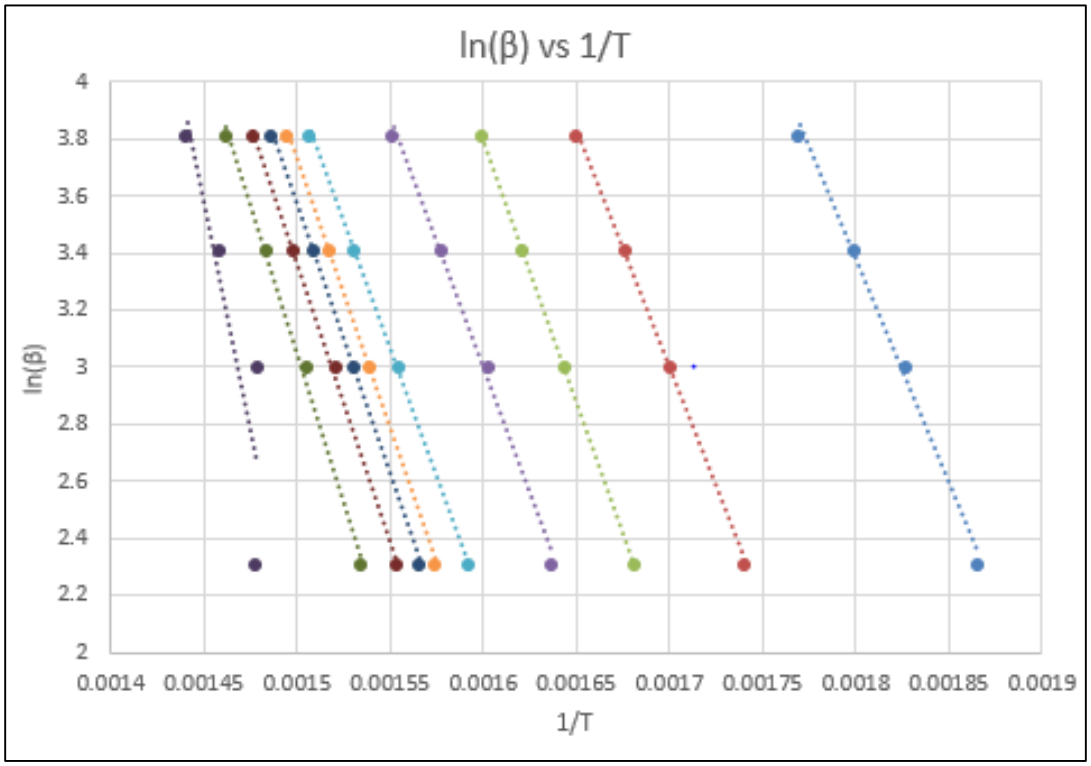

Figure 45: Intermediate Step in Isoconversional Method

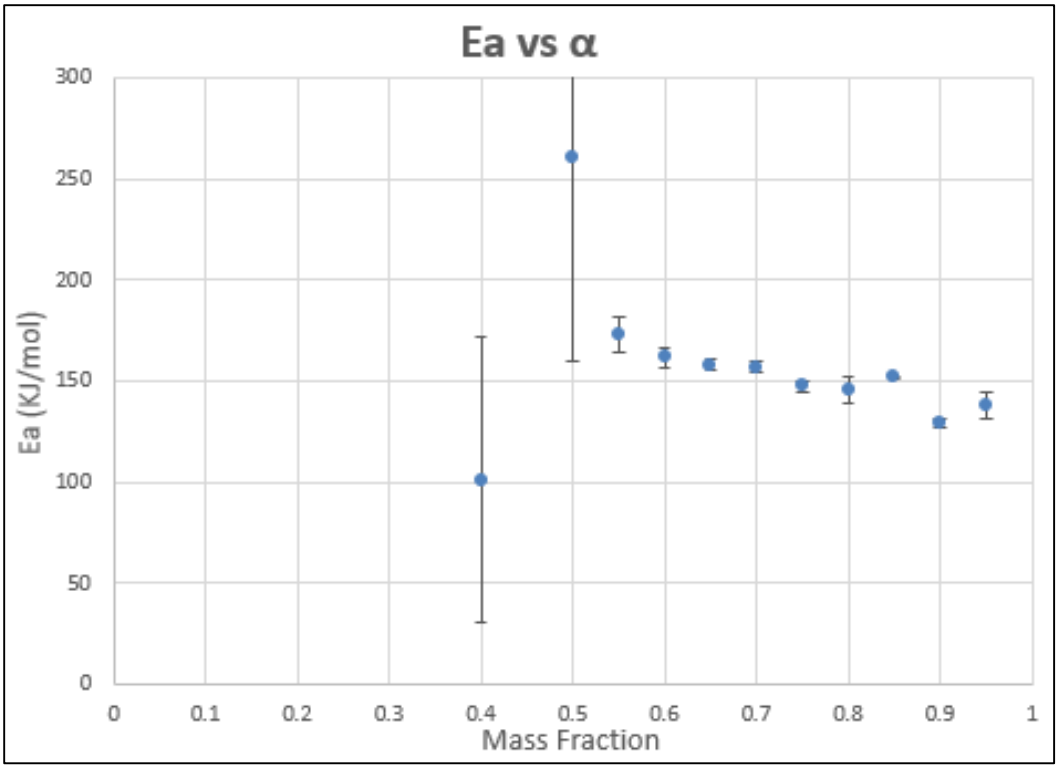

Figure 46: Activation Energy Trend Observed from Various Alpha Values

Multiple Heating Rate – Activation Energy

Table 13: Hetron Error and Activation Energy Determination

α	Slope	LINEST	Ea (kJ/mol)	Error
0.95	-16624	784.58	138.21	6.52
0.9	-15559	227.94	129.36	1.90
0.85	-18261	62.49	151.82	0.52
0.8	-17524	782.76	145.69	6.51
0.75	-17745	331.60	147.53	2.76
0.7	-18893	331.45	157.08	2.76
0.65	-19006	324.27	158.02	2.70
0.6	-19465	591.98	161.83	4.92
0.55	-20843	1035.40	173.29	8.61
0.5	-31353	12185.48	260.67	101.31
0.45	20139	6327.74	-167.44	52.61
0.4	-12175	8501.27	101.22	70.68

Powder, Chunk, and Drop Analysis

TGA tests were run with Hetron 66 ATH samples at the same heating rates, 30 K/min, for three different morphologies chunk, powder, and drops.

Single Heating Rate Method

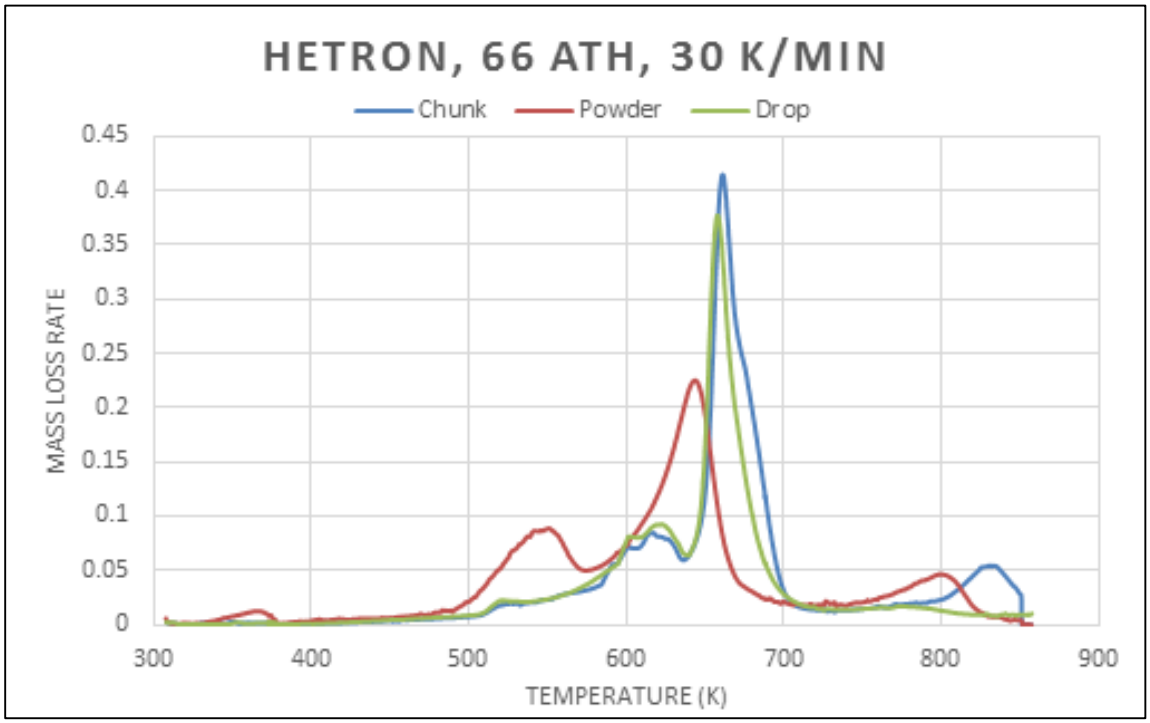

Figure 47: Powder, Chunk, and Drop Samples at Single Heating Rate, 30 K/min

Mass Loss History

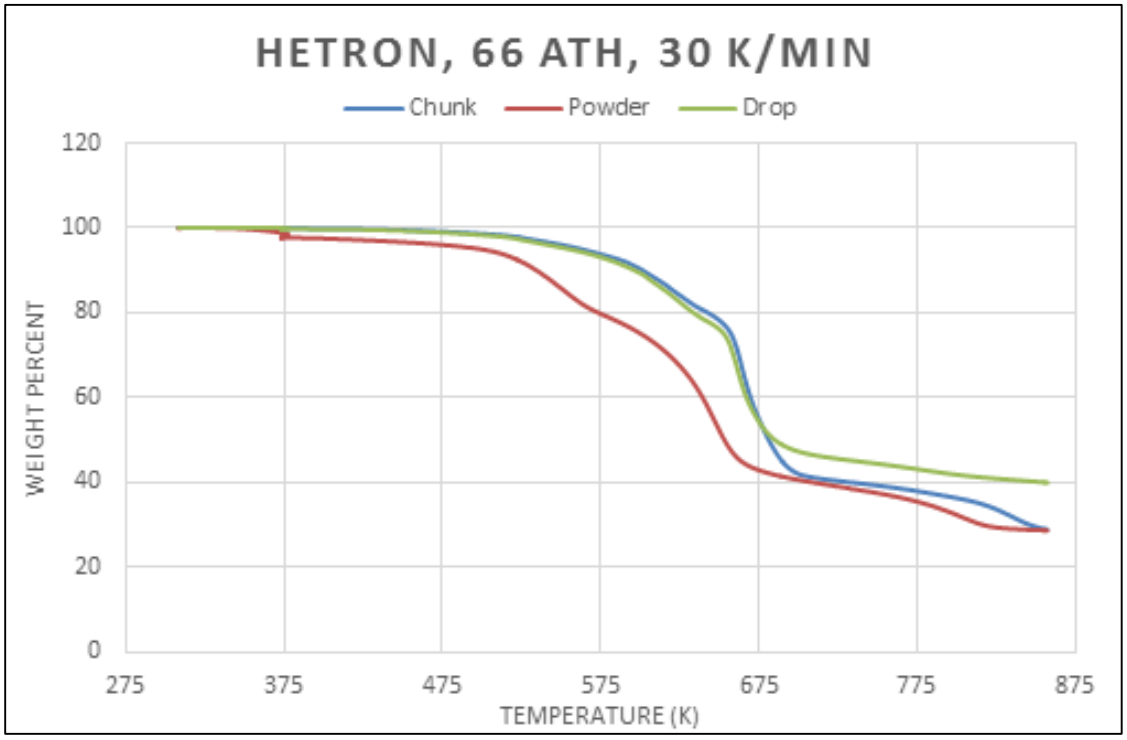

Figure 48: Change in Alpha Value compared to the temperature for various Sample Preps

Hetron-ATH (100:100)

TGA tests were run with Hetron-ATH (100:100) samples at four different heating rates, 10 K/min, 20 K/min, 30 K/min, and 45 K/min.

Single Heating Rate Method

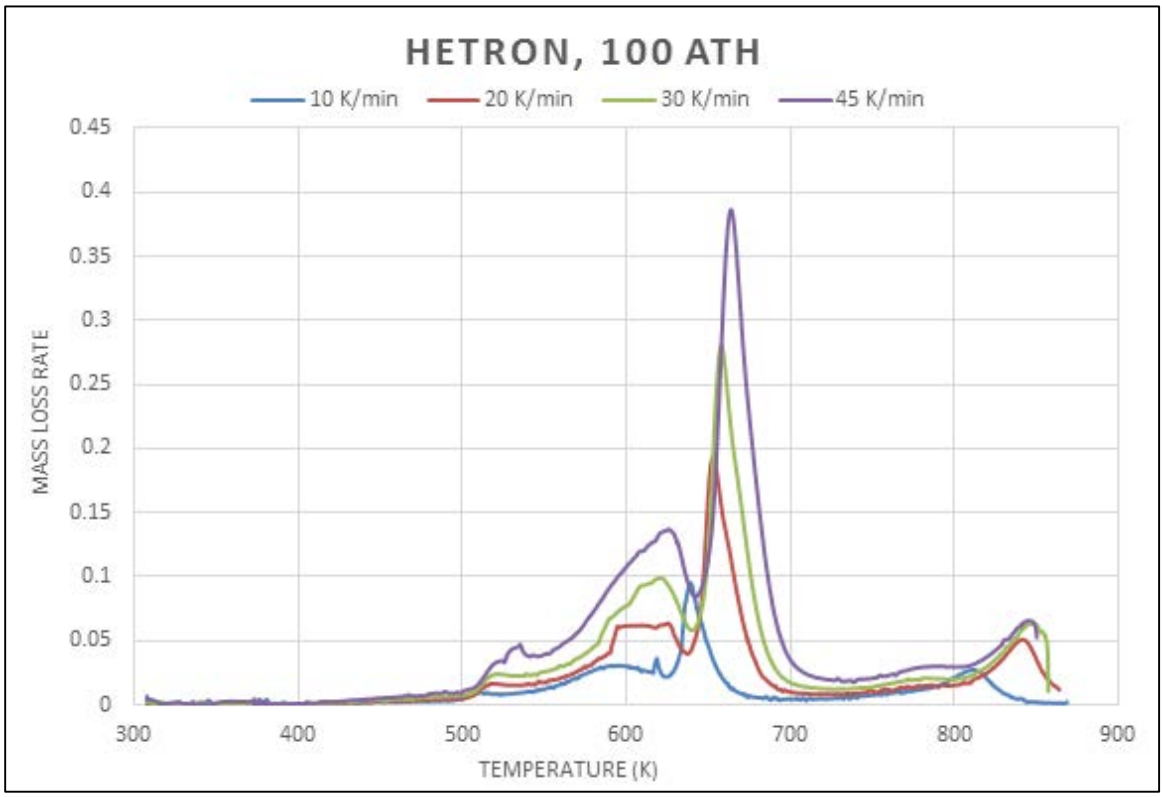

Figure 49: Single Heating Rate Method of Hetron 100 ATH at Various Heating Rates

Single Heating Rate Method – Peak Temperature and Activation Energy

Table 14: Peak Temperature and Activation Energies

Heating Rate (K/min)	Peak Temperature (K)	Activation Energy (E_a – J/mol)	Pre-Exponential Factor (A)
10	638.7558	126817.543	8771164675
20	652.3292	130865.279	2.23E+10
30	657.8349	127280.178	1.36E+10
45	663.0157	119390.387	3741982075

OFW Isoconversional Method

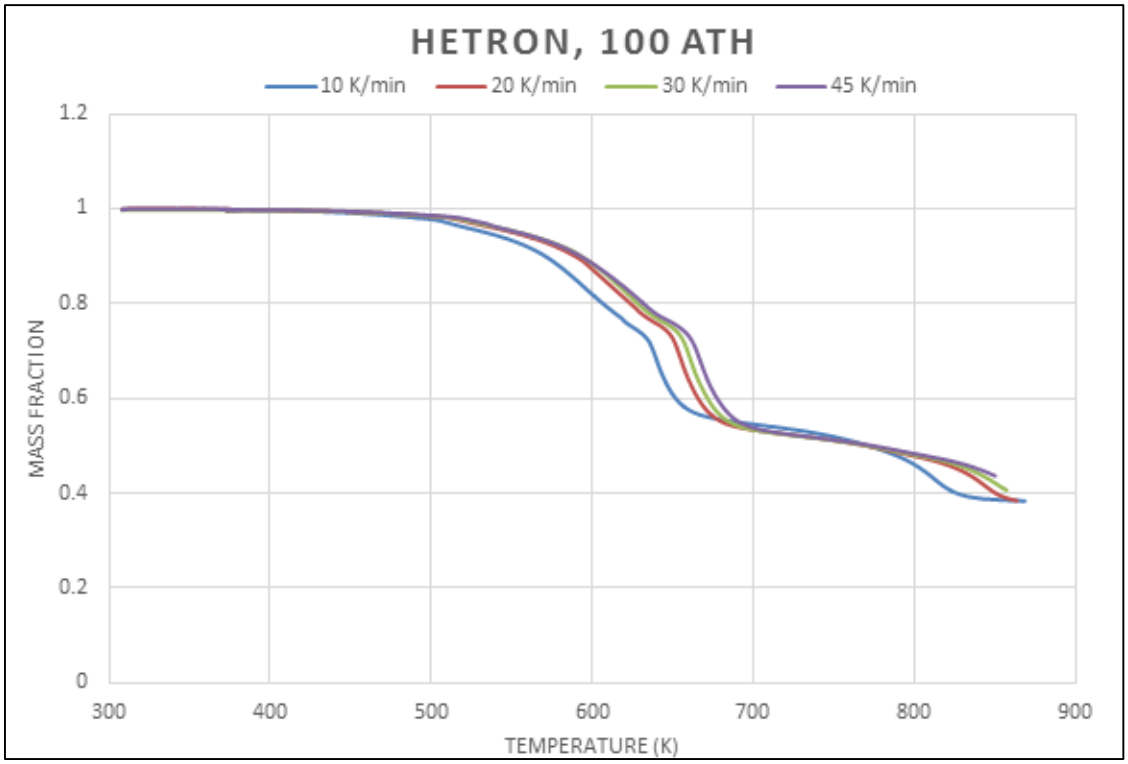

Figure 50: Multiple Heating Rate for Hetron TGA Data

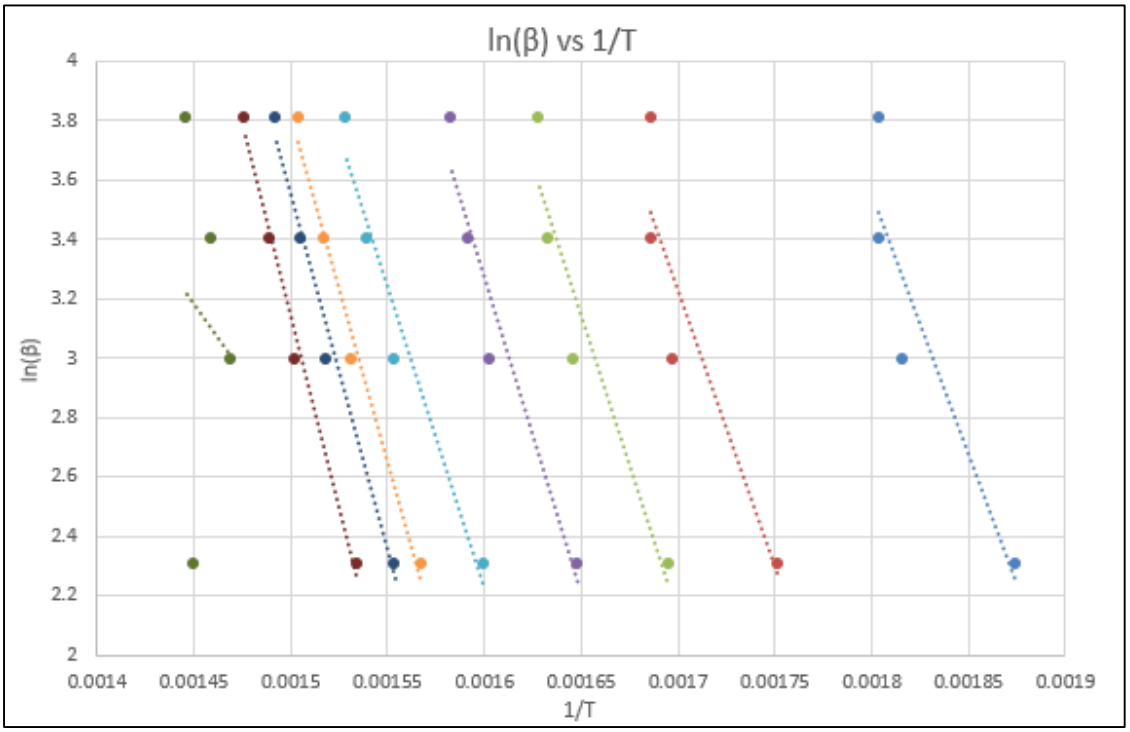

Figure 51: Intermediate Step in Isoconversional Method

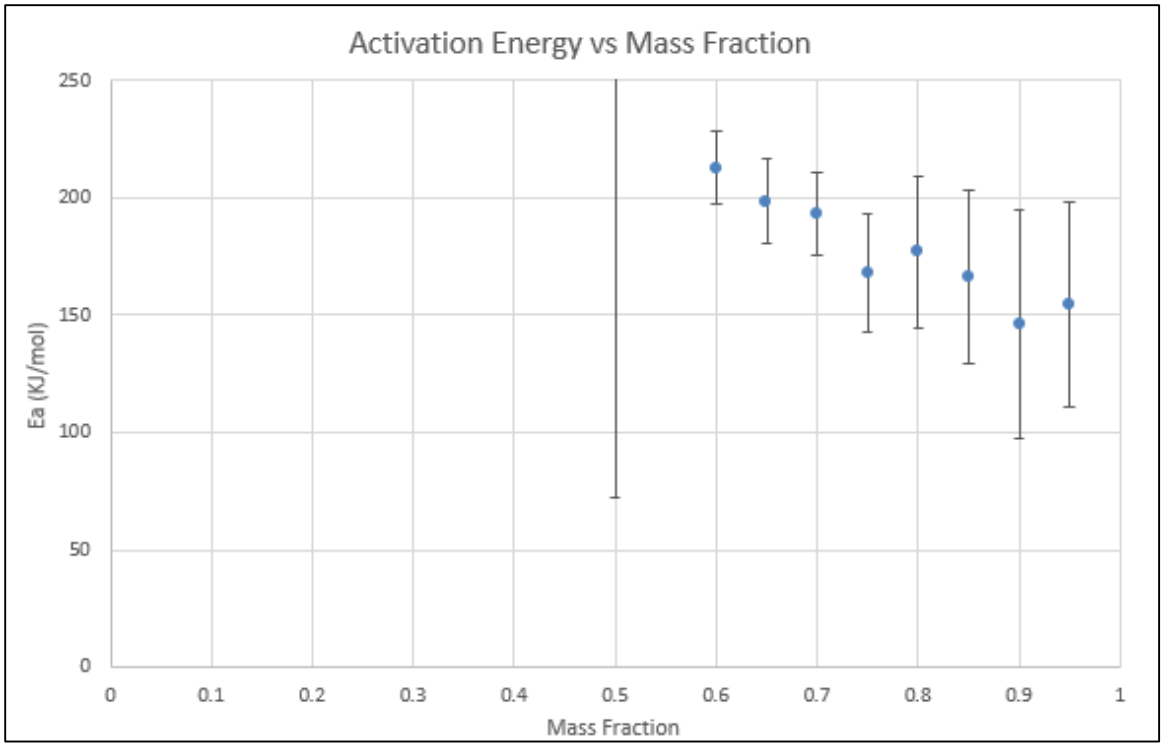

Figure 52: Activation Energy Trend Observed from Various Alpha Values

Multiple Heating Rate – Activation Energy

Table 15: Hetron Error and Activation Energy Determination

α	Slope	LINEST	Ea (kJ/mol)	Error
0.95	-18576	5251.02	154.44	43.66
0.9	-17597	5847.94	146.30	48.62
0.85	-20005	4437.57	166.32	36.89
0.8	-21291	3888.45	177.01	32.33
0.75	-20192	3011.91	167.88	25.04
0.7	-23228	2123.88	193.12	17.66
0.65	-23885	2170.93	198.58	18.05
0.6	-25601	1902.87	212.85	15.82
0.55	-80905	44158.51	672.64	367.13
0.5	-125168	116483.14	1040.65	968.44

Powder, Chunk, and Drop Analysis

TGA tests were run with Hetron 100 ATH samples at the same heating rates, 30 K/min, for three different morphologies chunk, powder, and drops.

Single Heating Rate Method

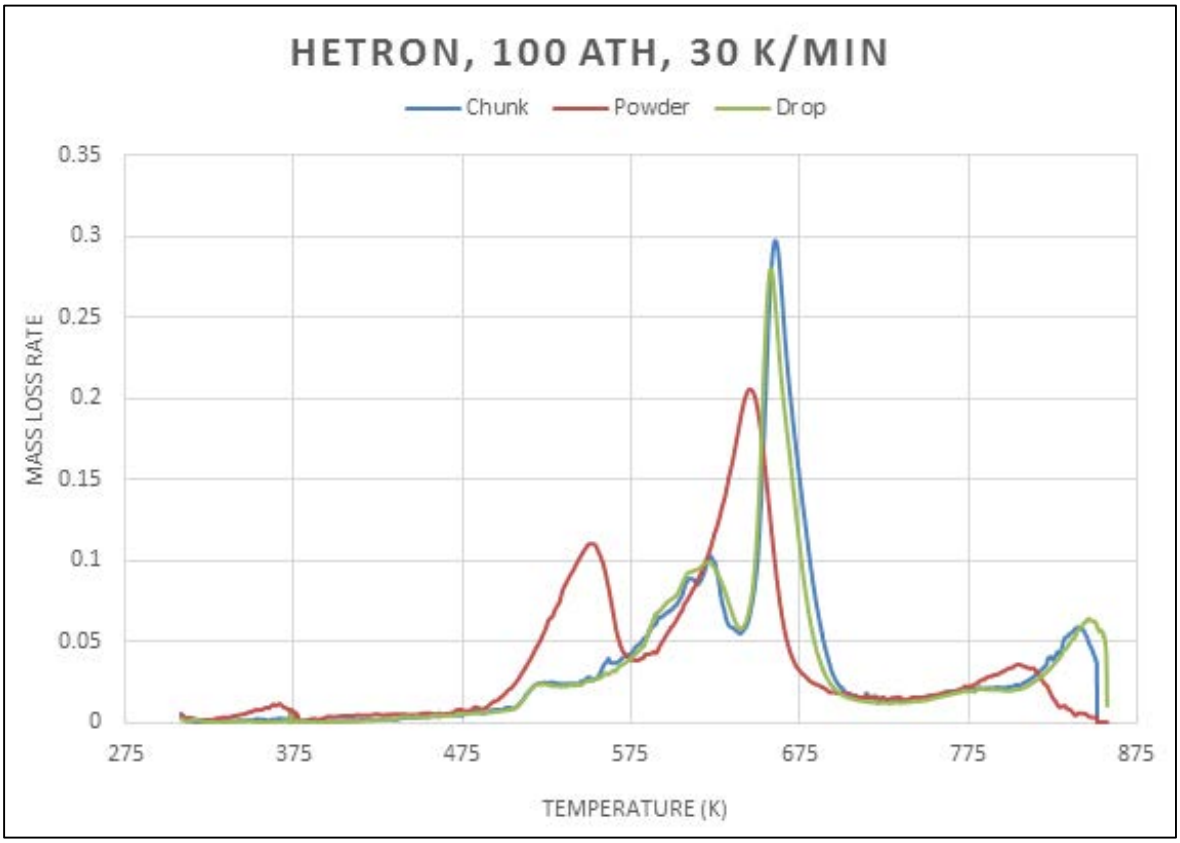

Figure 53: Powder, Chunk, and Drop Samples at Single Heating Rate, 30K/min

Mass Loss History

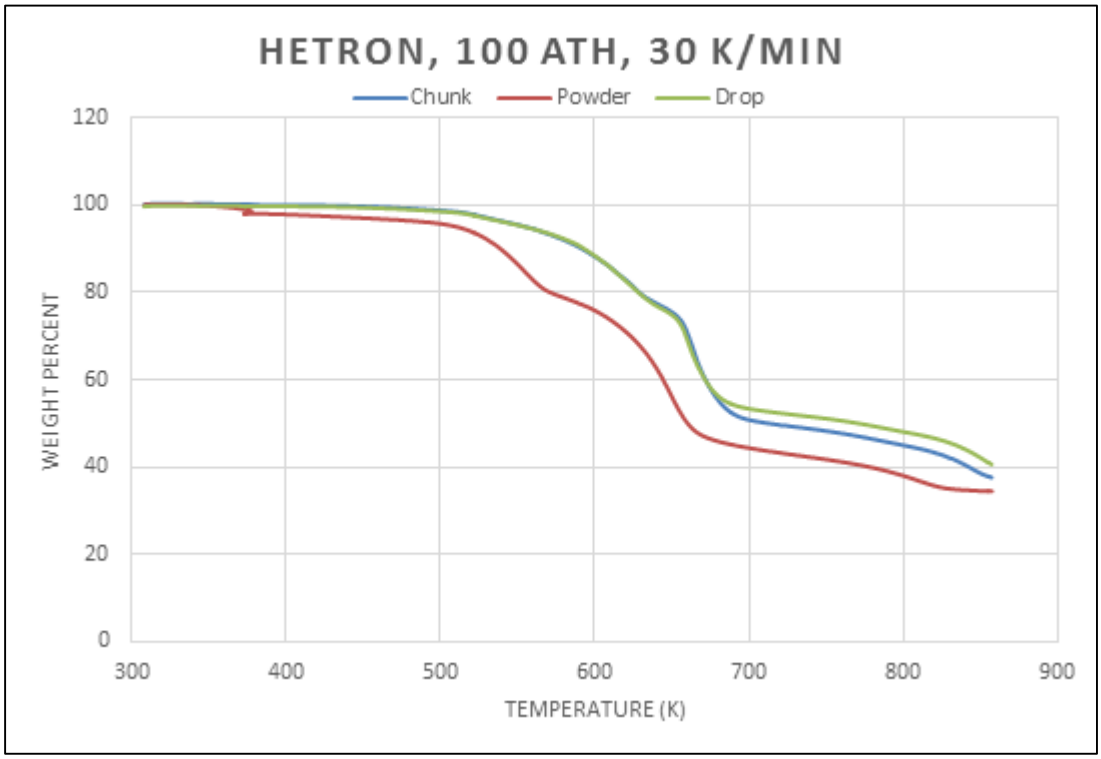

Figure 54: Change in Alpha Value compared to the temperature for various Sample Preps

Hetron-ATH (100:130)

TGA tests were run with Hetron-ATH (100:130) samples at four different heating rates, 10 K/min, 20 K/min, 30 K/min, and 45 K/min.

Single Heating Rate Method

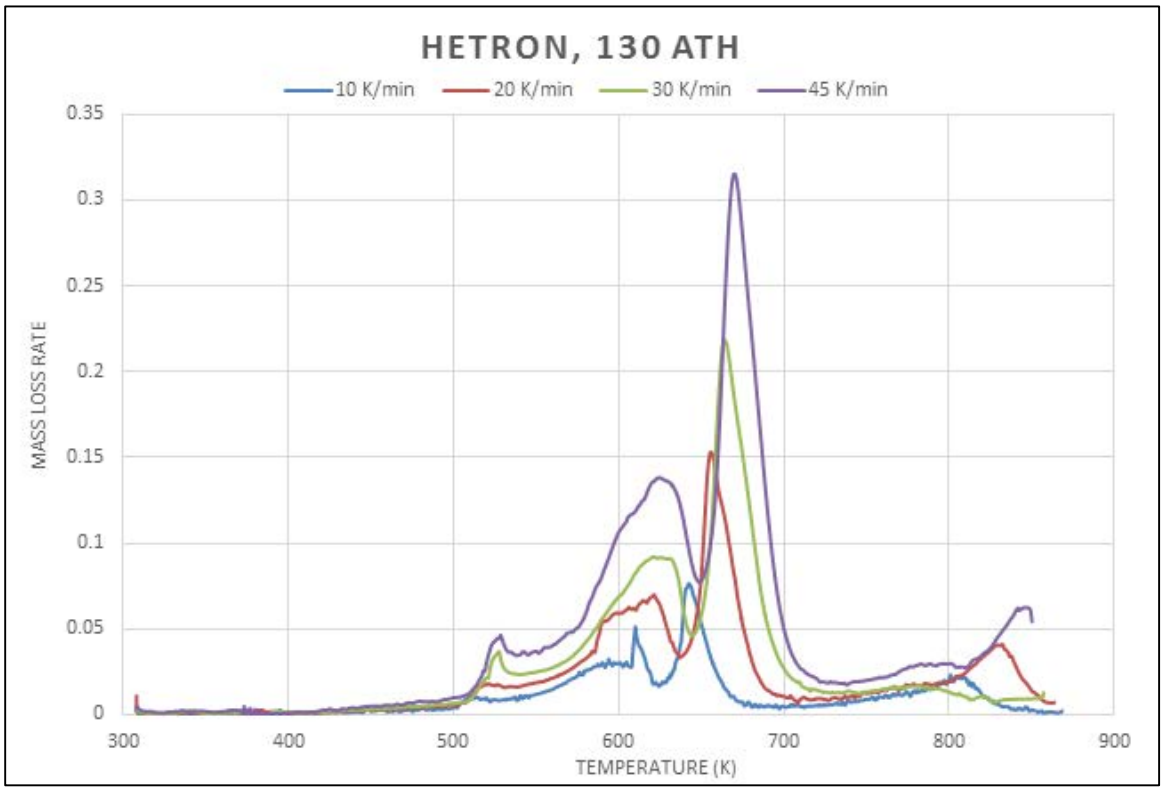

Figure 55: Single Heating Rate Method of Hetron 130 ATH at Various Heating Rates

Single Heating Rate Method – Peak Temperature and Activation Energy

Table 16: Peak Temperature and Activation Energies

Heating Rate (K/min)	Peak Temperature (K)	Activation Energy (E_a – J/mol)	Pre-Exponential Factor (A)
10	642.2466	102968.3	71093653
20	655.1793	105305.7	1.47E+08
30	661.5551	70998.07	2.36E+05
45	668.3796	98819.13	63220016

OFW Isoconversional Method

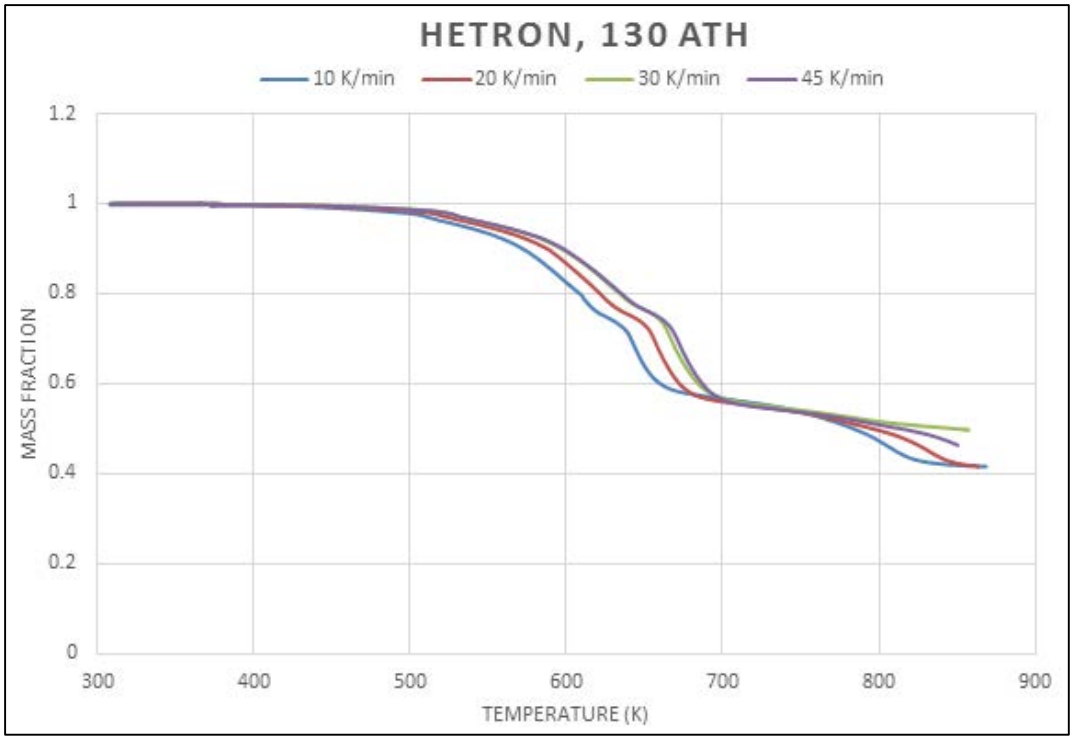

Figure 56: Multiple Heating Rate for Hetron TGA Data

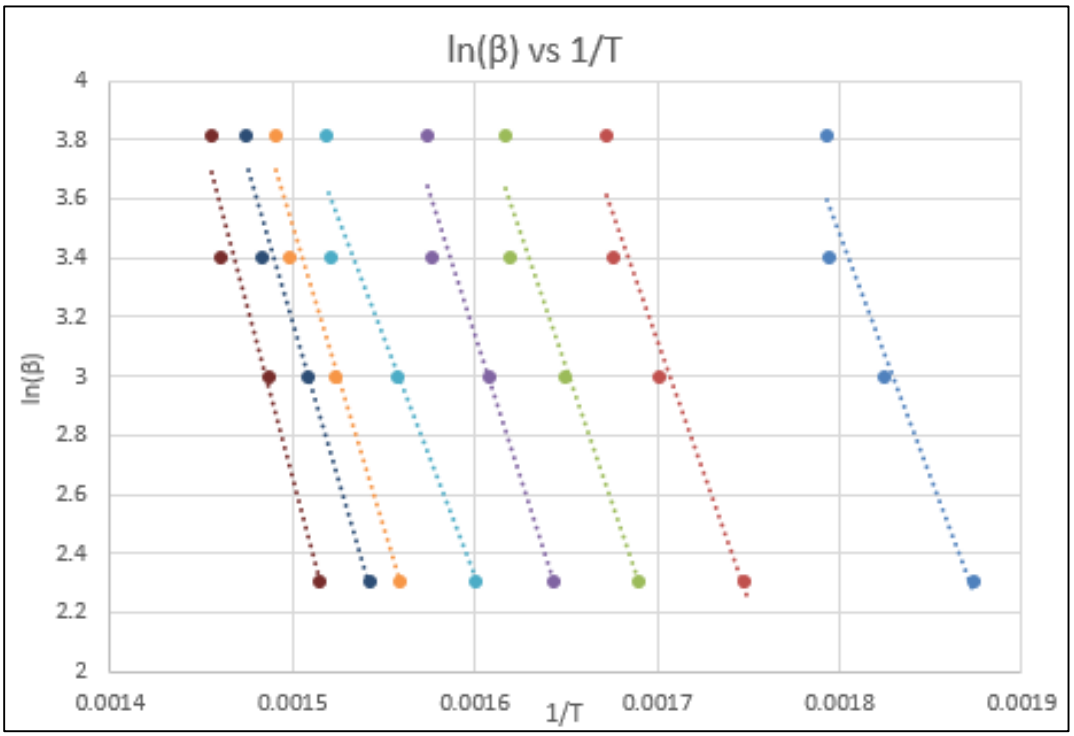

Figure 57: Intermediate Step in Isoconversional Method

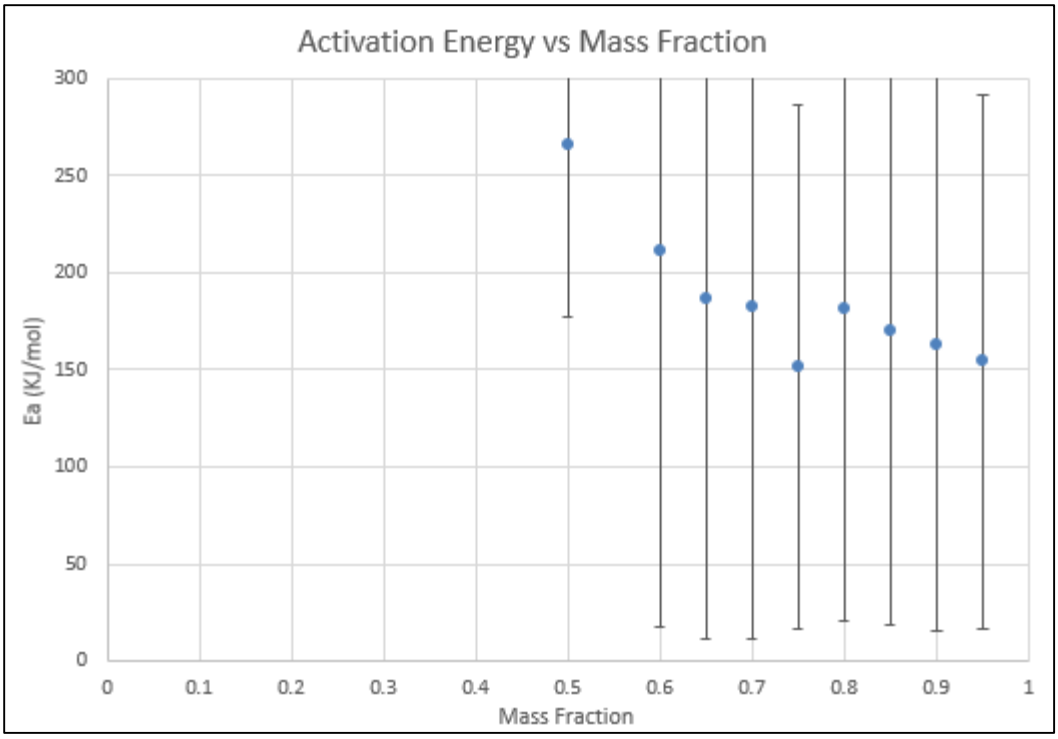

Figure 58: Activation Energy Trend Observed from Various Alpha Values

Multiple Heating Rate – Activation Energy

Table 17: Hetron Error and Activation Energy Determination

α	Slope	LINEST	Ea (kJ/mol)	Error
0.95	-18549	-16551.00	154.22	-137.61
0.9	-19610	-17769.00	163.04	-147.73
0.85	-20408	-18173.00	169.67	-151.09
0.8	-21810	-19354.00	181.33	-160.91
0.75	-18239	-16203.00	151.64	-134.71
0.7	-21925	-20603.00	182.28	-171.29
0.65	-22410	-21000.00	186.32	-174.59
0.6	-25363	-23257.00	210.87	-193.36
0.55	37792	25250.08	-314.20	209.93
0.5	-31962	-10651.00	265.73	-88.55

Powder, Chunk, and Drop Analysis

TGA tests were run with Hetron (130 ATH) samples at the same heating rates, 30 K/min, for three different morphologies chunk, powder, and drops.

Single Heating Rate Method

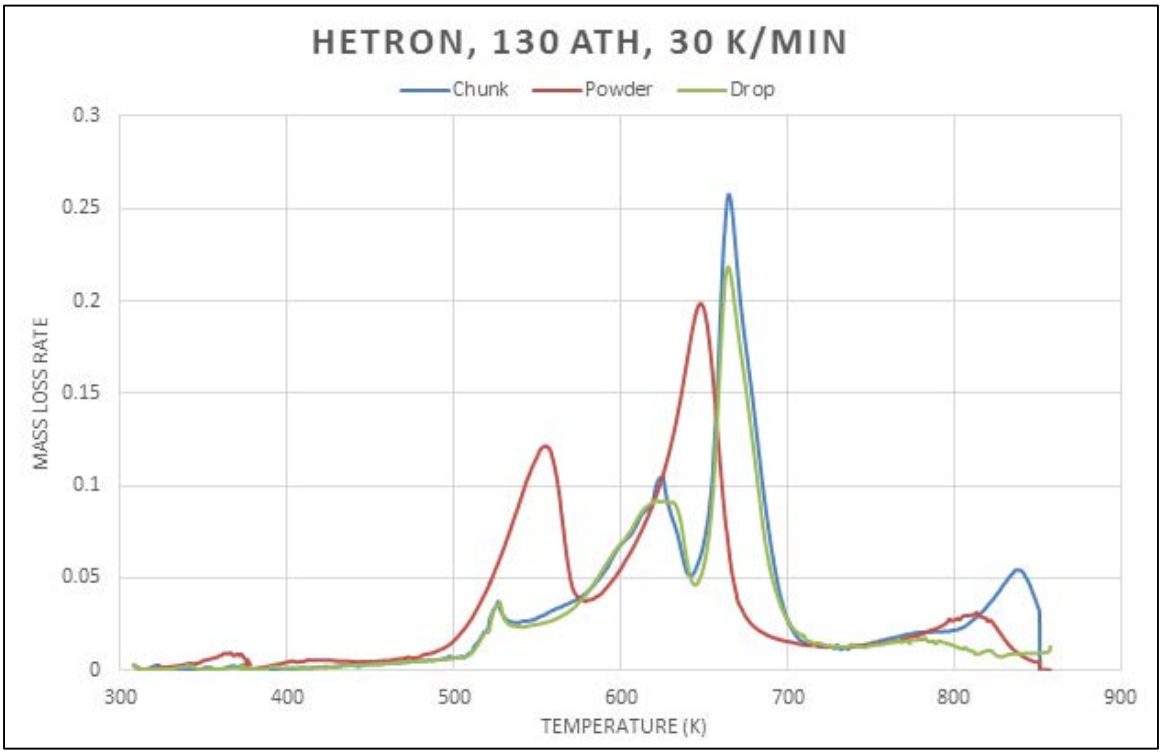

Figure 59: Powder, Chunk, and Drop Samples at Single Heating Rate, 30K/min

Mass Loss History

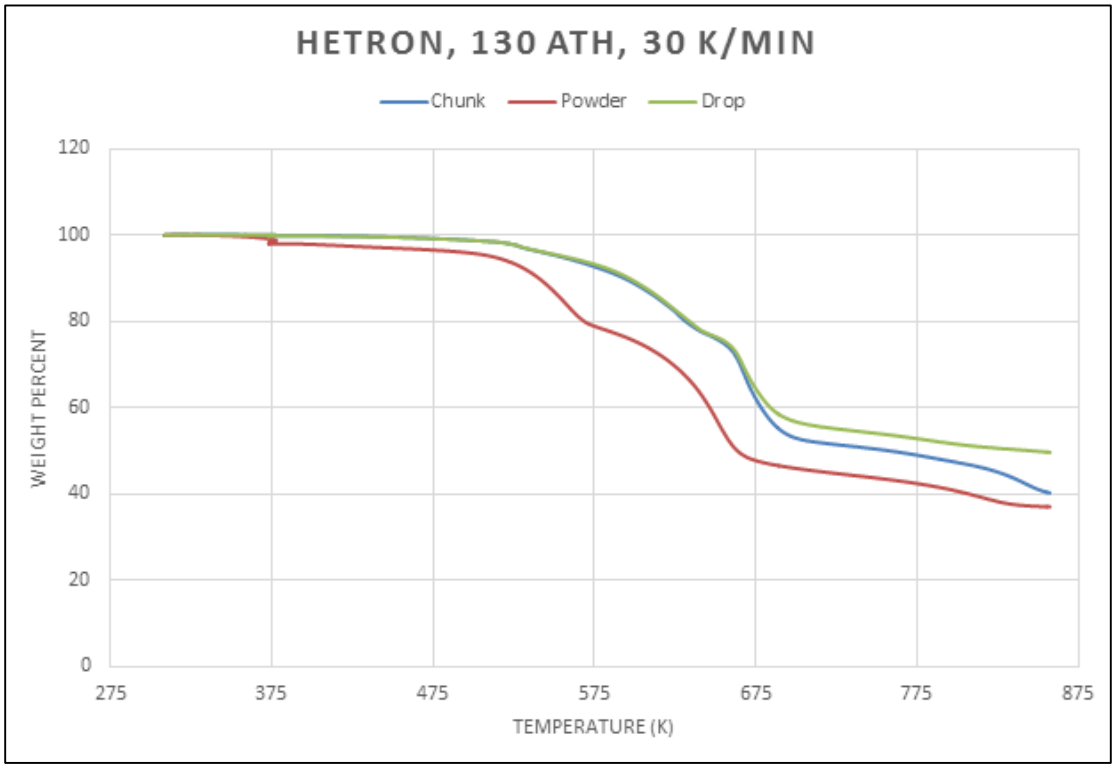

Figure 60: Change in Alpha Value compared to the temperature for various Sample Preps

Hetron Mixtures: Ideal Mixing Model

ATH Model

In this section, the optimized parameters for all ATH samples are displayed in a table. This table is accompanied by the mass fraction and mass loss rate graphs that depict the experimental and modeled decomposition of ATH against temperature.

Heating Rate	Weight-loss Fraction	Activation Energy [kJ/mol]	Pre-exponential Const.	Exponent
10 K/min	0.34	140.1	11.4	0.7
20 K/min	--	--	--	1.115
30 K/min	--	--	--	1.25
45 K/min	--	--	--	1.5

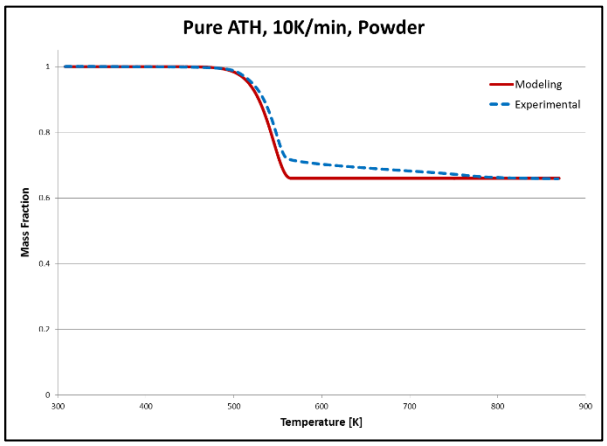

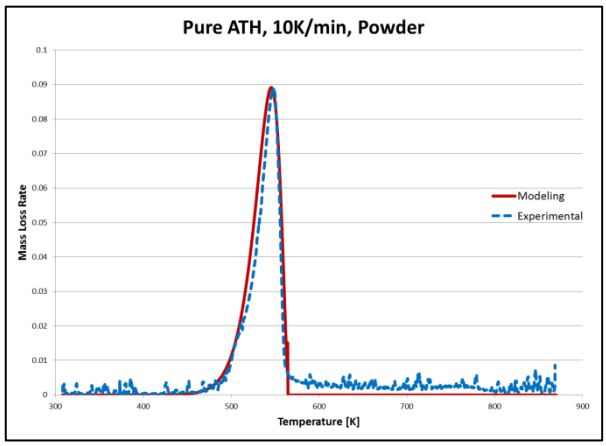

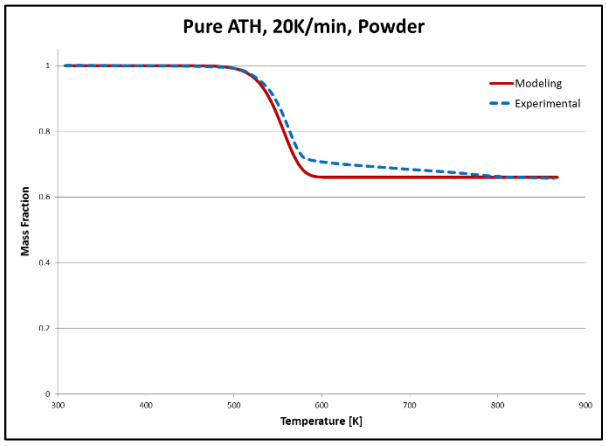

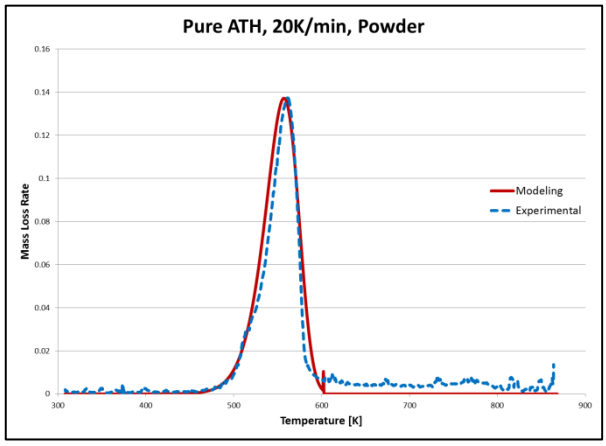

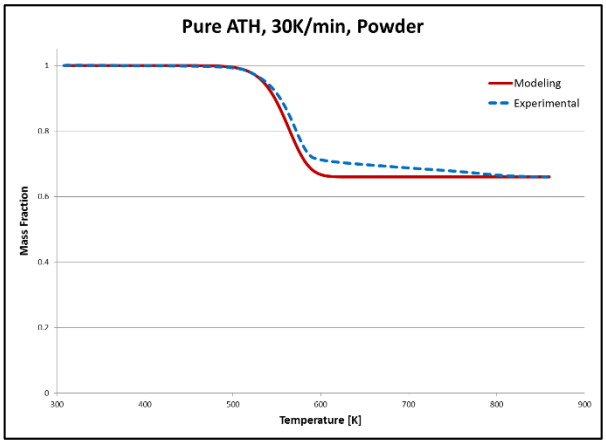

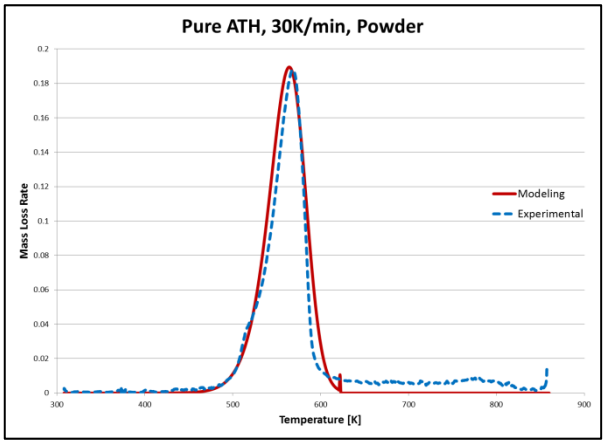

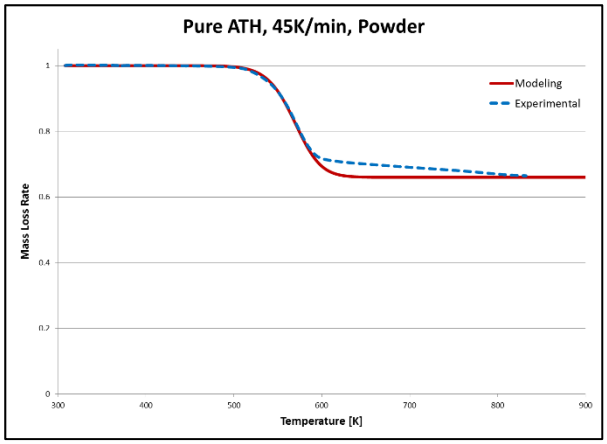

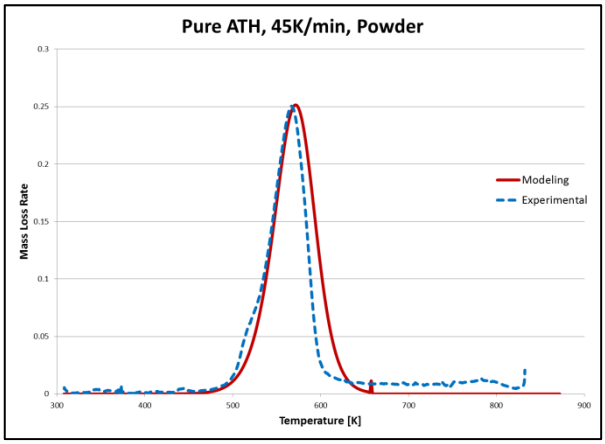

The model is not an exact fit, which is to be expected as we are using a simplified, single nth order reaction. That being said, the model does provide an accurate representation of the overall behavior of ATH as it decomposes, which supports the use of Kim's kinetic model evaluated in this study.

Hetron-ATH (100:0) Model

In this section, the optimized parameters for all Hetron-ATH (100:0) samples are displayed in a table. This table is accompanied by the mass fraction and mass loss rate graphs that depict the experimental and modeled decomposition of Hetron-ATH (100:0) against temperature.

Heating Rate	Weight-loss Fraction, f	Activation Energy, Ea [kJ/mol]	Pre-exponential Const log A [log (/s)]	Exponent, n
10 K/min	0.94	195.37	13.7	1.2
20 K/min	--	--	13.7	1.075
30 K/min	--	--	13.7	1.125
45 K/min	--	--	13.7	1.23

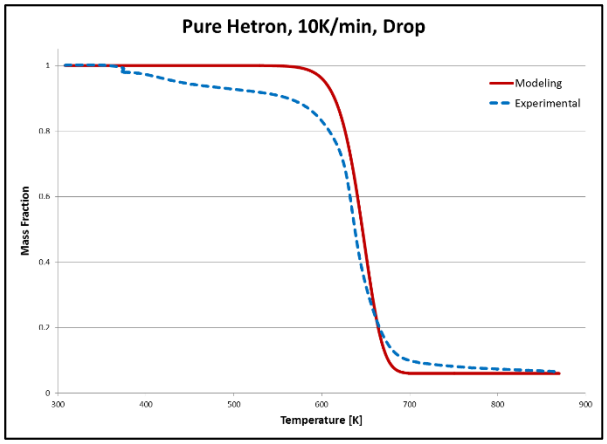
Pure Hetron, 10K/min, Drop
Modeling
Experimental
Mass Fraction
Temperature [K]

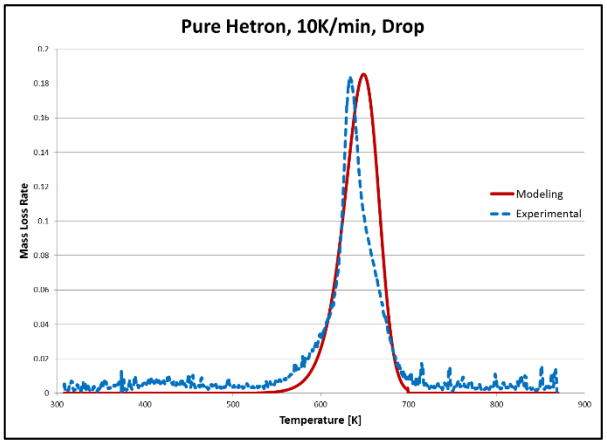
Pure Hetron, 10K/min, Drop
Modeling
Experimental
Mass Loss Rate
Temperature [K]

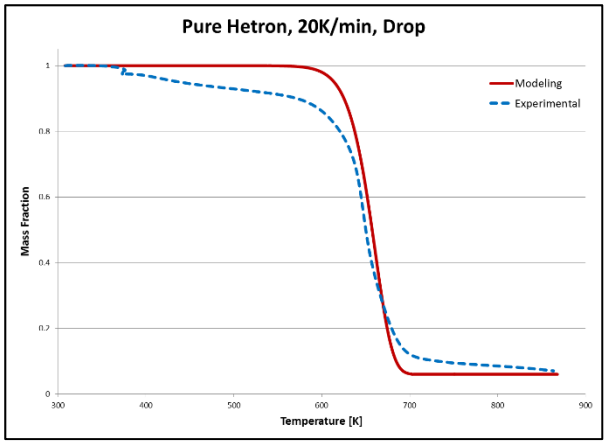
Pure Hetron, 20K/min, Drop
Modeling
Experimental
Mass Fraction
Temperature [K]

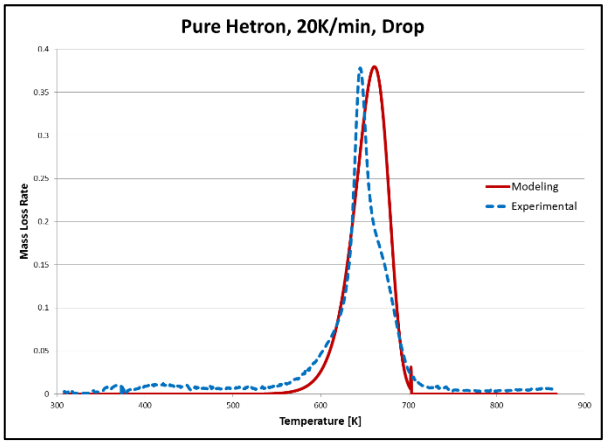
Pure Hetron, 20K/min, Drop
Modeling
Experimental
Mass Loss Rate
Temperature [K]

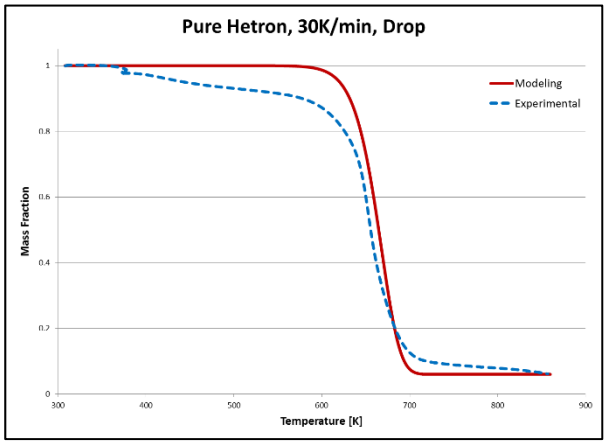
Pure Hetron, 30K/min, Drop
Modeling
Experimental
Mass Fraction
Temperature [K]

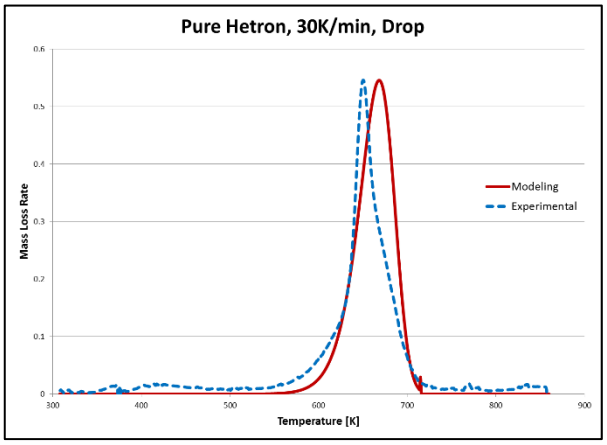
Pure Hetron, 30K/min, Drop
Modeling
Experimental
Mass Loss Rate
Temperature [K]

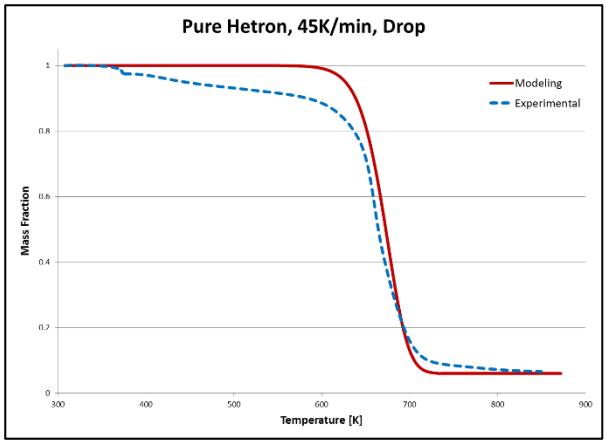

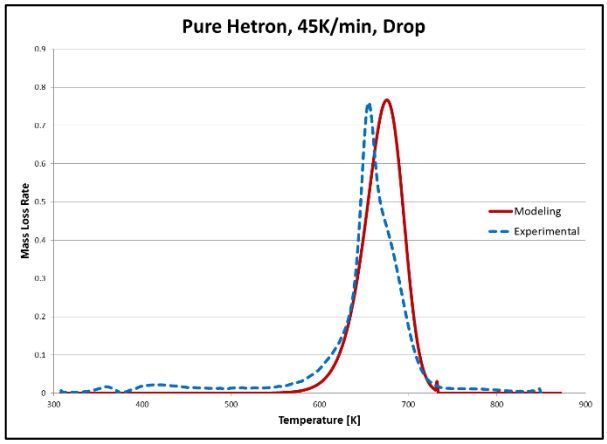

As seen by the above graphs, the model is not an exact fit which is to be expected as we are using a simplified mathematical model to fit a non-uniform decomposition. Overall, the model does provide an accurate representation of the decomposition of Hetron-ATH (100:0) as the model "fits" the temperature ranges and peak heights of the experimental data.

The most prominent discrepancies are seen in the actual shape of the curves. Relative to the mass fractions, it can be observed in all heating cases that the sample starts to decompose and lose mass before the model indicates a decrease in mass; however, once the model's mass fraction does start to decrease, the slope is very similar to the experimental data. In the mass loss rate graphs, the discrepancies are represented by the quick increase in peak height over a short period of time (short range in temperature), and a slow decrease from the peak max back to zero. Since we are modeling pure substances with one reaction, the model can only provide a symmetrical curve. More complex modeling would be required to get an exact fit of the experimental data, either in the form of multiple reactions or a new conversion term.

Hetron-ATH Mixture Model

The mixture models shown in this section are the result of an ideal, additive mixture. Similar to the scaling process described in Appendix: RK4 Modeling for a multiple reaction decomposition curve, the ideal mixture model scaled the optimized parameters of pure Hetron and ATH by their respective weight-loss fractions, f. Additionally, these parameters were proportioned by their percentage in the mixture. For a two component mixture the following equation was used to calculate alpha at each time step:

$$\propto_{total}(t) = f_1 r_1 \propto_1 + f_2 r_2 \propto_2 \qquad f_n r_n = Z_n$$

Subscript “1” denotes the first component; subscript “2” denotes the second; “r” represents the corresponding mass ratio of a component in the mixture; and “Z” is the scaling constant.

The first table below shows the proportioned, optimized parameters used for each Hetron ATH mixture; the second s. Following the table are the modeled mass fraction and mass loss curves for powder and drop mixtures at 30K/min.

Optimized Parameters	Pure Hetron	Pure ATH
Activation Energy, Ea	195.37	140.1
Pre-exponential Const, log A	13.7	11.4
Exponent, n	1.125	1.25
Weight-loss fraction, f	0.94	0.34

Mixture Ratio Hetron : ATH	Scaling Constant, Z_{Hetron}	Scaling Constant, Z_{ATH}
100 : 33	0.707	0.084
100 : 66	0.566	0.135
100 : 100	0.47	0.17
100 : 130	0.409	0.192

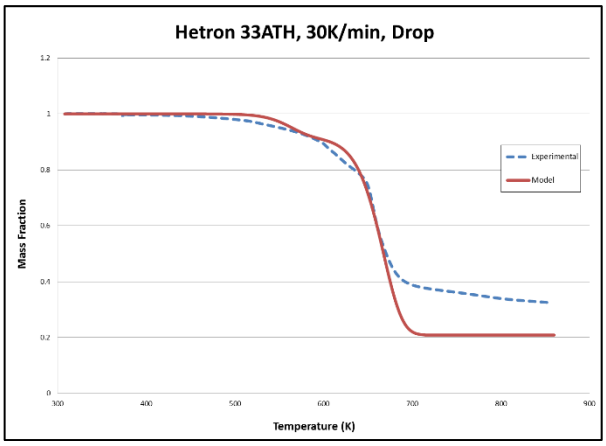

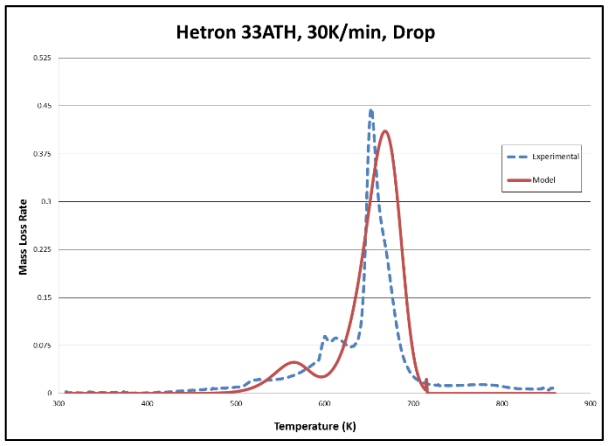

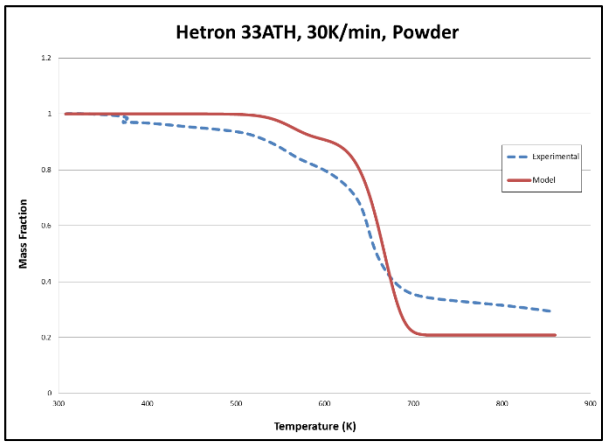

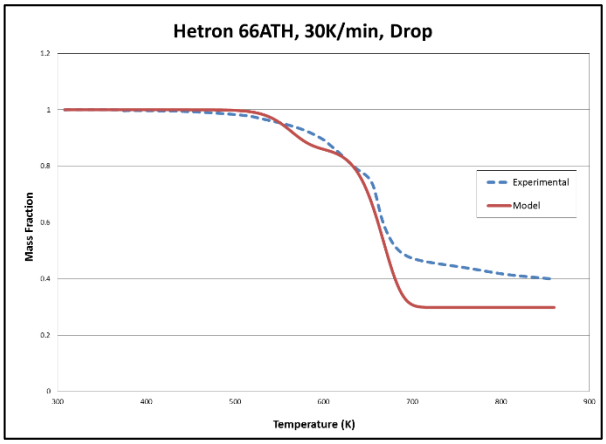
Hetron 66ATH, 30K/min, Drop
Mass Fraction
Temperature (K)
Experimental
Model

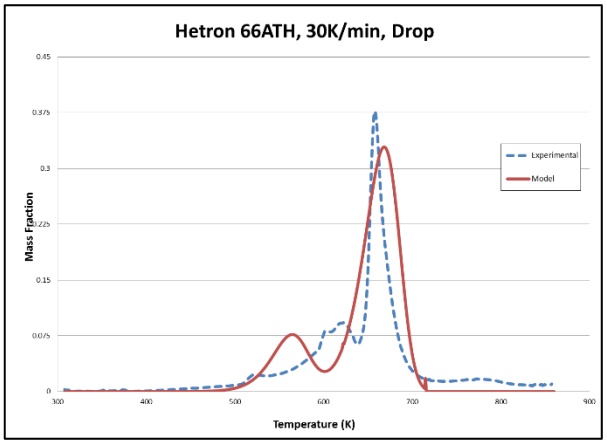
Hetron 66ATH, 30K/min, Drop
Mass Fraction
Temperature (K)
Experimental
Model

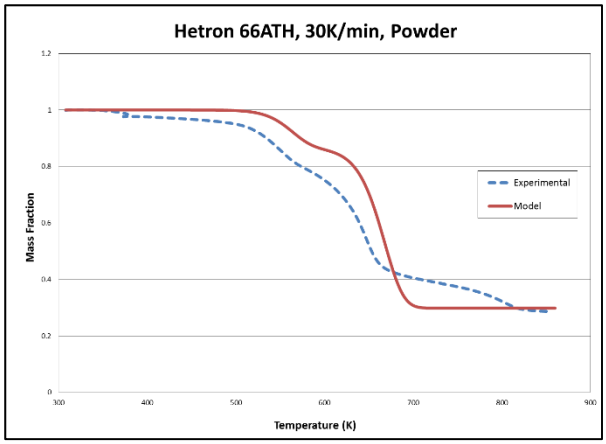
Hetron 66ATH, 30K/min, Powder
Mass Fraction
Temperature (K)
Experimental
Model

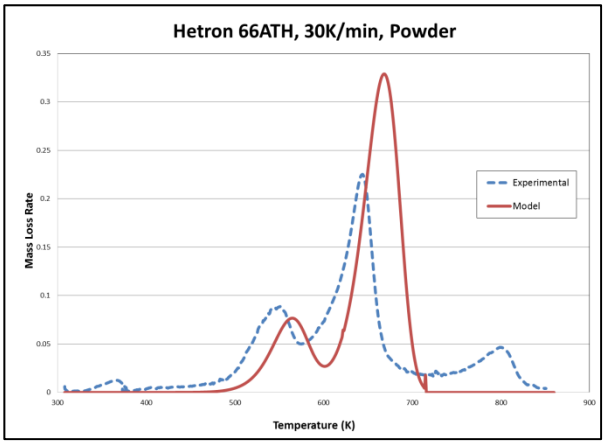
Hetron 66ATH, 30K/min, Powder
Mass Loss Rate
Temperature (K)
Experimental
Model

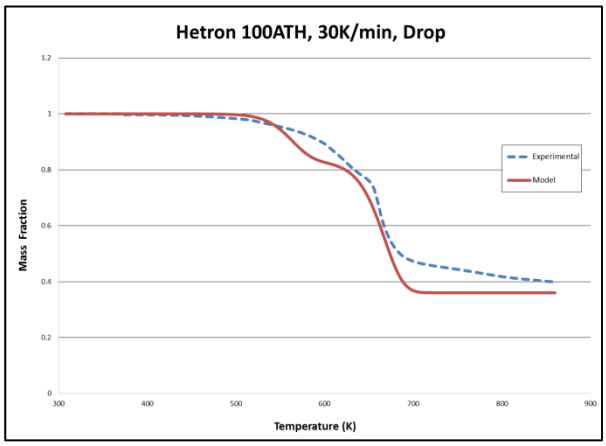
Hetron 100ATH, 30K/min, Drop
Mass Fraction
Temperature (K)
Experimental
Model

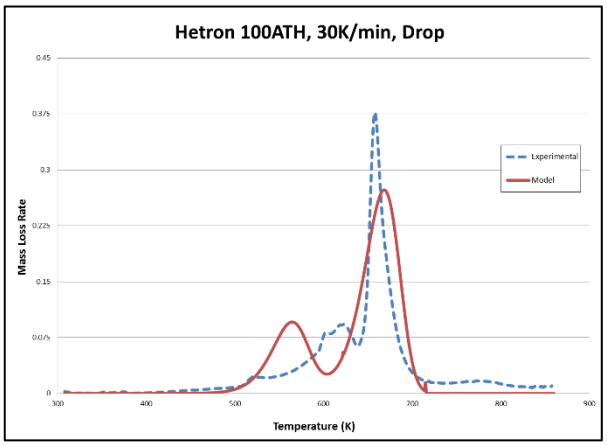
Hetron 100ATH, 30K/min, Drop
Mass Loss Rate
Temperature (K)
Experimental
Model

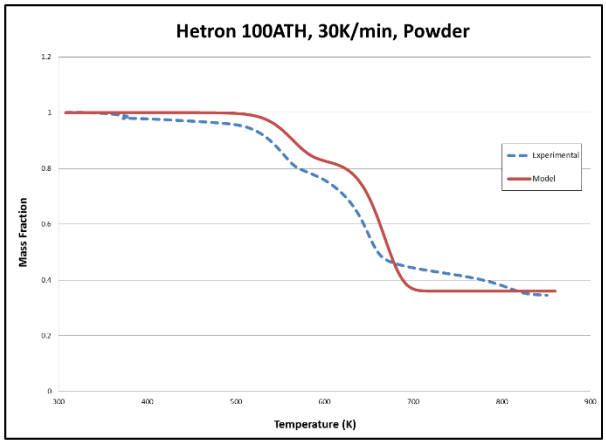

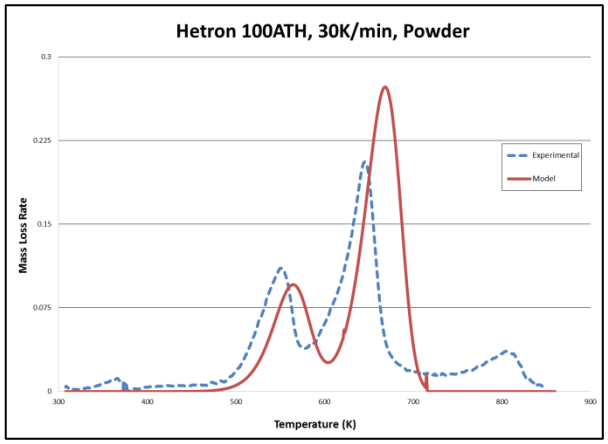

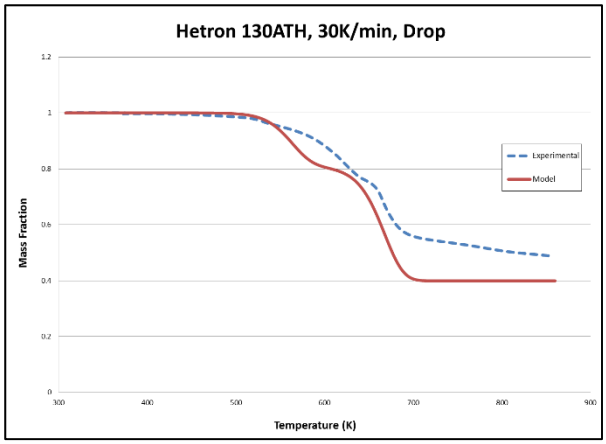

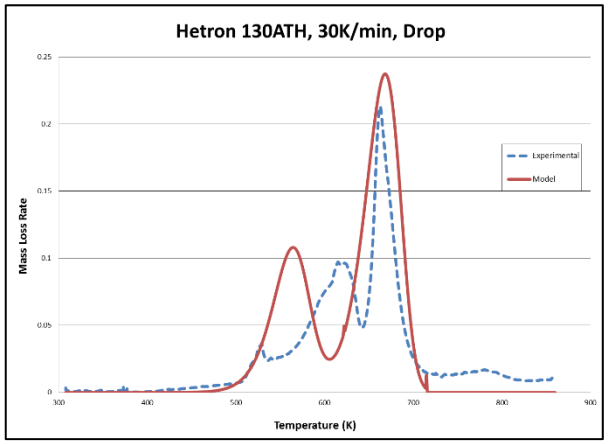

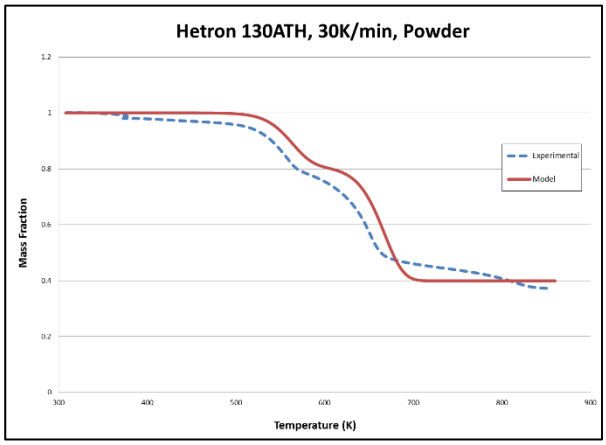

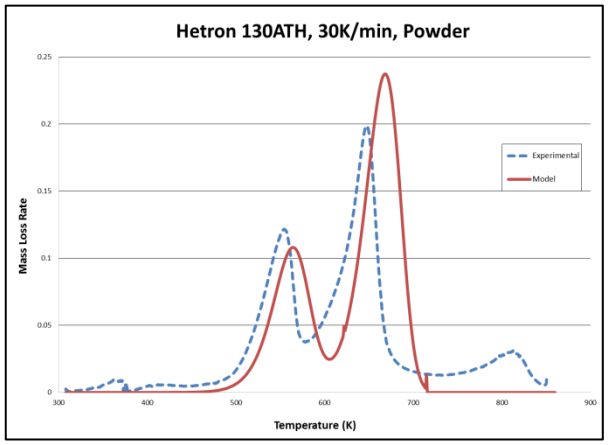

Overall observations that can be made for the mixture models are related to morphology.

1. A transport effect is seen in what would be considered the “ATH” peak in the mass loss graphs, as the modeled peak is shifted to an early temperature in the drop samples. This is further seen in the mass fraction graphs as the decline begins earlier than the experimental. This shift is believed to be a result of the ATH parameters being optimized for a powder sample.

2. The final mass fractions for the drop samples is continually lower for the models than the experimental data in all mixtures. In the pure Hetron models, the modeled curve covers a larger area than the experimental data due to the symmetrical behavior of the model. This inconsistency is then carried over to the modeling.
3. The behavior and overall shape of the powder mixtures follows that of the experimental data much more closely than the drop. Again, this is believed to be a result of using powder ATH parameters in the ideal mixing model.
4. The "Hetron peak" in the powder sample is overestimated by the model. Since the final mass fractions of the model closely match that of the experimental, it shows that the integrals of the model and experimental data are equal. However, additional peaks are seen in the experimental powder data that are not accounted for in the ideal mixing model. Powder was observed to be much more variable than the drop in its decomposition behavior, so it is believed that this variance is the result of new peaks.

Hetron Mixtures: Heat of Decomposition Model

The heat of decomposition for each mixture was determined using the process described in Appendix F.3: Heat of Decomposition; they can be found below.

Sample			Heat of Decomposition [J/g]	Peak Temperature [K]
Amt. ATH	Medium	Heating Rate [C/min]		
0	Drop	10	52	647
0	Drop	10	71	647
0	Drop	5	82	633
33	Drop	10	272	602
33	Drop	5	231	587
66	Drop	10	340	604
66	Drop	5	299	595
100	Drop	10	401	627
100	Drop	5	354	593
130	Drop	10	645	608
130	Drop	5	768	594
Pure	Powder	10	999	596
Pure	Powder	5	988	588
0	Powder	10	172	637
33	Powder	10	214	585
66	Powder	10	606	593
100	Powder	10	97	637
130	Powder	10	--	--

Appendix J: Ashland Fireblock Gelcoat Data

Gelcoat Fireblock-Sand (100:0)

TGA tests were run with Gelcoat Fireblock, 0 Sand samples at four different heating rates: 10, 20, 30, and 45 K/min.

Single Heating Rate Method

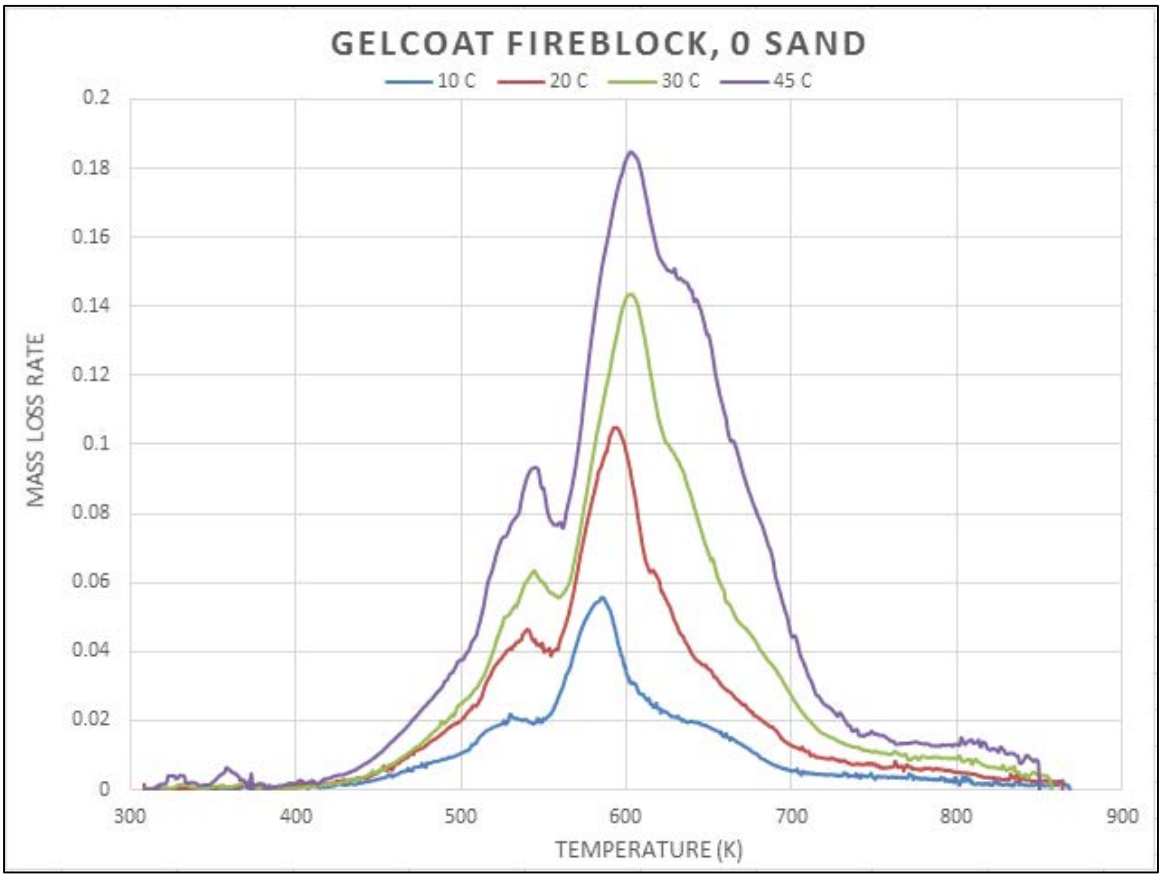

Figure 61: Single Heating Rate Method of Gelcoat Fireblock 0 Sand at Various Heating Rates

Single Heating Rate Method – Peak Temperature and Activation Energy

Table 1: Peak Temperature and Activation Energies

Heating Rate (K/min)	Peak Temp (K)	Activation Energy (kJ/mol)	Pre-Exponential Factor (A)
10	48.22917	164.3633	2.62E+14
20	34.69584	161.0782	1.73E+14
30	30.3375	160.0591	1.21E+14
45	27.0625	145.986	9.69E+12

OFW Isoconversional Method

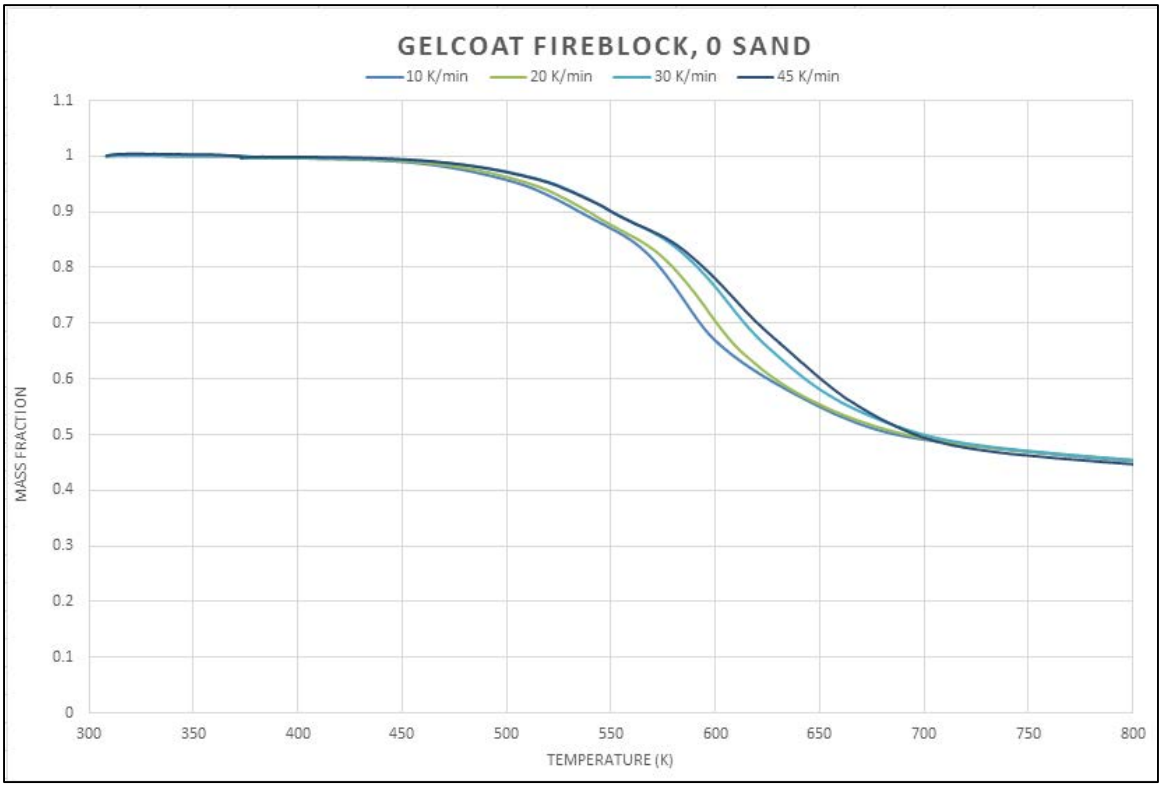

Figure 62: Multiple Heating Rate for TGA Gelcoat Fireblock, 0 Sand

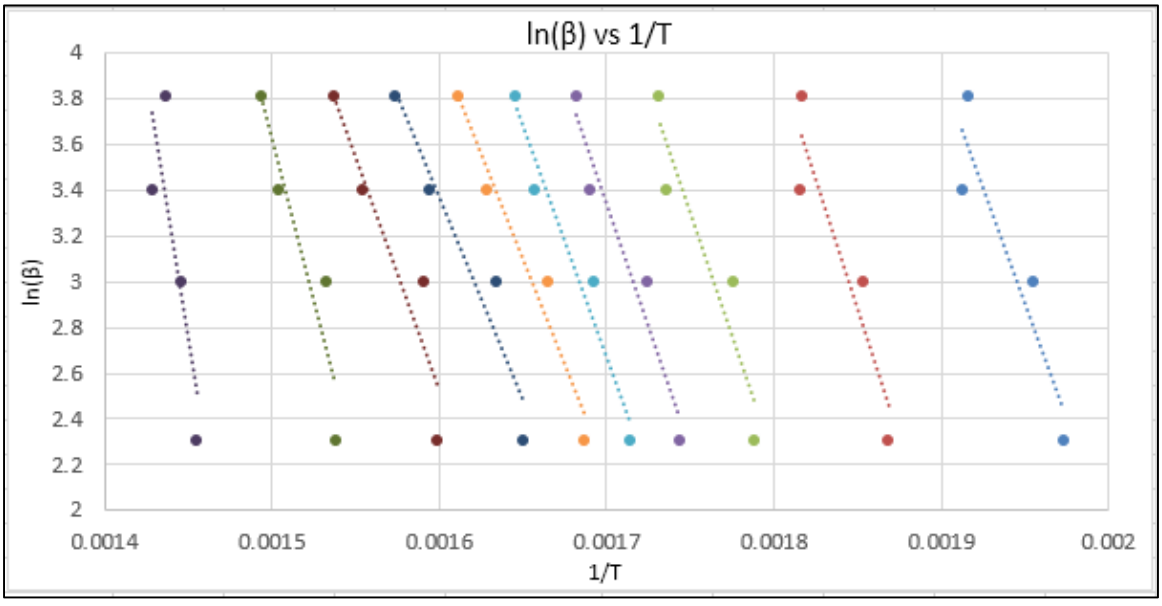

Figure 63: Intermediate Step in isoconversional method

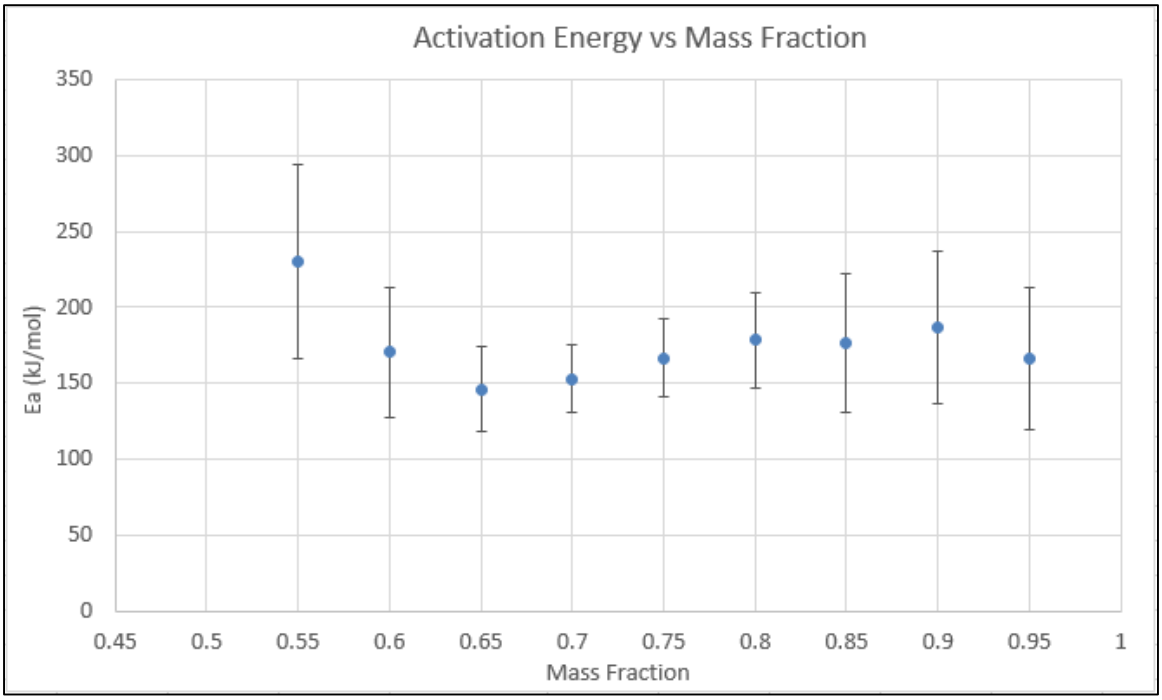

Figure 64: Activation energy trend observed at varying alpha values

Multiple Heating Rate – Activation Energy

Table 2: Gelcoat Fireblock Error and Activation Energy

α	Slope	LINEST	Ea (kJ/mol)	Error
0.95	-20053.29	5629.79	166.72	46.81
0.90	-22500.67	6003.32	187.07	49.91
0.85	-21265.03	5509.69	176.80	45.81
0.80	-21461.19	3794.01	178.43	31.54
0.75	-20059.86	3068.66	166.78	25.51
0.70	-18376.58	2657.91	152.78	22.10
0.65	-17589.18	3377.72	146.24	28.08
0.60	-20486.23	5143.00	170.32	42.76
0.55	-27730.64	7679.90	230.55	63.85
0.50	-46799.19	21350.01	389.09	177.50
0.45	21239.66	16288.01	-176.59	135.42

Powder, Chunk, and Drop Analysis

TGA tests were run with Gelcoat Fireblock 0 Sand at the same heating rate, 30 K/min, for three different morphologies: powder, chunk, and drop.

Single Heating Rate Method

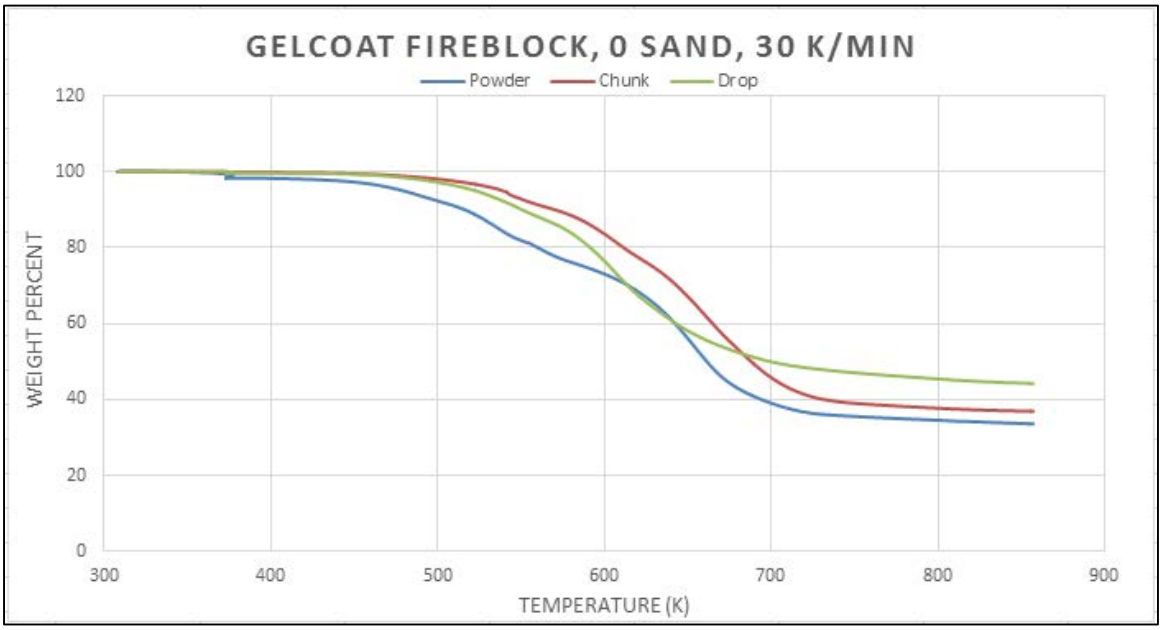

Figure 65: Powder, chunk, and drop samples single heating rate method at 30 K/min

Mass Loss History

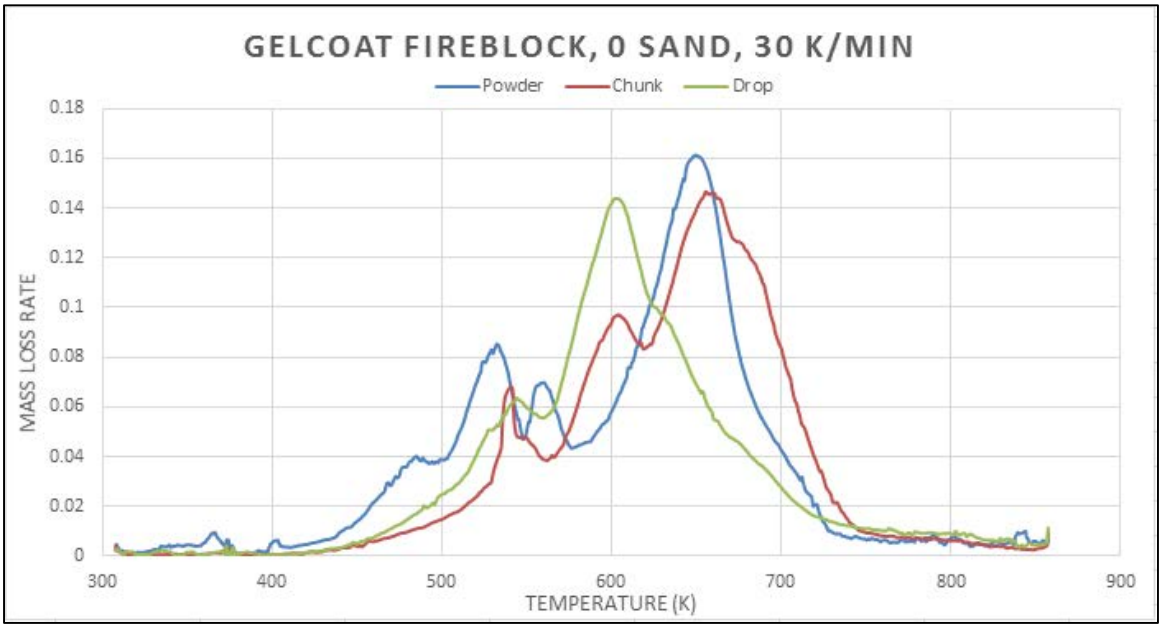

Figure 66: Powder, chunk, and drop data at 30 K/min

Gelcoat Fireblock-Sand (70:30)

TGA tests were run with Gelcoat Fireblock, 30 Sand samples at four different heating rates: 10, 20, 30, and 45 K/min.

Single Heating Rate Method

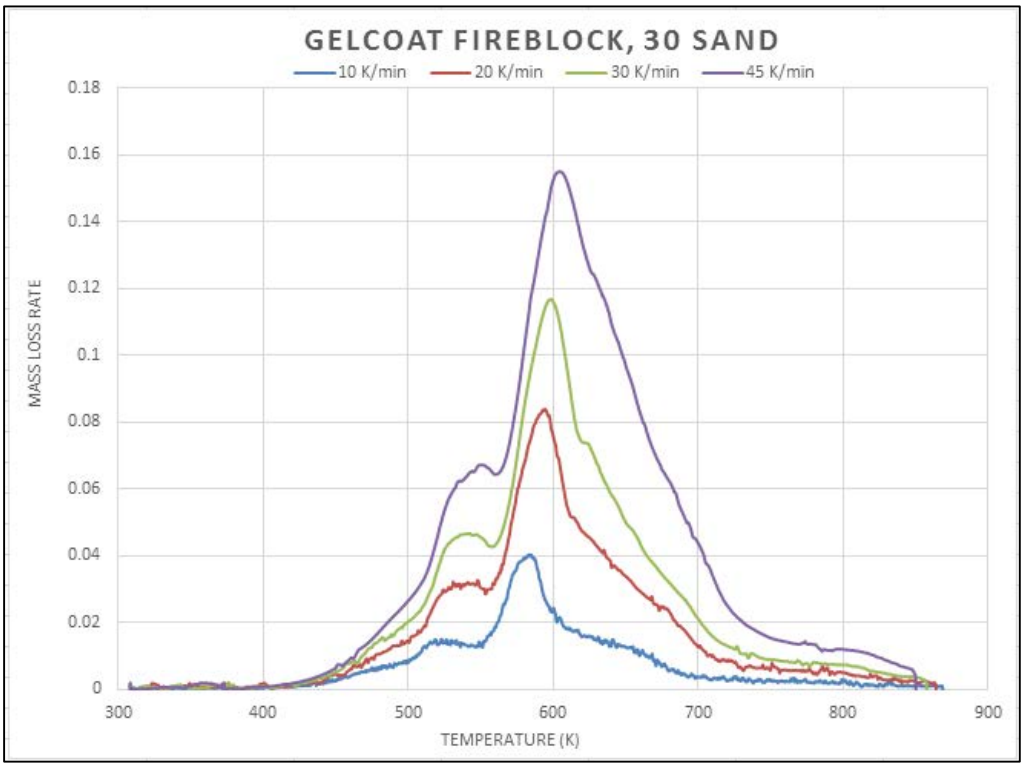

Figure 67: Single Heating Rate Method of Gelcoat Fireblock 30 Sand at Various Heating Rates

Single Heating Rate Method – Peak Temperature and Activation Energy

Table 1: Peak Temperature and Activation Energies

Heating Rate (K/min)	Peak Temp (K)	Activation Energy (kJ/mol)	Pre-Exponential Factor (A)
10	584.9687	161.7499285	1.5802E+14
20	594.7649	163.1576713	2.37037E+14
30	598.6099	164.6538276	3.87071E+14
45	604.7117	157.1735941	8.78492E+13

OFW Isoconversional Method

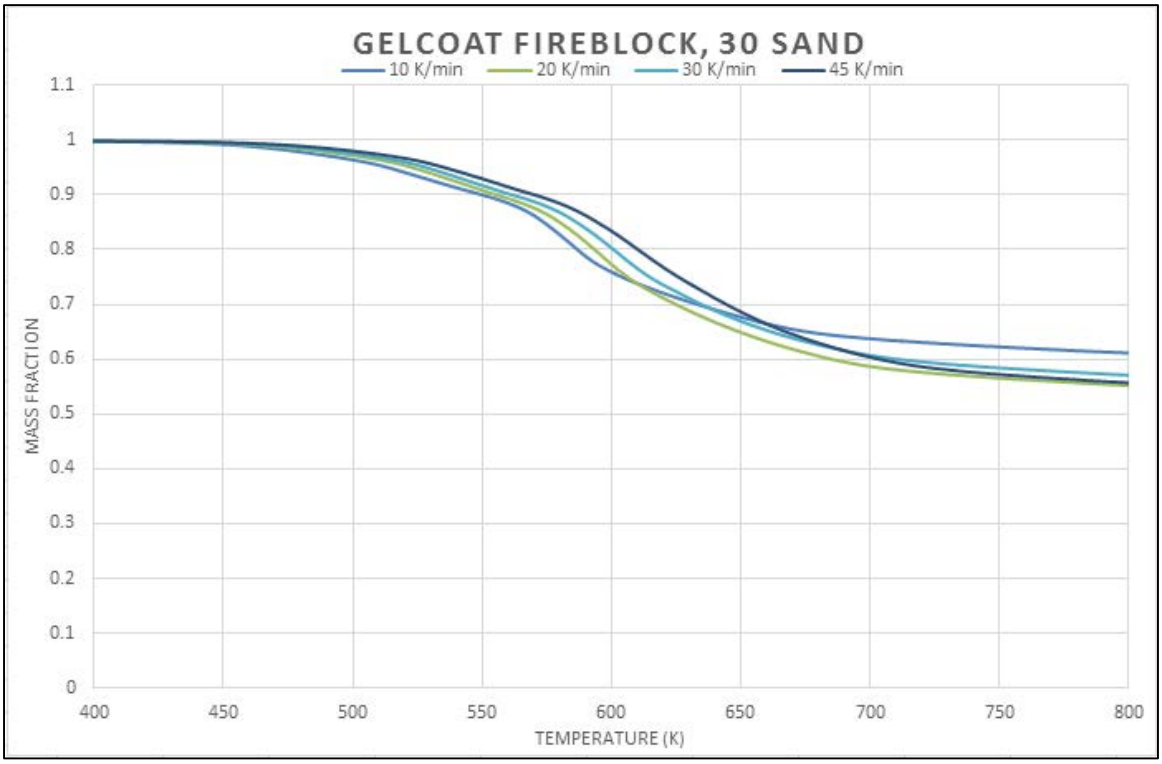

Figure 68: Multiple Heating Rate for TGA Gelcoat Fireblock, 30 Sand

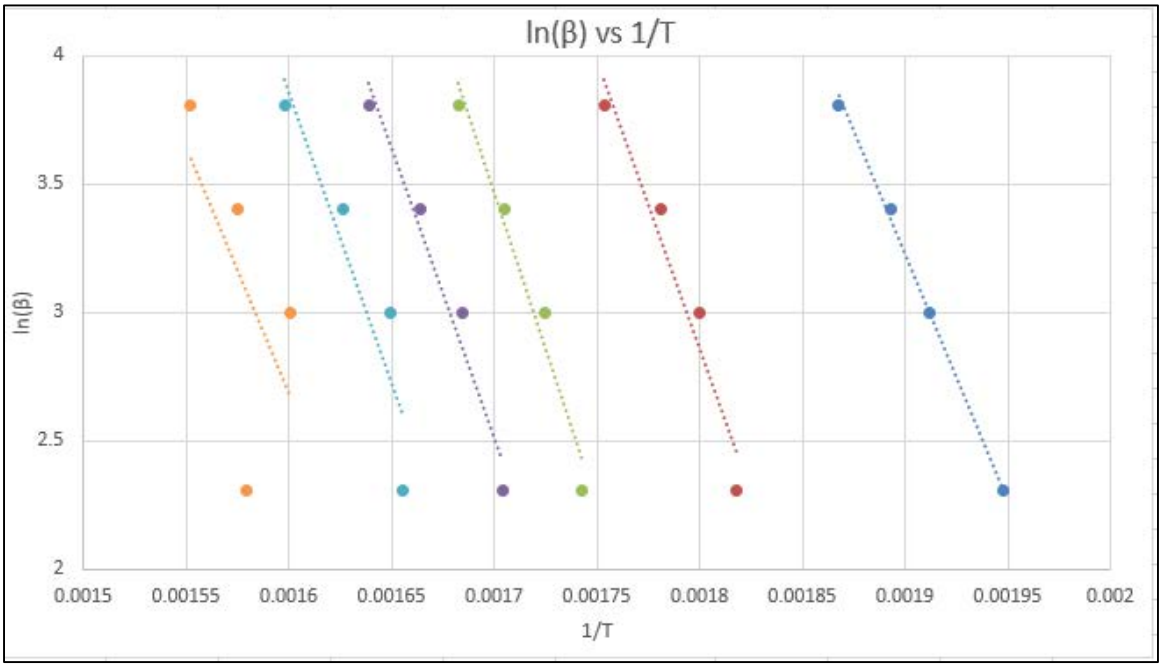

Figure 69: Intermediate Step in isoconversional method

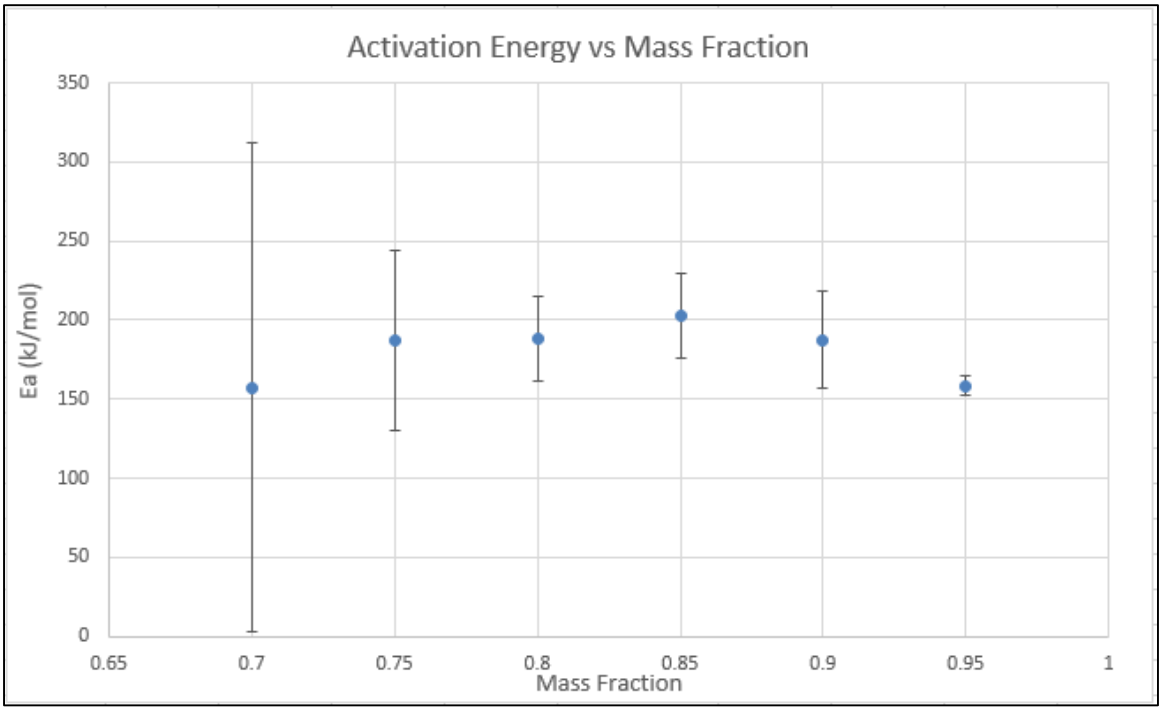

Figure 70: Activation energy trend observed at varying alpha values

Multiple Heating Rate – Activation Energy

Table 2: Gelcoat Fireblock Error and Activation Energy

α	Slope	LINEST	Ea (kJ/mol)	Error
0.95	-19052.45	746.37	158.40	6.21
0.90	-22573.89	3667.10	187.68	30.49
0.85	-24363.56	3203.67	202.56	26.64
0.80	-22642.27	3159.82	188.25	26.27
0.75	-22559.70	6840.97	187.56	56.88
0.70	-18933.27	18591.94	157.41	154.57

Powder, Chunk, and Drop Analysis

TGA tests were run with Gelcoat Fireblock 30 Sand at the same heating rate, 30 K/min, for three different morphologies: powder, chunk, and drop.

Single Heating Rate Method

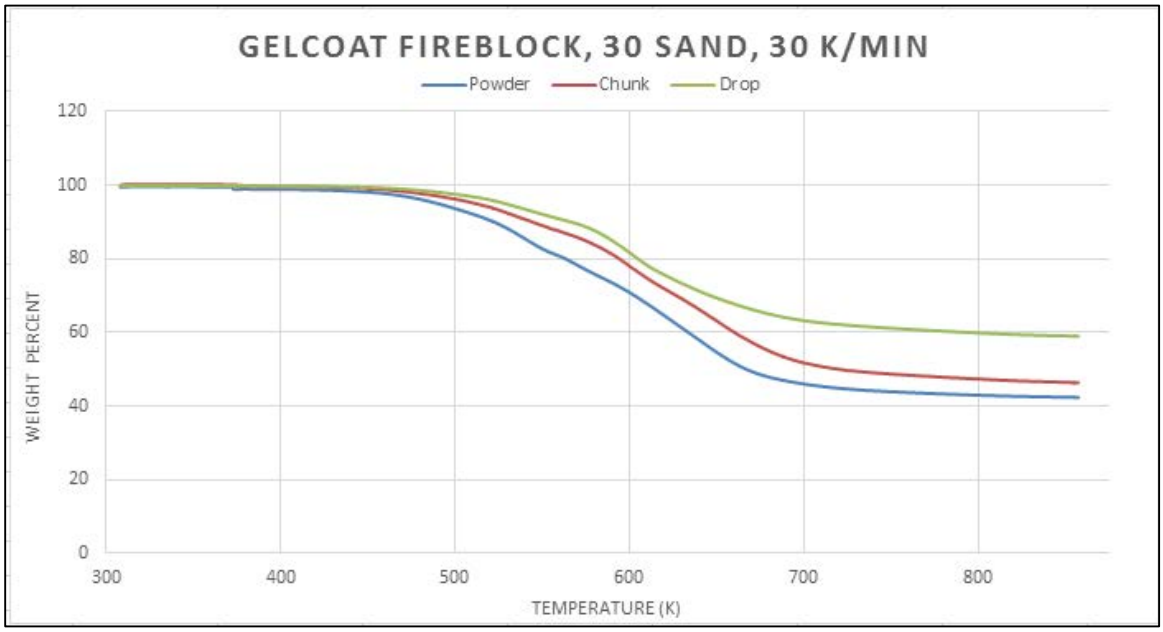

Figure 71: Powder, chunk, and drop samples at single heating rate, 30 K/min

Mass Loss History

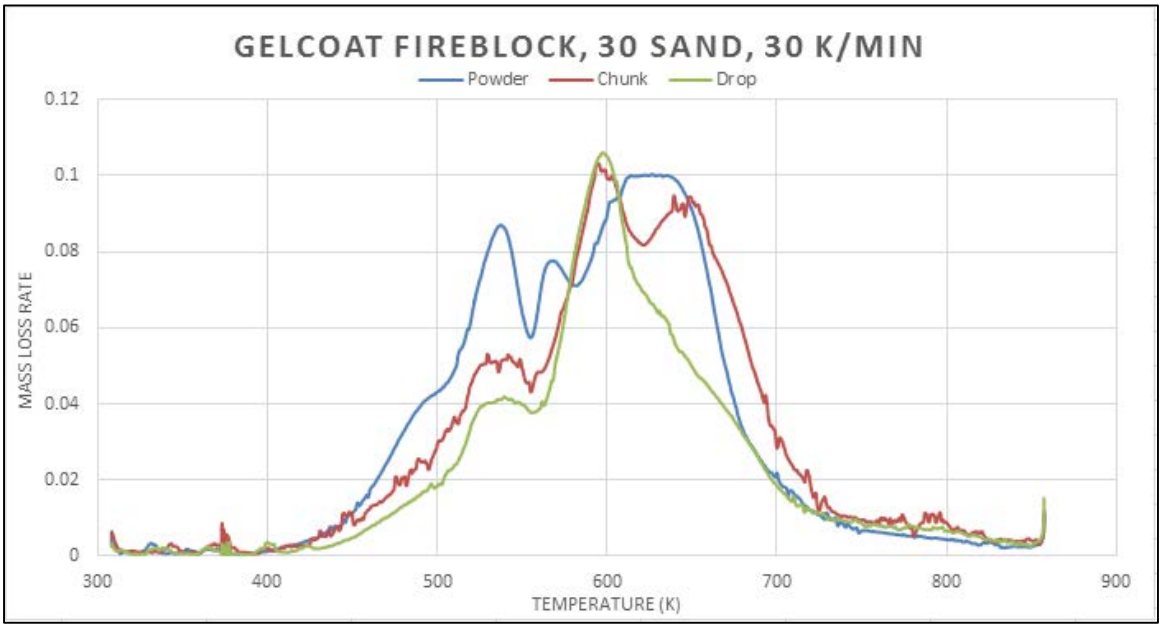

Figure 72: Powder, chunk, and drop data at 30 K/min

Gelcoat Fireblock-Sand (60:40)

TGA tests were run with Gelcoat Fireblock, 40 Sand samples at four different heating rates: 10, 20, 30, and 45 K/min.

Single Heating Rate Method

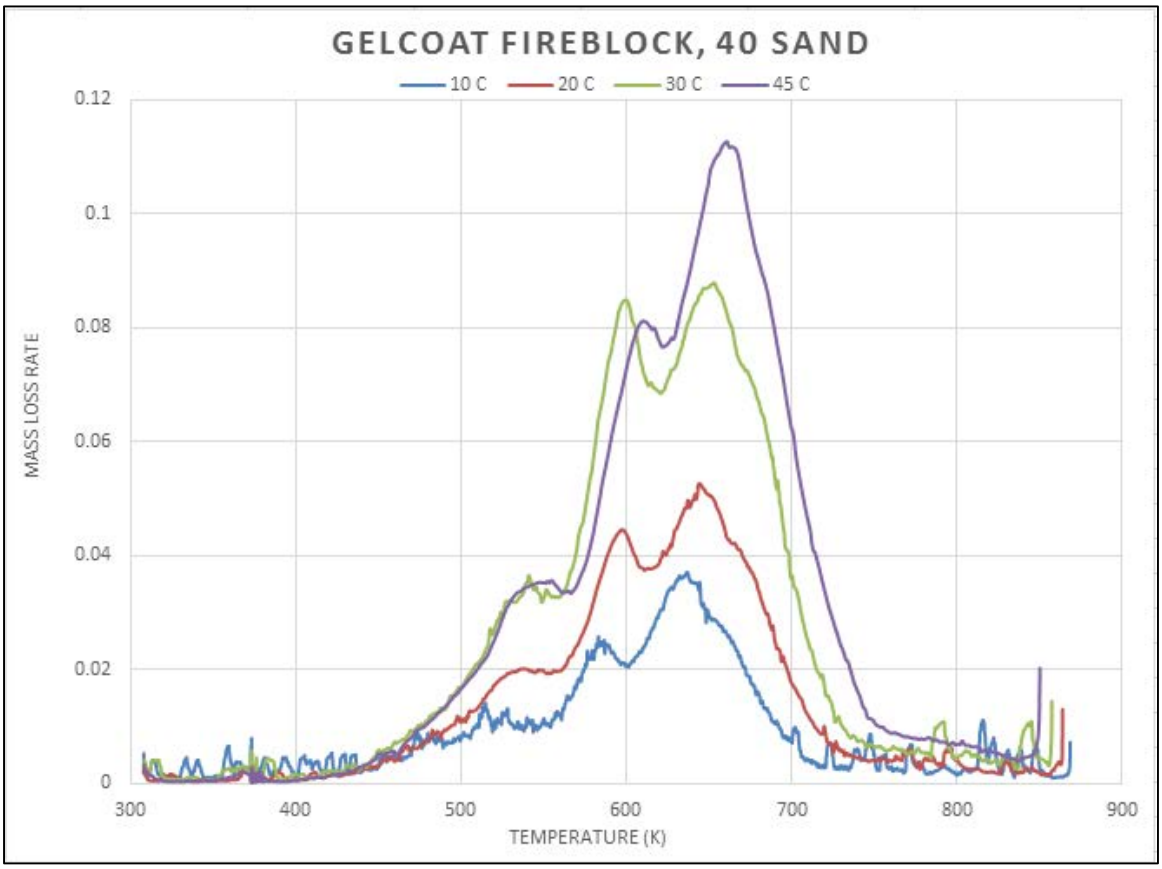

Figure 73: Single Heating Rate Method of Gelcoat Fireblock 40 Sand at Various Heating Rates

Single Heating Rate Method – Peak Temperature and Activation Energy

Table 1: Peak Temperature and Activation Energies

Heating Rate (K/min)	Peak Temp (K)	Activation Energy (kJ/mol)	Pre-Exponential Factor (A)
10	53.3875	122.7100567	4129479198
20	37.2625	107.9609571	355051074.9
30	32.0125	100.3061179	89909583.15
45	28.40417	119.1214179	3475821789

OFW Isoconversional Method

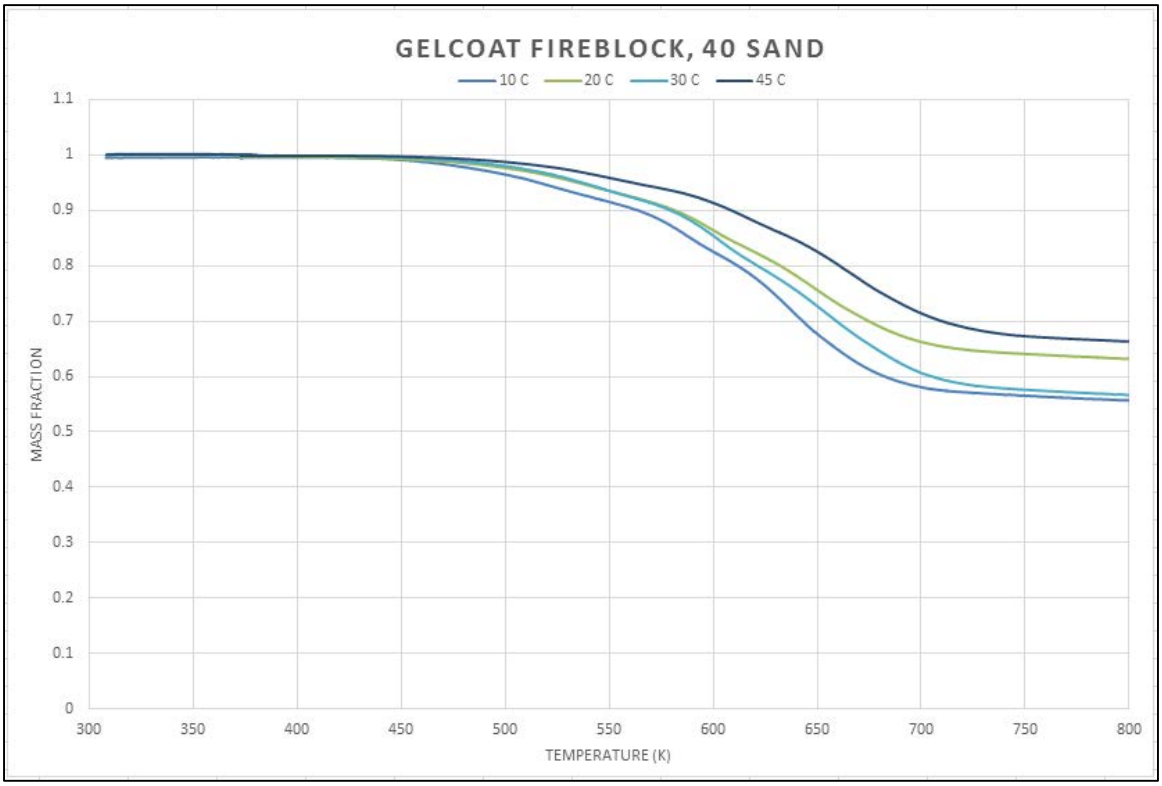

Figure 74: Multiple Heating Rate for TGA Gelcoat Fireblock, 40 Sand

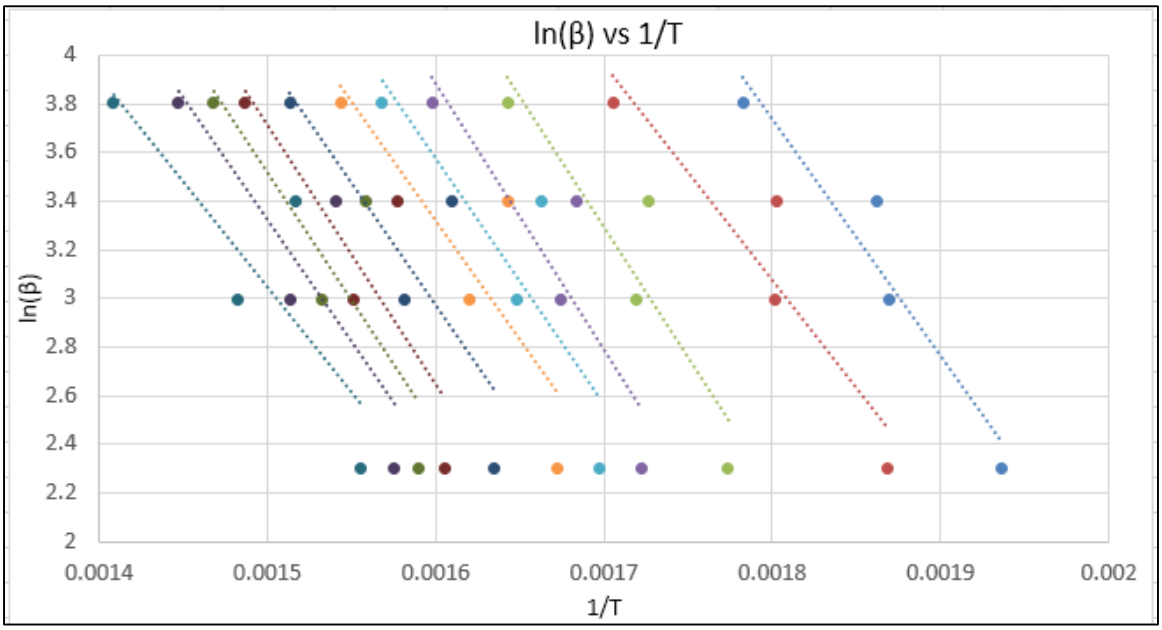

Figure 75: Intermediate Step in isoconversional method

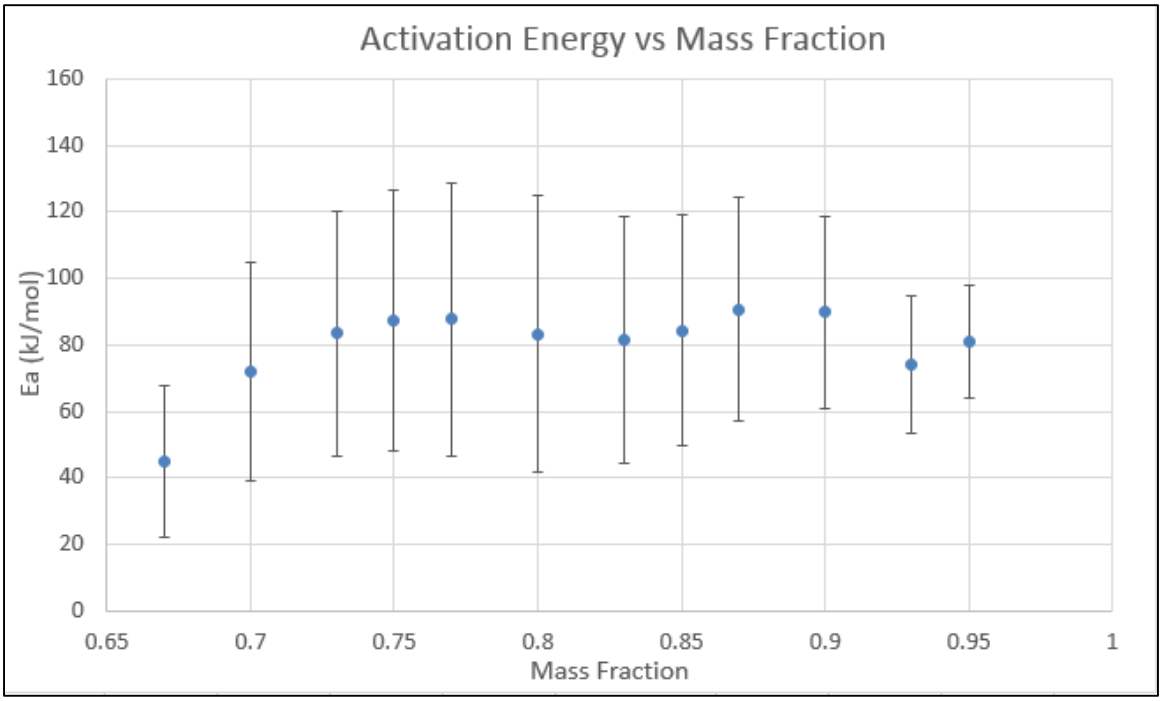

Figure 76: Activation energy trend observed at varying alpha values

Multiple Heating Rate – Activation Energy

Table 2: Gelcoat Fireblock Error and Activation Energy

α	Slope	LINEST	Ea (kJ/mol)	Error
0.95	-9743.30	2017.72	81.01	16.78
0.93	-8905.71	2456.92	74.04	20.43
0.90	-10802.06	3471.48	89.81	28.86
0.87	-10908.73	4044.06	90.70	33.62
0.85	-10149.13	4161.03	84.38	34.59
0.83	-9792.06	4472.19	81.41	37.18
0.80	-10021.49	4992.20	83.32	41.51
0.77	-10549.22	4945.63	87.71	41.12
0.75	-10489.39	4705.79	87.21	39.12
0.73	-10026.27	4426.54	83.36	36.80
0.70	-8636.63	3947.30	71.80	32.82
0.67	-5398.44	2771.12	44.88	23.04

Powder, Chunk, and Drop Analysis

TGA tests were run with Gelcoat Fireblock 40 Sand at the same heating rate, 30 K/min, for three different morphologies: powder, chunk, and drop.

Single Heating Rate Method

Figure 77: Powder, chunk, and drop samples single heating rate method at 30 K/min

Mass Loss History

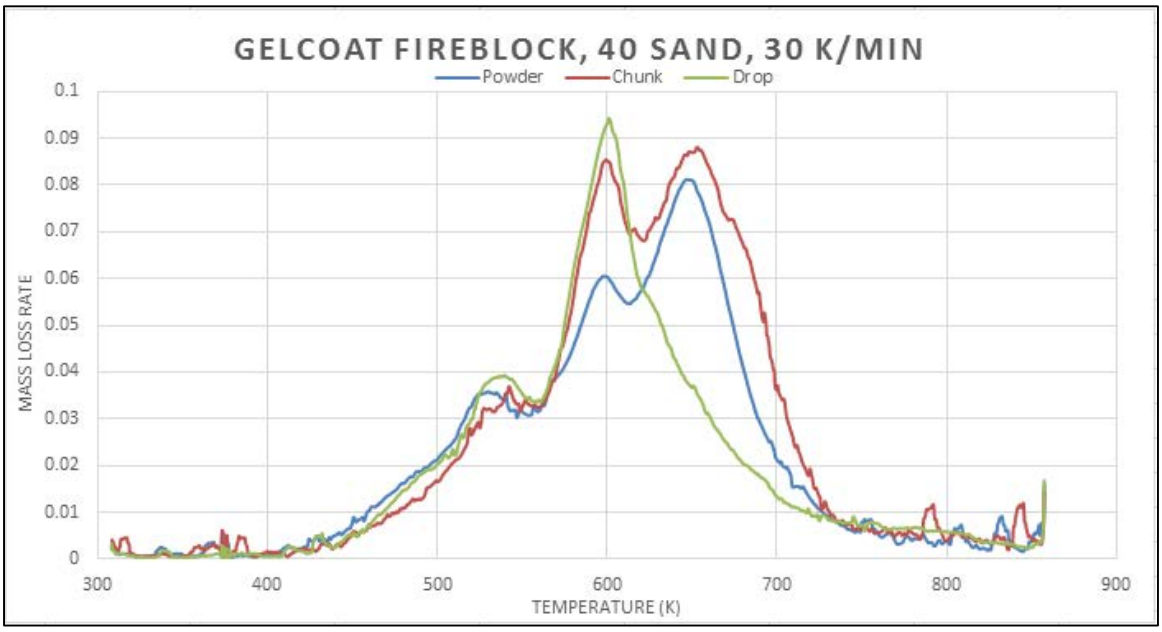

Figure 78: Powder, chunk, and drop data at 30 K/min

Gelcoat Fireblock-Sand (50:50)

TGA tests were run with Gelcoat Fireblock, 50 Sand samples at four different heating rates: 10, 20, 30, and 45 K/min.

Single Heating Rate Method

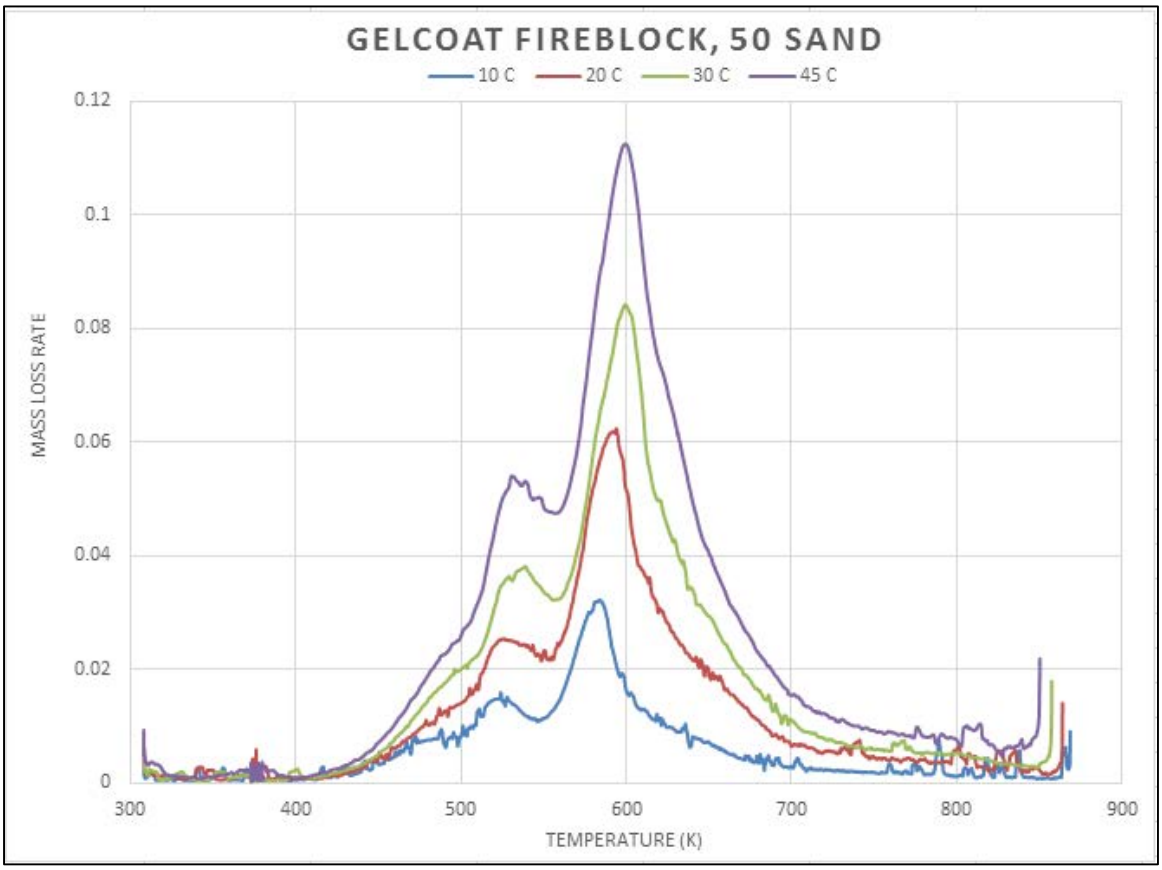

Figure 79: Single Heating Rate Method of Gelcoat Fireblock 50 Sand at Various Heating Rates

Single Heating Rate Method – Peak Temperature and Activation Energy

Table 1: Peak Temperature and Activation Energies

Heating Rate (K/min)	Peak Temp (K)	Activation Energy (kJ/mol)	Pre-Exponential Factor (A)
10	48.0375	146.9193593	7.22162E+12
20	34.75416	151.3561714	2.11743E+13
30	30.2375	148.9004591	1.41858E+13
45	26.97916	146.0202768	1.18391E+13

OFW Isoconversional Method

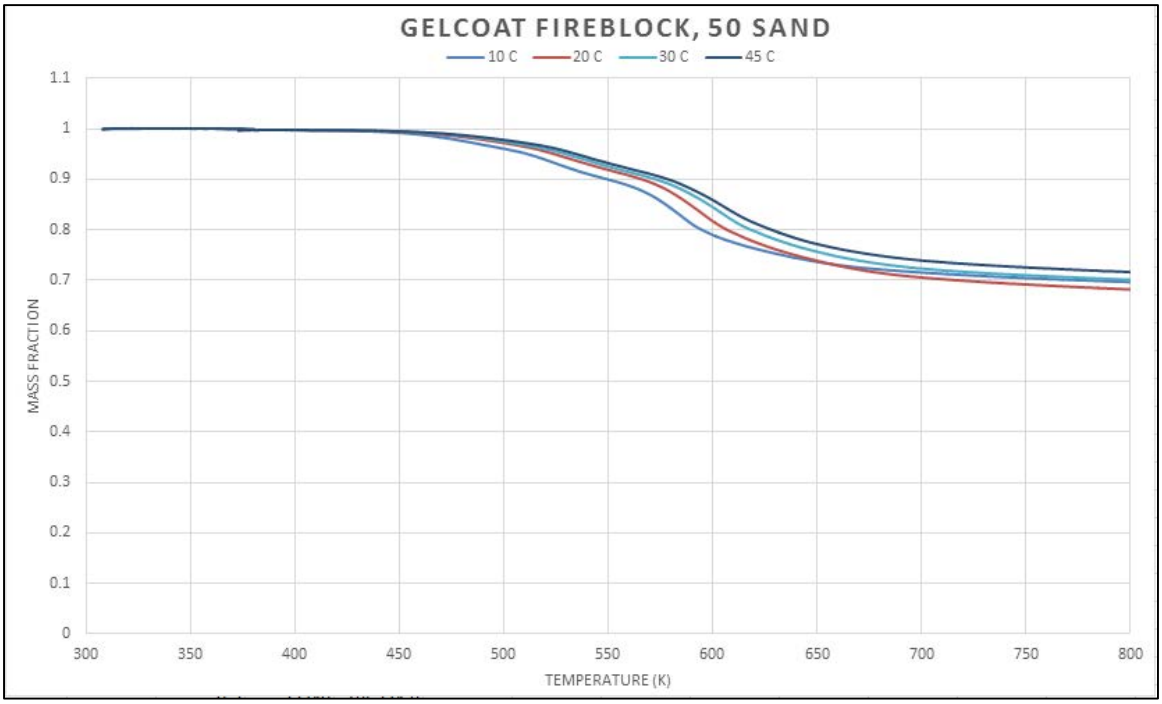

Figure 80: Multiple Heating Rate for TGA Gelcoat Fireblock, 50 Sand

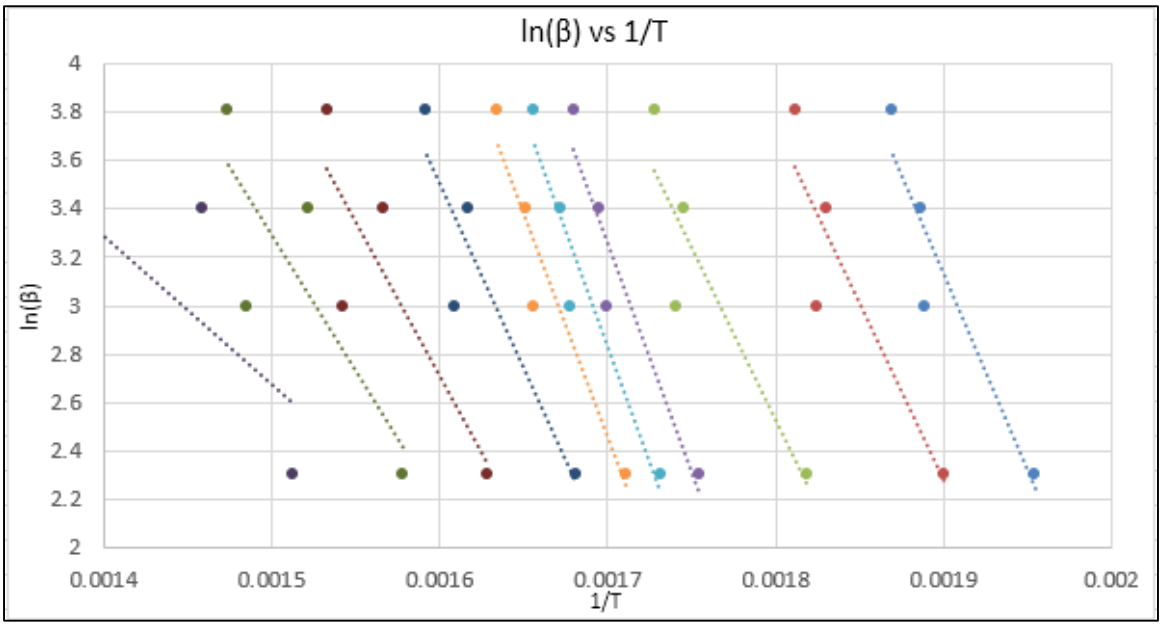

Figure 81: Intermediate Step in isoconversional method

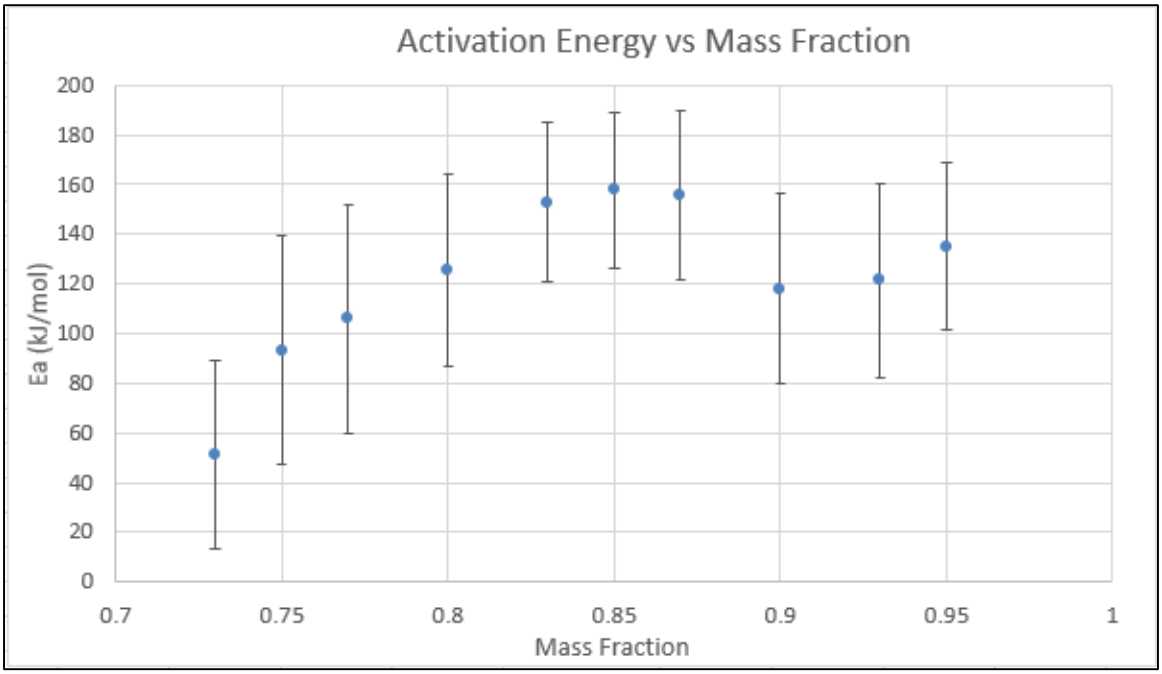

Figure 82: Activation energy trend observed at varying alpha values

Multiple Heating Rate – Activation Energy

Table 2: Gelcoat Fireblock Error and Activation Energy

α	Slope	LINEST	Ea (kJ/mol)	Error
0.95	-16225.76	4061.48	134.90	33.77
0.93	-14600.63	4683.08	121.39	38.94
0.90	-14203.59	4638.47	118.09	38.56
0.87	-18736.69	4106.14	155.78	34.14
0.85	-18967.74	3785.97	157.70	31.48
0.83	-18384.75	3858.92	152.85	32.08
0.80	-15081.26	4660.64	125.39	38.75
0.77	-12755.90	5528.29	106.05	45.96
0.75	-11214.78	5519.74	93.24	45.89
0.73	-6167.82	4570.59	51.28	38.00

Powder, Chunk, and Drop Analysis

TGA tests were run with Gelcoat Fireblock 50 Sand at the same heating rate, 30 K/min, for three different morphologies: powder, chunk, and drop.

Single Heating Rate Method

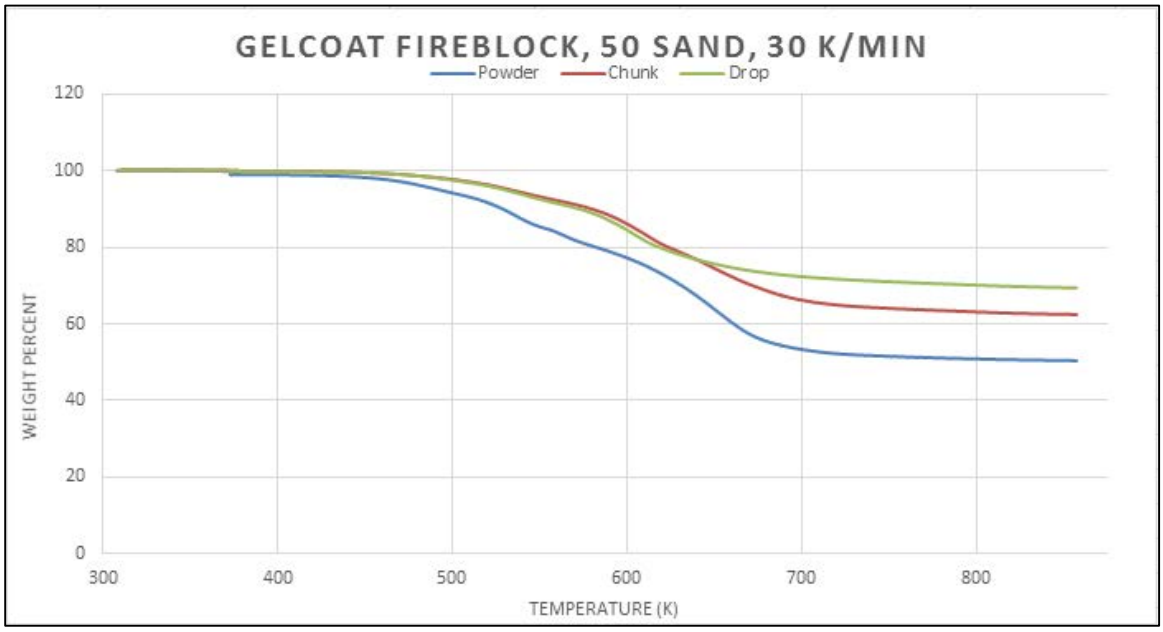

Figure 83: Powder, chunk, and drop samples at single heating rate, 30 K/min

Mass Loss History

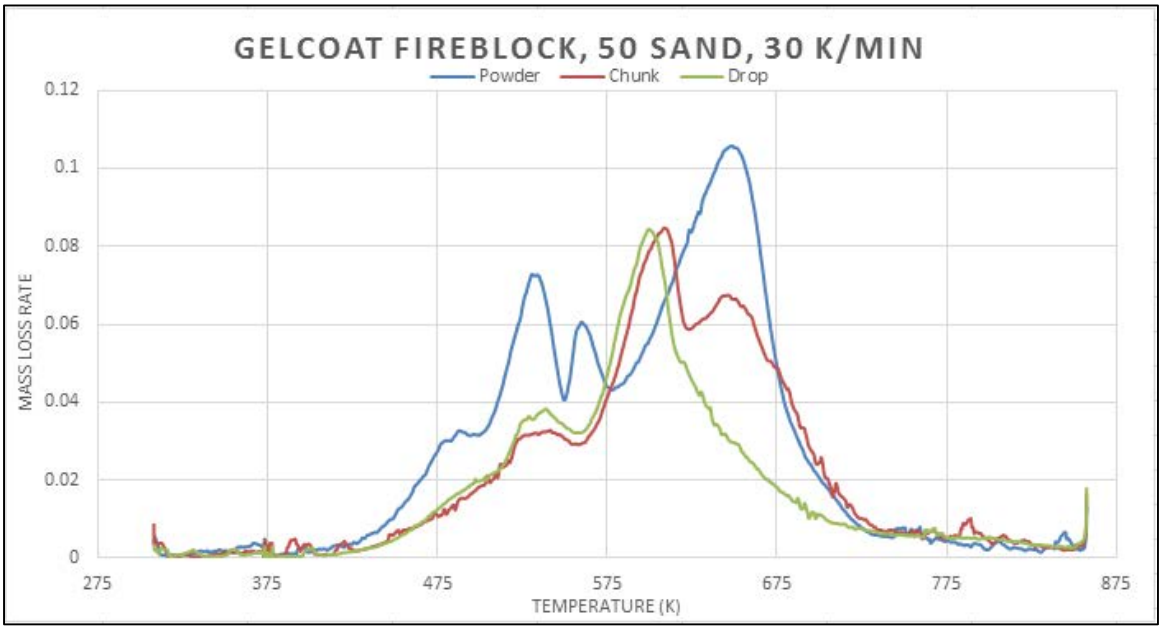

Figure 84: Powder, chunk, and drop data at 30 K/min

Gelcoat Fireblock-Sand (40:60)

TGA tests were run with Gelcoat Fireblock, 60 Sand samples at four different heating rates: 10, 20, 30, and 45 K/min.

Single Heating Rate Method

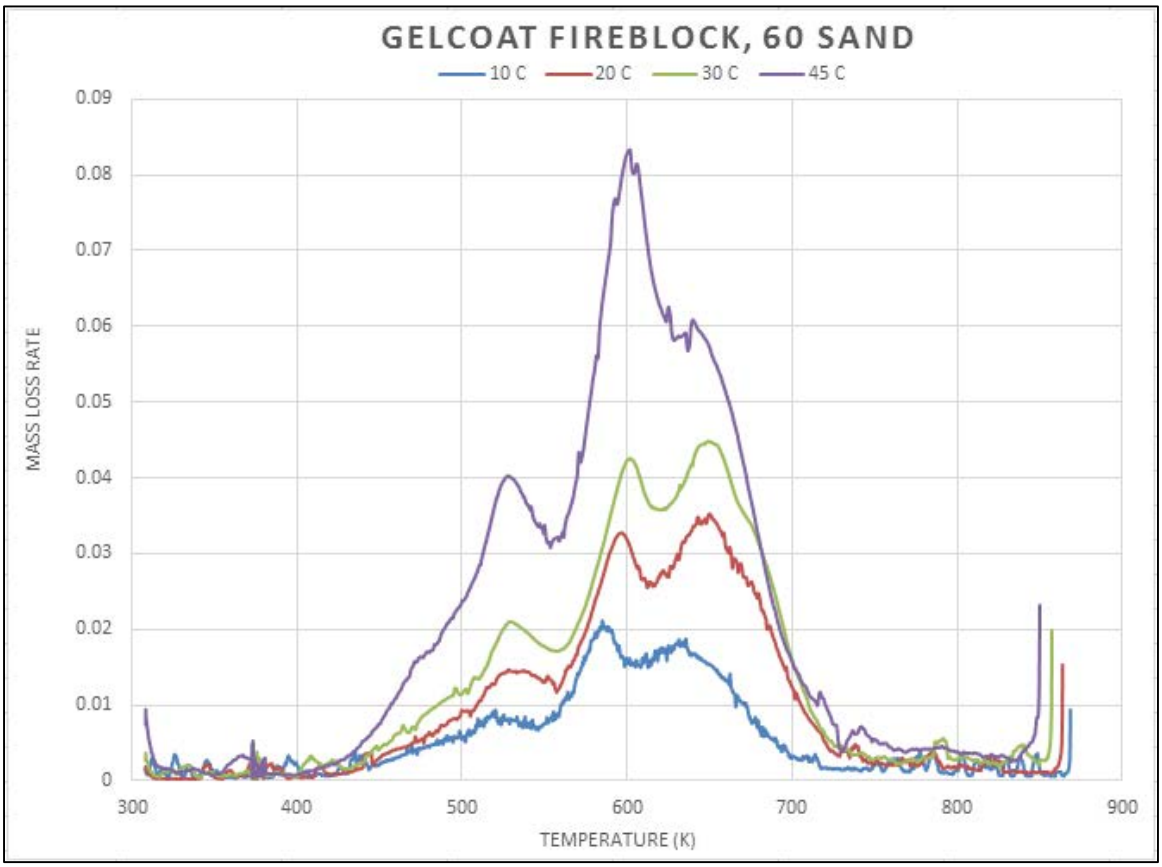

Figure 85: Single Heating Rate Method of Gelcoat Fireblock 60 Sand at Various Heating Rates

OFW Isoconversional Method

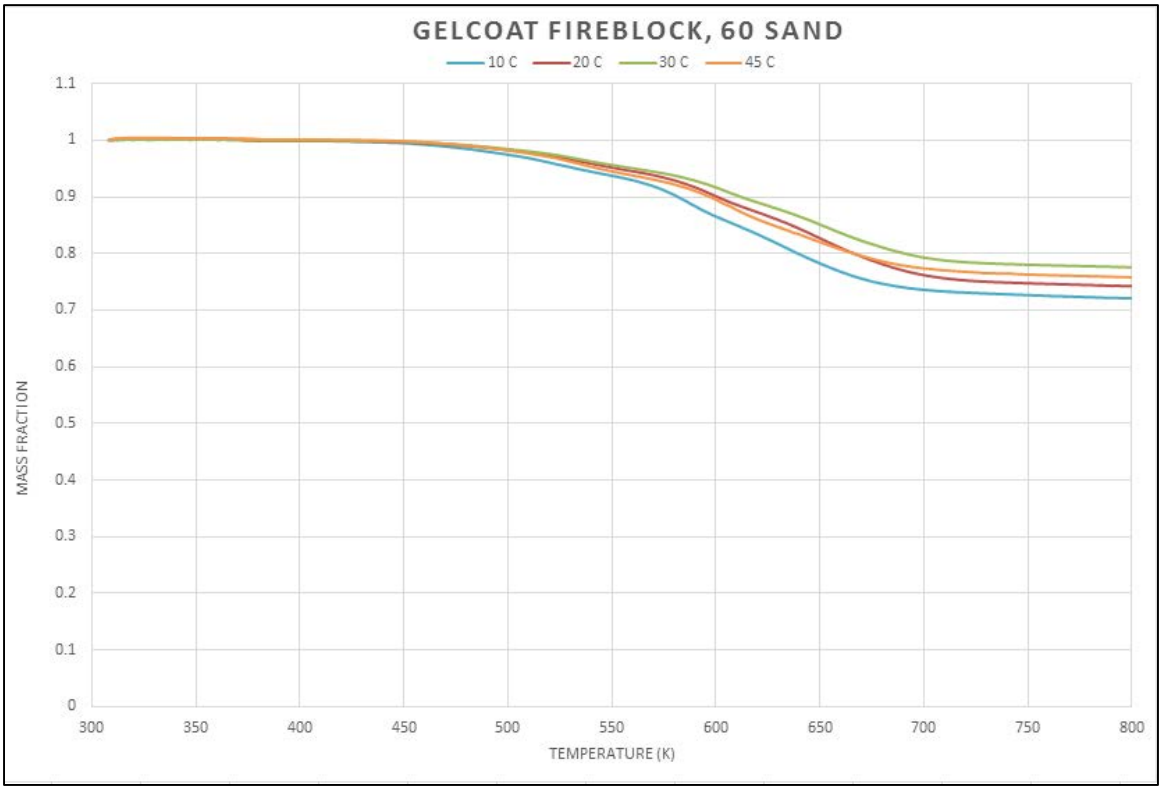

Figure 86: Multiple Heating Rate for TGA Gelcoat Fireblock, 60 Sand

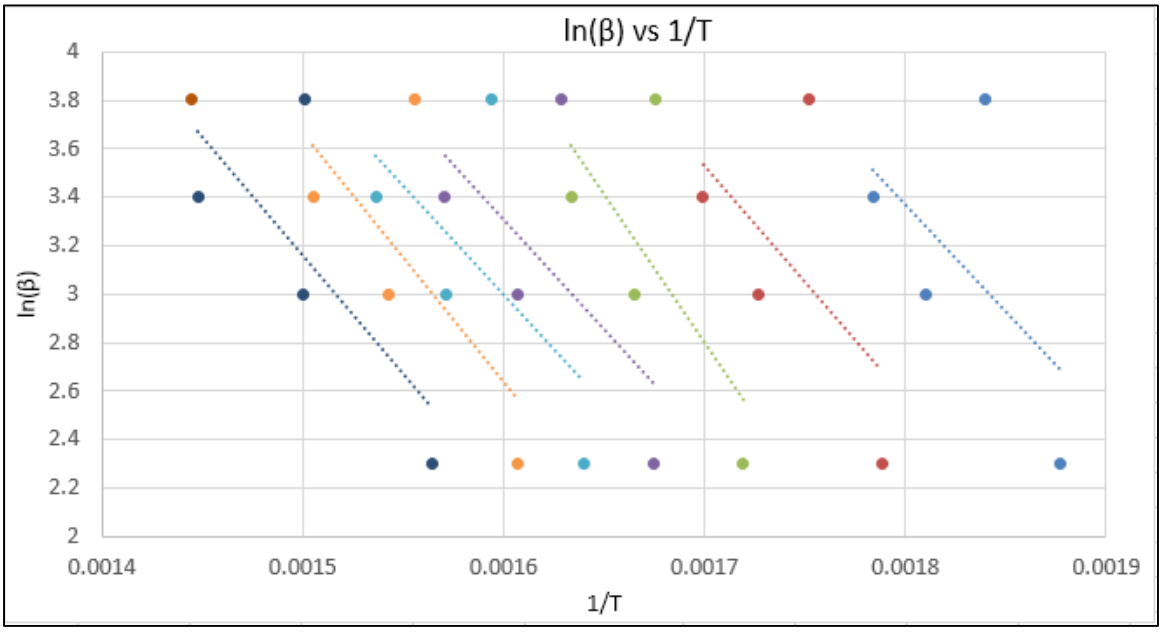

Figure 87: Intermediate Step in isoconversional method

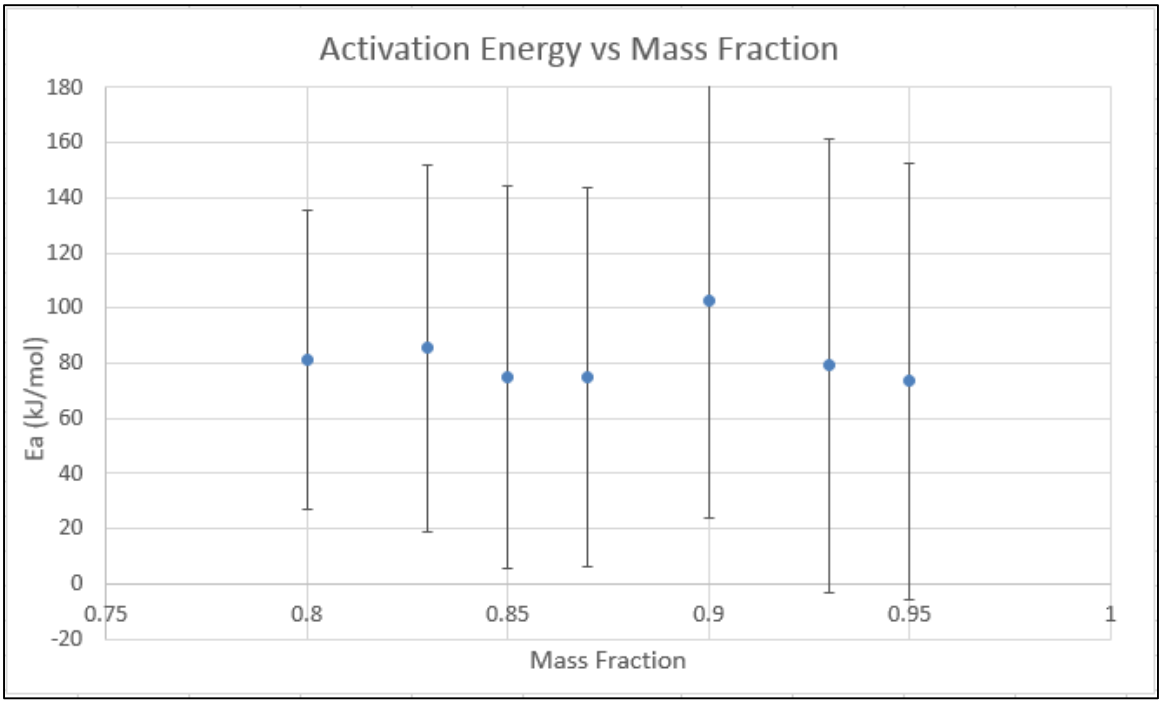

Figure 88: Activation energy trend observed at varying alpha values

Multiple Heating Rate – Activation Energy

Table 2: Gelcoat Fireblock Error and Activation Energy

α	Slope	LINEST	Ea (kJ/mol)	Error
0.95	-8833.75	9495.87	73.44	78.95
0.93	-9529.84	9891.48	79.23	82.24
0.90	-12325.06	9465.60	102.47	78.70
0.87	-8988.15	8269.96	74.73	68.76
0.85	-9007.77	8345.34	74.89	69.38
0.83	-10281.50	8003.42	85.48	66.54
0.80	-9792.17	6542.02	81.41	54.39
0.77	-2327.83	2463.54	19.35	20.48

Powder, Chunk, and Drop Analysis

TGA tests were run with Gelcoat Fireblock 60 Sand at the same heating rate, 30 K/min, for three different morphologies: powder, chunk, and drop.

Single Heating Rate Method

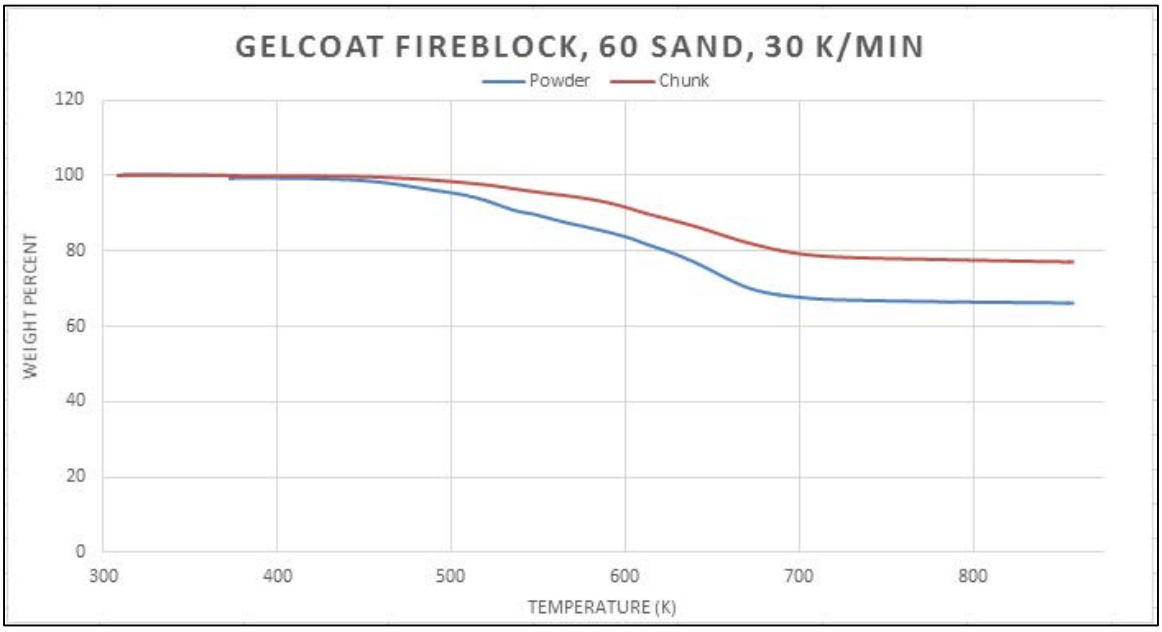

Figure 89: Powder, chunk, and drop samples single heating rate method at 30 K/min

Mass Loss History

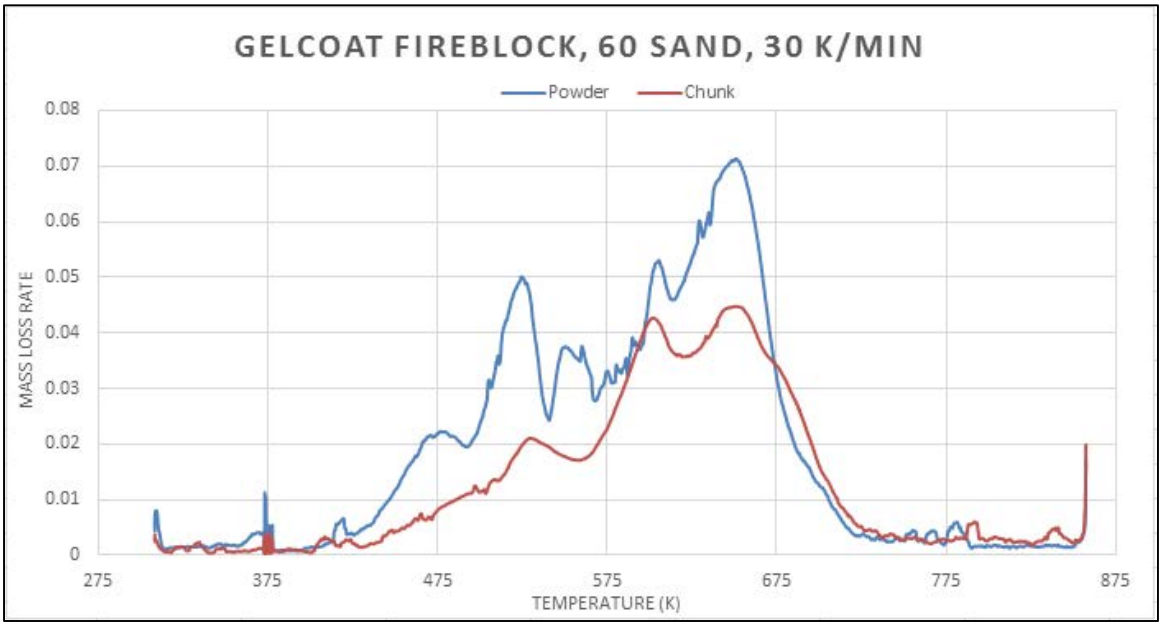

Figure 90: Powder, chunk, and drop data at 30 K/min

Appendix K: Gurit Ampreg 21FR Data

TGA tests were run with Ampreg-ATH (100:0) samples at four different heating rates, 10 K/min, 20 K/min, 30 K/min, and 45 K/min.

Single Heating Rate Method

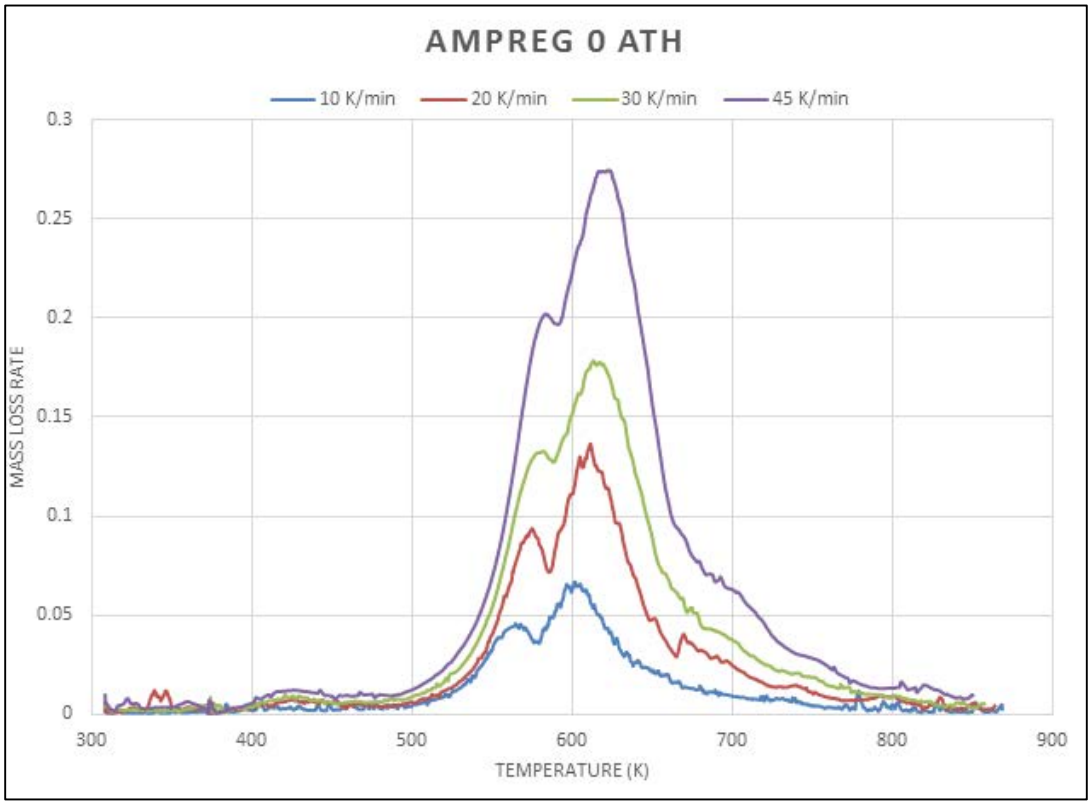

Figure 91: Single Heating Rate Method of Ampreg 0 ATH at Various Heating Rates

Single Heating Rate Method – Peak Temperature and Activation Energy

Table 18: Peak Temperature and Activation Energies

Heating Rate (K/min)	Peak Temperature (K)	Activation Energy (E_a – J/mol)	Pre-Exponential Factor (A)
10	633.1718	286236.6	3.52E+23
20	644.7258	296158.7	1.69E+24
30	650.7298	293984.5	9.92E+23
45	655.3896	251246.7	3.35E+20

OFW Isoconversional Method

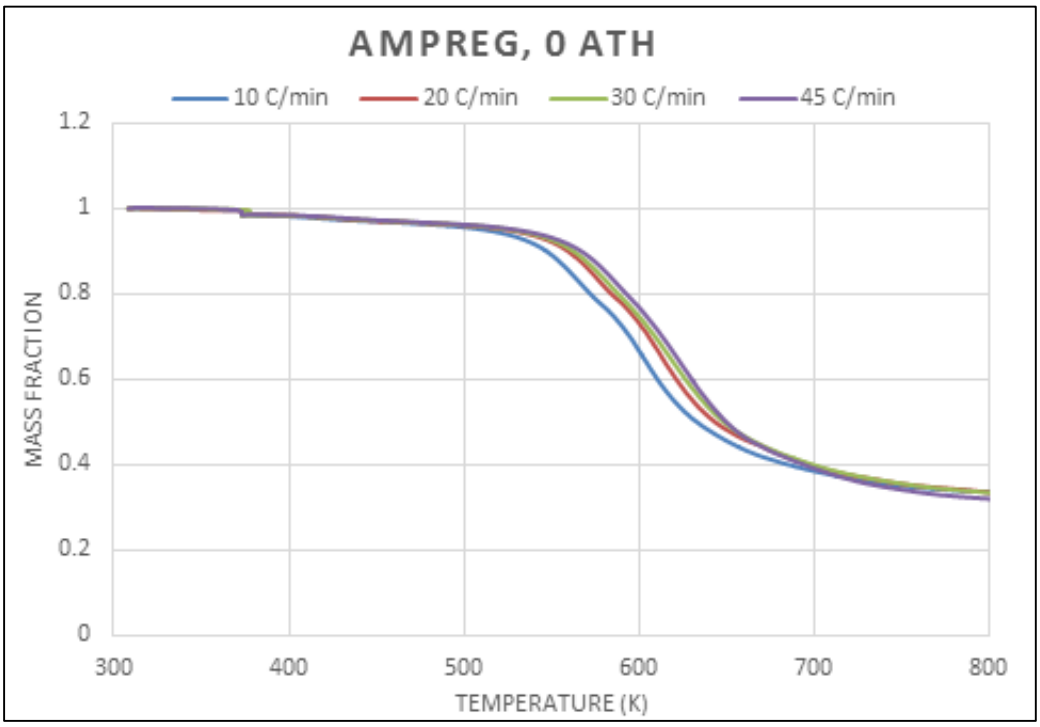

Figure 92: Multiple Heating Rate for Ampreg TGA Data

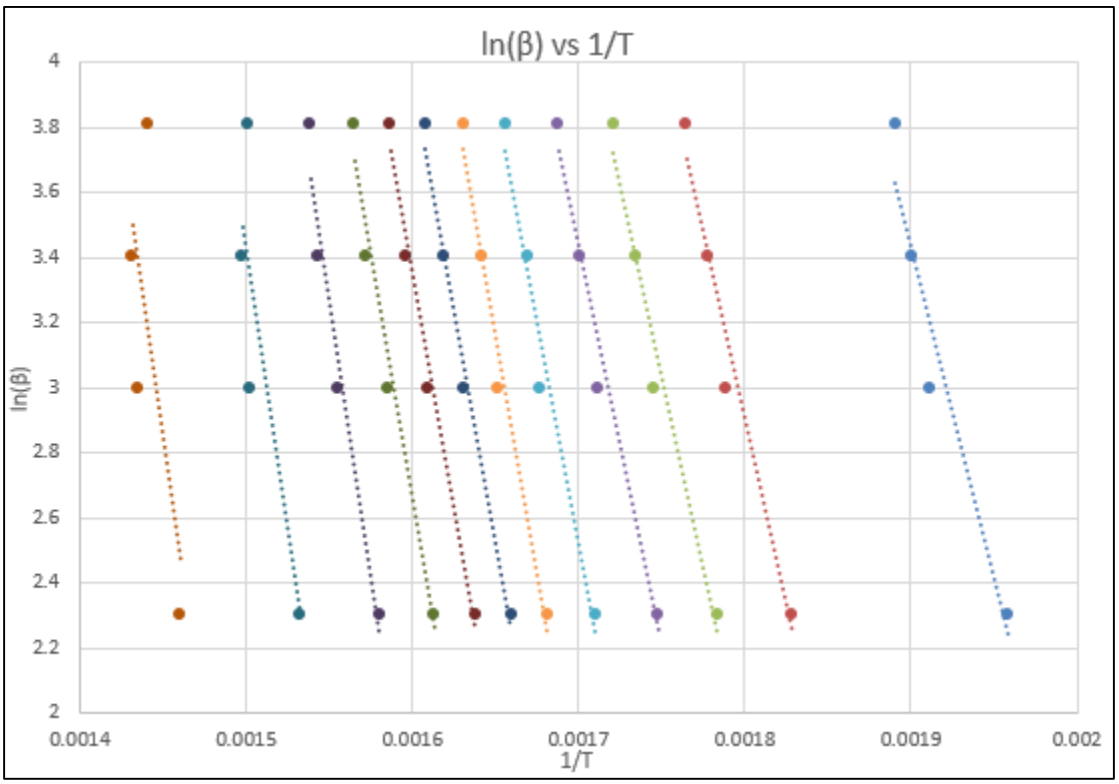

Figure 93: Intermediate Step in Isoconversional Method

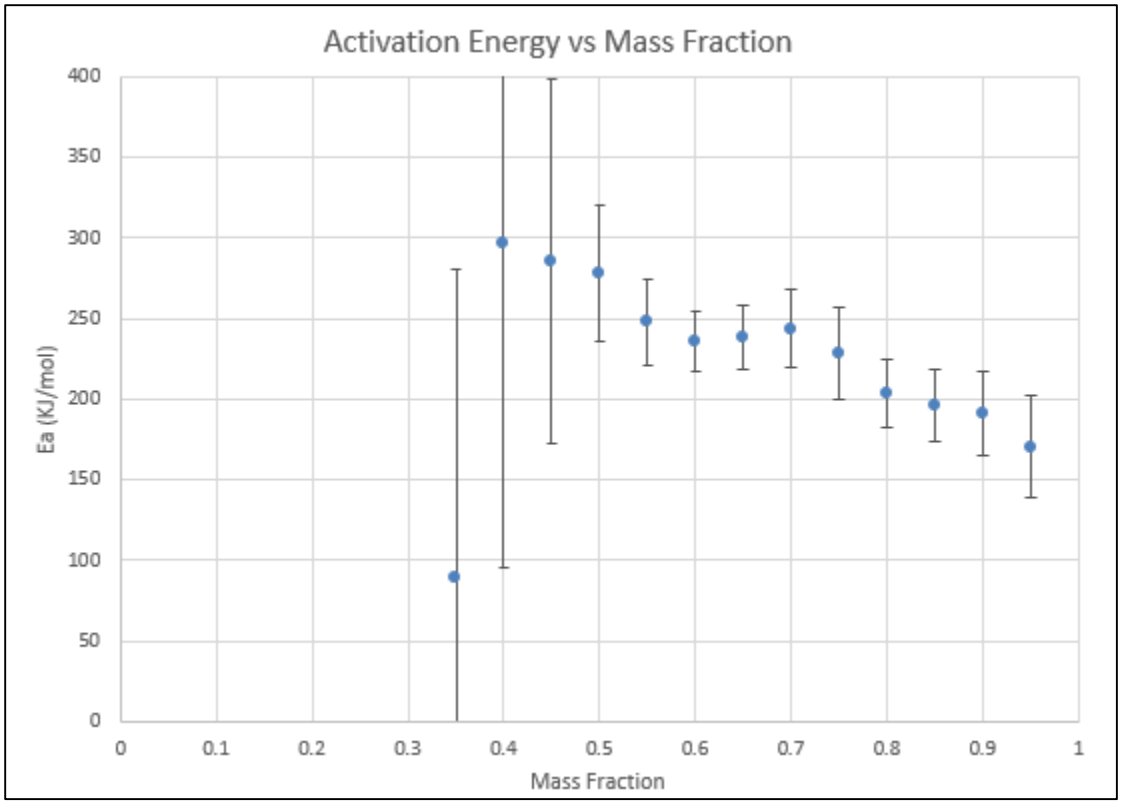

Figure 94: Activation Energy Trend Observed from Various Alpha Values

Multiple Heating Rate – Activation Energy

Table 19: Ampreg's Error and Activation Energy Determination

α	Slope	LINEST	Ea (kJ/mol)	Error
0.95	-20521	3870.09884	170.6116	32.176
0.9	-23007	3135.07223	191.2802	26.06499
0.85	-23550	2673.68014	195.7947	22.22898
0.8	-24472	2593.48198	203.4602	21.56221
0.75	-27500	3432.48198	228.635	28.53766
0.7	-29285	2896.87878	243.4755	24.08465
0.65	-28629	2376.98074	238.0215	19.76222
0.6	-28398	2247.7634	236.101	18.6879
0.55	-29803	3183.21379	247.7821	26.46524
0.5	-33471	5050.49013	278.2779	41.98977
0.45	-34334	13557.2029	285.4529	112.7146
0.4	-35619	24183.0473	296.1364	201.0579
0.35	-10678	23123.1539	88.77689	192.2459

Powder, Chunk, and Drop Analysis

TGA tests were run with Ampreg (0 ATH) samples at the same heating rates, 30 K/min, for three different morphologies chunk, powder, and drops.

Single Heating Rate Method

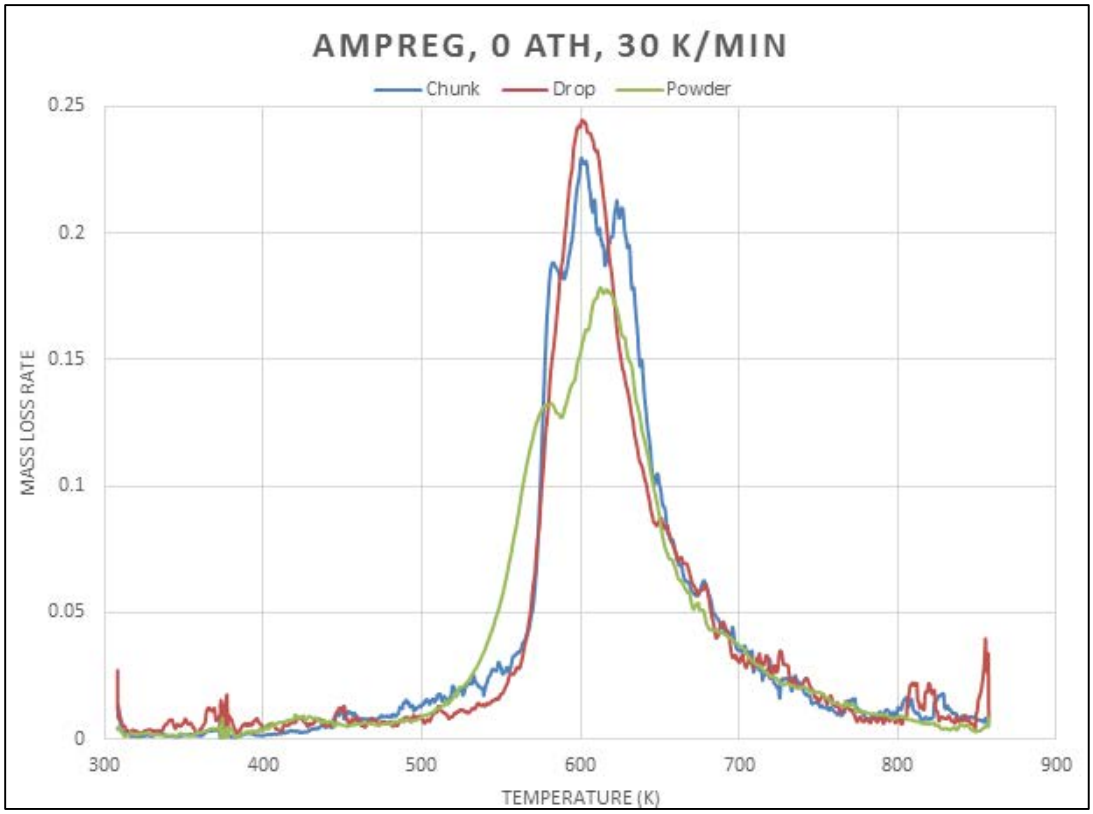

Figure 95: Powder, Chunk, and Drop Samples at Single Heating Rate, 30K/min

Mass Loss History

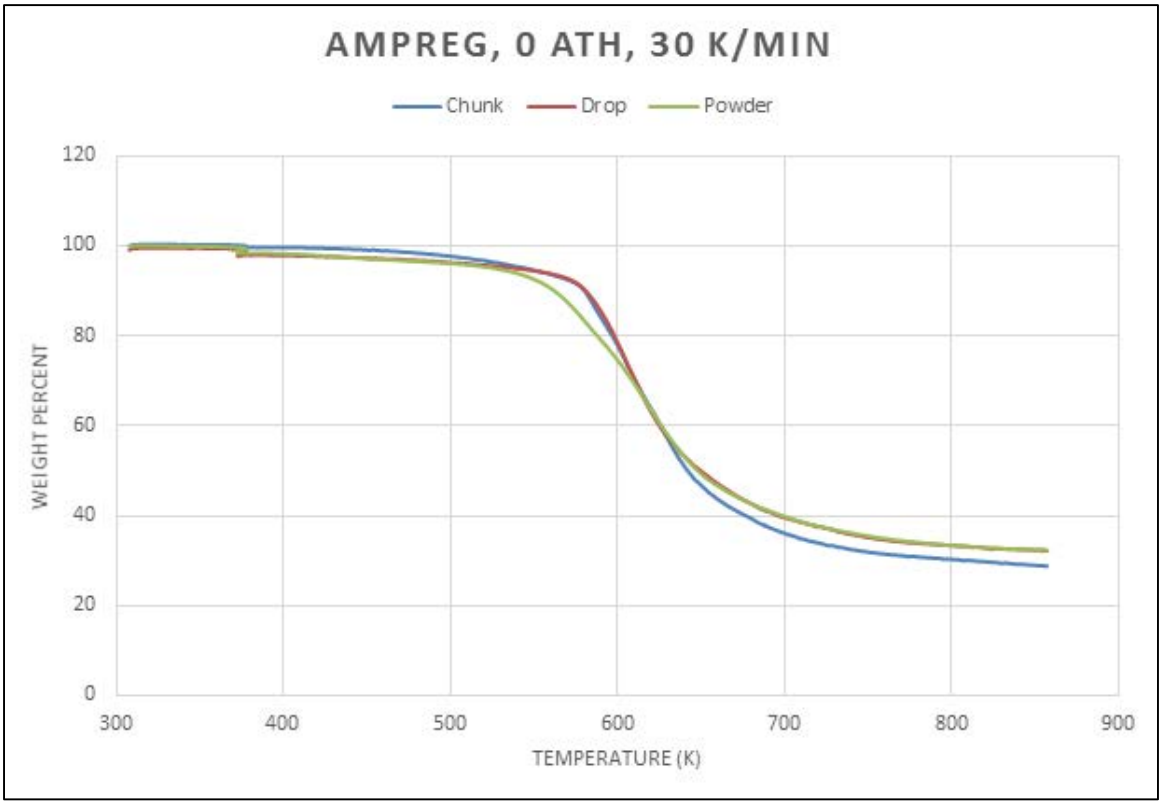

Figure 96: Change in Alpha Value compared to the temperature for various Sample Preps

References

[1] Stoliarov, Stanislav I., Jing Li. *Measurement of Kinetics and Thermodynamics of the Thermal Degradation for Non-charring Polymers*. Combustion and Flame, Volume 160:7 (1287-129). 2013.

[2] Kim, Esther. *Evaluating the Effects of Applying Different Kinetic Models to Pyrolysis Modeling of Fiberglass-reinforced Polymer Composites*. Fire and Materials. DOI: 10.1002/fam.2239. 2014

[3] TA Instruments. *Thermogravimetric Analysis*. Product Website. 2014. http://www.tainstruments.com/product.aspx?siteid=11&id=11&n=1

[4] Perkin Elmer. *Thermogravimetric Analysis (TGA): A Beginner's Guide.* 2010. http://www.perkinelmer.com/CMSResources/Images/44-74556GDE_TGABeginnersGuide.pdf

[5] TA Instruments. *Differential Scanning Calorimetry.* 2014. http://www.tainstruments.com/product.aspx?siteid=11&id=262&n=1

[6] Lautenberger, Christopher, Carlos Fernandez-Pello. *Generalized Pyrolysis Model for Combustible Solids.* Fire Safey Journal, Volume 44, 819-830. 2009.

[7] Ozawa, Takeo. *A New Method of Analyzing Thermogravimetric Data*. Bulletin of the Chemical Society of Japan, Volume 356:1 (1881 – 1886). 1965. https://www.jstage.jst.go.jp/article/bcsj1926/38/11/38_11_1881/_pdf

[8] Khawa, Ammar, Douglas Flanagan. *Role of Isoconversional Methods in Varying Activation Energies of Solid-State Kinetics*. Thermochimica Acta, Volume 429:1 (93-102). May 2005. http://www.sciencedirect.com/science/article/pii/S0040603104005271

[9] Wu, Weixuan, Junmeng Cai, Ronghou Liu. *Isoconversional Kinetic Analysis of Distributed Activation Energy Model Processes for Pyrolysis of Solid Fuels*. Industrial and Engineering Chemistry Research: 52 (14376-14383). 2013. http://pubs.acs.org/doi/pdf/10.1021/ie4021123

[10] Sbirrazzuoli, Nicolas, et al. *Integral, Differential and Advanced Isoconversional Methods: Complex Mechanisms and Isothermal Predicted Conversion–time Curves*. Chemometrics and Intelligent Laboratory Systems, Volume 95:2 (219-226). November 2007. http://www.sciencedirect.com/science/article/pii/S0169743909000173

[11] Stanislav I. Stoliarov, Richard N. Walters. *Determination of the Heats of Gasification of Polymers Using Differential Scanning Calorimetry*. Polymer Degradation and Stability, Volume 93:2 (422-427). February 2008.

[12] Engineering Toolbox. *Particle Sizes: Sizes of Airborne particles*. http://www.engineeringtoolbox.com/particle-sizes-d_934.html

[13] Tang, Benjamin. "Fiber Reinforced Polymer Composites Applications in USA." *Fiber Reinforced Polymer Composites Applications in USA*. U.S. Department of Transportation, 6 Jan. 1997. Web. 18 Oct. 2013.

[14] "Kreysler & Associates." *Kreysler Associates*. N.p., n.d. Web. 18 Oct. 2013.

[15] Curry, Bruce. "Fire Retardant Ployester Resin Formulations." (n.d.): n. pag. AOC World Leader in Resin Technology, 1 Oct. 2003. Web.

[16] International Building Code (IBC) Council. Chapter 26 Plastics. 2012.

[17] Keller, M. Dealing with NFPA 285. 2012, from http://www.payette.com/post/1661751-dealing-with-nfpa-285

[18] Navigating Wall Assembly Fire Testing. 2013.http://continuingeducation.construction.com/crs.php?L=51&C=1076

[19] Parker, William J. An Investigation of the Fire Environment in the ASTM E84 Tunnel Test. National Bureau of Standards. Washington, DC.

[20] C.A. Nieto de Castro et al. *Calibration of a DSC: Its Importance for the Traceability and Uncertainty of Thermal Measurements*. Thermochimica Acta, Volume 347 (85-91). 2000.

[21] M. Ferriol, A. Gentilhomme, M. Cochez, N. Oget, J.L. Mieloszynski. *Thermal Degradation of Poly(methyl methacrylate) (PMMA): Modelling of DTG and TG curves.* Polymer Degradation and Stability, Volume 79:2 (271-281). ISSN 0141-3910. 2003. http://www.sciencedirect.com/science/article/pii/S0141391002002914